SSI-BRIDGE 2:
SOIL-BRIDGE INTERACTION DURING LONG-DURATION EARTHQUAKE MOTIONS

FINAL PROJECT REPORT

by

Trevor J. Carey
H. Benjamin Mason
Andre R. Barbosa
Oregon State University

for

Pacific Northwest Transportation Consortium (PacTrans)
USDOT University Transportation Center for Federal Region 10
University of Washington
More Hall 112, Box 352700
Seattle, WA 98195-2700

In cooperation with US Department of Transportation-Research and Innovative Technology Administration (RITA)

Disclaimer

The contents of this report reflect the views of the authors, who are responsible for the facts and the accuracy of the information presented herein. This document is disseminated under the sponsorship of the U.S. Department of Transportation's University Transportation Centers Program, in the interest of information exchange. The Pacific Northwest Transportation Consortium, the U.S. Government and matching sponsor assume no liability for the contents or use thereof.

Technical Report Documentation Page

1. Report No.	2. Government Accession No.	3. Recipient's Catalog No.	
4. Title and Subtitle SSI-Bridge 2: Soil-bridge interaction during long-duration earthquake motions		**5. Report Date** **6. Performing Organization Code**	
7. Author(s) Trevor J. Carey, H. Benjamin Mason, and Andre R. Barbosa		**8. Performing Organization Report No.**	
9. Performing Organization Name and Address PacTrans Pacific Northwest Transportation Consortium University Transportation Center for Region 10 University of Washington More Hall 112 Seattle, WA 98195-2700		**10. Work Unit No. (TRAIS)** **11. Contract or Grant No.**	
12. Sponsoring Organization Name and Address United States of America Department of Transportation Research and Innovative Technology Administration		**13. Type of Report and Period Covered** **14. Sponsoring Agency Code**	

15. Supplementary Notes
Report uploaded at www.pacTrans.org

16. Abstract

Subduction zone earthquakes are characterized by their large magnitudes, which produce many cycles of strong ground shaking, and thus, long-duration earthquake motions. The Pacific Northwest is prone to subduction zone earthquake motions. Furthermore, many of the coastal bridges in the Pacific Northwest, which will be affected by strong ground shaking, are not designed for seismic loading. The 2011 Great East Japan Earthquake, during which notable damage to coastal bridges occurred, serves as motivation for this study. Herein, a model of a prototypical Pacific Northwest bridge is developed in the finite element framework OpenSees. The modeling considers shaking in two bridge directions, longitudinal and transverse, as well as two site-soil conditions, liquefiable and non-liquefiable. The bridge models are subjected to strong shaking with a suite of 46 subduction zone earthquake motions and 48 shallow crustal earthquake motions. Damage is tracked with two demand parameters: (1) the number of inelastic excursions (NIE), which tracks how many times the bridge column was demanded into its inelastic zone during the strong shaking; and (2) the cumulative plastic rotation (CPR), which accounts for the accumulation of damage in the bridge column during the strong shaking. The results show that subduction zone earthquake motions had much higher NIEs and CPRs compared to the shallow crustal earthquake motions. Furthermore, the earthquake motion intensity parameters that incorporate duration better predicted the NIE and CPR compared to the intensity measures that only incorporated amplitudinal intensity. The prediction of the NIE and CPR for durational dependent earthquake motion intensity parameters was validated with correlation coefficients. The liquefiable site-soil conditions were found to cause a decrease in the NIE and CPR compared with the non-liquefiable site-soil conditions. The difference in damage was attributed to the liquefiable site-soil condition fundamentally changing the earthquake motion and leading to the lengthening of the fundamental period of the soil-bridge systems. The results of the research imply that to increase the safety of our transportation network in the Pacific Northwest, engineers should consider earthquake motion intensity parameters and demand parameters that include the effects of earthquake motion duration when performing seismic design of bridges.

17. Key Words		18. Distribution Statement	
Earthquakes, bridge safety, seismic design		No restrictions.	
19. Security Classification (of this report) Unclassified.	**20. Security Classification (of this page)** Unclassified.	**21. No. of Pages**	**22. Price** NA

Form DOT F 1700.7 (8-72) **Reproduction of completed page authorized**

Table of Contents

List of Figures

List of Tables

Acknowledgments

The authors are grateful for the help of Michael H. Scott, Pedro Arduino, and Kyle T. Romney. In addition, the authors are grateful for the support of PacTrans and particularly the support of the local Oregon State University PacTrans team, including Chris Bell, David Hurwitz, and Dana Ainsworth. The work presented herein is largely from the Master of Science thesis written by Trevor J. Carey at Oregon State University (Carey 2014; Carey et al. 2014).

Executive Summary

The recent Great East Japan Earthquake emphasized the hazards associated with large magnitude, long-duration earthquakes. Damage to bridges during earthquakes is particularly important, because regional recovery heavily depends on the operation of bridges to move supplies and equipment. Like Japan, the Pacific Northwest (PNW) also experiences devastating mega-thrust earthquakes. Understanding the earthquake hazard is critical, because PNW coastal bridges may not be adequately designed for long-duration strong ground shaking. The objective of this work is to determine the safety and resilience of a typical PNW coastal bridge to the expected long-duration earthquake. To meet the aforementioned objective, a soil-bridge system was numerically modeled to determine the seismic response of a typical PNW coastal bridge. The numerical soil-bridge system was developed using the OpenSees finite element framework (McKenna *et al.* 2010). The OpenSees finite element framework has been used by researchers for the last decade to perform advanced structural and geotechnical earthquake simulations. The diverse assortment of constitutive models, solution algorithms and element formulations in the OpenSees framework allows for the determination of structural damage during earthquake loading. Soil-bridge systems have been predominately designed for amplitudinal intensity parameters with no consideration of earthquake motion duration. Accordingly, to determine how the duration of an earthquake can cause damage to soil-bridge systems, a suite of 46 subduction zone and 48 shallow crustal earthquake motions were selected, and the earthquake motions were inputted into the numerical soil-bridge model. All earthquake motions were linearly scaled to the same target spectrum to isolate earthquake motion duration effects. The analyses was performed

with four different soil-bridge model configurations. In addition to transverse and longitudinal bridge orientations, a non-liquefiable and liquefiable site-soil condition was also included. The four soil-bridge model configurations extend the singular configuration by Barbosa *et al.* (2014) for a similar soil-bridge model. The results were analyzed in terms of two demand parameters: (1) the number of inelastic excursions (*NIE*), which tracks how many times the bridge column was demanded into its inelastic zone during the strong shaking; and (2) the cumulative plastic rotation (*CPR*), which accounts for the accumulation of damage in the bridge column during the strong shaking.

Subduction zone earthquake motions, which have longer durations compared to shallow crustal earthquake motions had much higher *NIE*s and *CPR*s compared to the shallow crustal earthquake motions. The increase in *NIE* and *CPR* for the subduction zone earthquake motions was apparent for each of the four model configurations considered. Furthermore, the earthquake motion intensity parameters that incorporate duration better predicted the *NIE* and *CPR* compared to the intensity measures that only incorporated amplitudinal intensity. The prediction of the *NIE* and *CPR* for durational dependent earthquake motion intensity parameters was validated with correlation coefficients. The liquefiable site-soil conditions were found to cause a decrease in the *NIE* and *CPR* compared with the non-liquefiable site-soil conditions. The difference in damage was attributed to the liquefiable site-soil condition fundamentally changing the earthquake motion (i.e., intensity and frequency content) and leading to the lengthening of the fundamental period of the soil-bridge systems. The results of the research imply that to increase the safety of our transportation network in the Pacific Northwest, engineers should consider earthquake motion intensity parameters and demand parameters that include the effects of earthquake motion duration when performing seismic design of bridges.

Chapter 1 Introduction

The recent Great East Japan Earthquake emphasized the hazards associated with large magnitude, long-duration earthquakes. Damage to bridges during earthquakes is particularly important, because regional recovery heavily depends on the operation of bridges to move supplies and equipment. Like Japan, the Pacific Northwest (PNW) also experiences devastating mega-thrust earthquakes. Understanding the earthquake hazard is critical, because PNW coastal bridges may not be adequately designed for long-duration strong ground shaking. The objective of this work is to determine the safety and resilience of a typical PNW coastal bridge to the expected long-duration earthquake.

To meet the aforementioned objective, a soil-bridge system was numerically modeled to determine the seismic response of a typical PNW coastal bridge. The numerical soil-bridge system was developed using the OpenSees finite element framework (McKenna *et al.* 2010). The OpenSees finite element framework has been used by researchers for the last decade to perform advanced structural and geotechnical earthquake simulations (e.g., Zhang *et al.* 2008). The diverse assortment of constitutive models, solution algorithms and element formulations in the OpenSees framework allows for the determination of structural damage during earthquake loading. Soil-bridge systems have been predominately designed for amplitudinal intensity parameters with no consideration of earthquake motion duration. Accordingly, to determine how the duration of an earthquake can cause damage to soil-bridge systems, a suite of 46 subduction zone and 48 shallow crustal earthquake motions were selected, and the earthquake motions were inputted into the numerical soil-bridge model. All earthquake motions were linearly scaled to the same target spectrum to isolate earthquake motion duration effects. The analyses was performed with four different soil-bridge model configurations. In addition to transverse and longitudinal

bridge orientations, a non-liquefiable and liquefiable site-soil condition was also included. The four soil-bridge model configurations extend the singular configuration by Barbosa *et al.* (2014) for a similar soil-bridge model.

Chapter 2 Literature Review

Soil-structure interaction (SSI) has been considered by engineering researchers and practitioners to accurately evaluate the seismic response of soil-bridge systems. Bridge-systems that incorporate SSI have longer fundamental periods and increased system damping compared with fixed-base bridge-systems. Typically, SSI has been thought to only benefit bridge-systems, because seismic demands are usually reduced when SSI effects are considered during seismic design. However, depending on the earthquake motion and the flexible-base foundation period shift, seismic demands may actually increase (e.g., Mylonakis and Gazetas 2000). Figure 2.1 illustrates that SSI does not always reduce seismic demands depending on the earthquake motion and period shift (NIST 2012). The uncertainty of seismic demands is the primary motivation for including SSI in the bridge system analysis. Soil-bridge system literature presented in this chapter is neither exhaustive nor focused explicitly on basic SSI principles. Kausel (2010) provides a history of SSI research and advances.

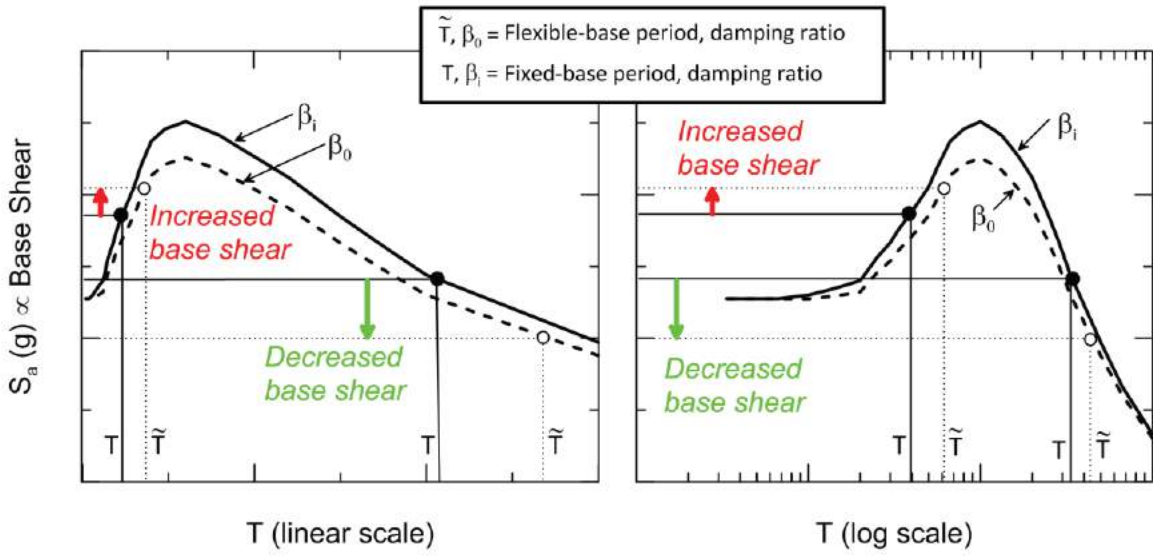

Figure 2.1. Idealization of base shear demands for a flexible-based system (i.e. includes SSI) with increased damping and period lengthening compared to a fixed-base system (NIST 2012).

One of the first numerical soil-bridge models created with the OpenSees framework was developed by Zhang *et al.* (2008) for the Humboldt Bay Middle Channel (HBMC) Bridge. The bridge deck of the HBMC Bridge is cast-in-place reinforced concrete and is supported by four precast, prestressed I-girders. The bridge deck and girders are assumed to respond linearly elastically during loading, given the high axial stiffness of the girder-bridge-deck composite. The bridge girders are supported by nine reinforced concrete piers that transmit forces and rotational moments to the soil continuum. The nine reinforced concrete piers are modeled in OpenSees using the Mander *et al.* (1988) confined concrete model and are discretized using fiber sections and beam-column elements. The modeled soil continuum, which is illustrated in Figure 2.2, incorporates liquefiable layers beneath and atop a competent non-liquefiable layer. The soil continuum is represented with a far-field mesh composed of 4 node "u-p" quadrilateral, plane-strain elements (Elgamal *et al.* 2002) that combine soil-skeleton displacement (*u*) and pore water pressure (*p*). The far-field mesh and structural bridge model are shown in Figure 2.3. Zhang *et al.* (2008) concluded the seismic response of the soil-bridge system was controlled by the nonlinear inelastic response of the soil continuum. Plastic deformation of the soil caused by lateral spreading and liquefaction resulted in large residual deformations and internal forces.

Khosravifar (2012) developed a two-dimensional nonlinear inelastic soil-bridge model for a single pile-foundation shaft. The model illustrated in Figure 2.4 was used to evaluate the inelastic structural response from effects of liquefaction and lateral spreading. Additionally, Khosravifar (2012) performed a parametric study to determine which system parameters had the greatest effect on the response of the soil-bridge system to earthquake loading. The soil-bridge model developed by Khosravifar (2012) considered the transverse direction of a typical pre-stressed box-beam bridge. The tributary mass and gravity loads were lumped at the bridge deck.

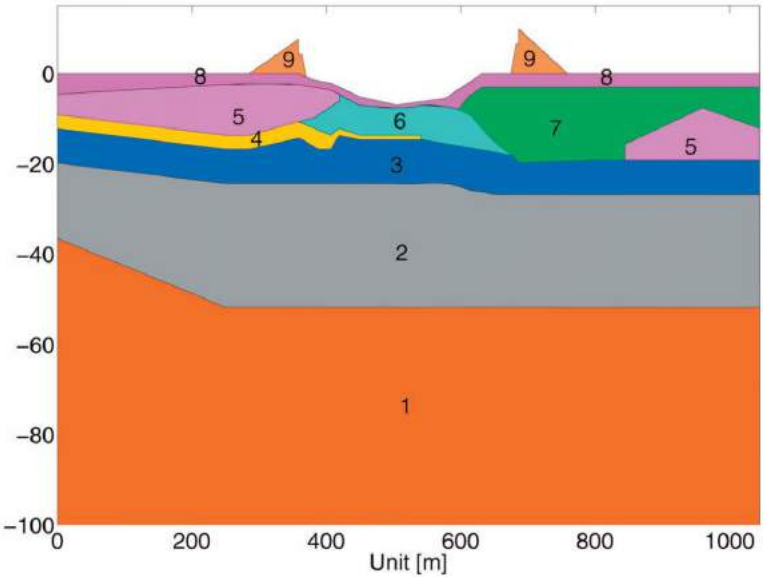

Figure 2.2. Two-dimensional soil profile of HBMC Bridge site. Layer 1: Tertiary and Quaternary Alluvial deposits; Layer 2: medium dense organic silt, sandy silt and stiff silty clay; Layer 3: dense sand; Layer 4: silt; Layer 5: medium dense to dense silty sand and sand with some organic matter; Layer 6: dense silty sand and sand; Layer 7: soft or loose sandy silt or silty sand with organic matter; Layer 8: soft to very soft organic silt with clay; and Layer 9: abutment fill (Zhang *et al.* 2008).

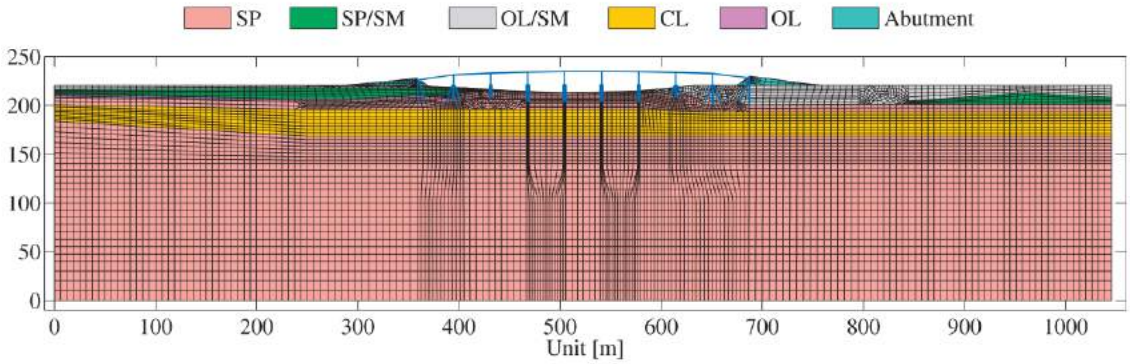

Figure 2.3. Two-dimensional soil mesh of the HBMC Bridge OpenSees model (Zhang *et al.* 2008).

The soil profile Khosravifar (2012) selected consisted of a 5 m clay crust, 3 m loose liquefiable sand and 12 m dense non-liquefiable sand. The soil-profile was discretized to a far-field soil column consisting of 9 node “u-p” quadrilateral elements. The pressure independent multi-yield material was used to model clays, and the pressure dependent multi-yield material

was used to model sands. The soil column was attached to the pile-foundation with one dimensional lateral p-y, vertical t-z, and end bearing q-z soil interface springs. The spring coefficients were developed using recommendations from the American Petroleum Institute (API 1993), with modifications to the lateral p-y springs using a procedure proposed by Boulanger *et al.* (1999) to account for larger effective overburden stresses. Similar to the soil-bridge model presented by Zhang *et al.* (2008), the column and pile-foundation was a continuous reinforced concrete shaft that was discretized into a fiber section for use with beam column elements.

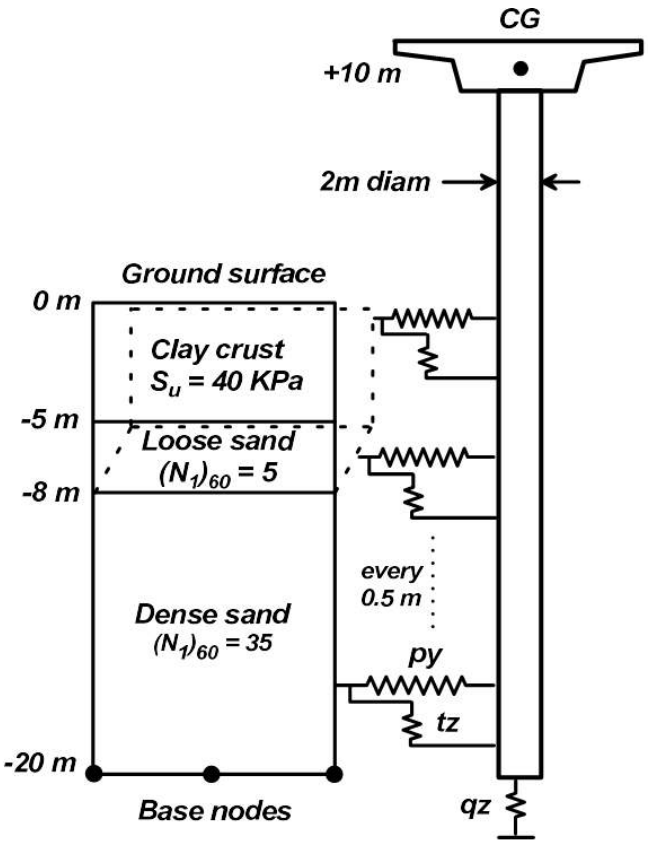

Figure 2.4. Two-dimenstional transverse bridge, soil column, and one-dimensional interface springs presented by Khosravifar (2012).

Khosravifar (2012) showed the combined effect of structural inertial forces and lateral spreading produced greater demands than the isolated case of non-liquefaction or lateral spreading. Khosravifar (2012) concluded that to determine the correct seismic response of a bridge-system, the analysis needs to consider all components (i.e., bridge deck, column, pile, soil) and non-linear material response.

Barbosa *et al.* (2014) used work by Zhang *et al.* (2008) and Khosravifar (2012) as motivation to develop the two-dimensional nonlinear longitudinal soil-bridge model illustrated in Figure 2.5. The soil-bridge model presented by Barbosa *et al.* (2014) was a 63.4 m long reinforced concrete bridge supported by a center column and end abutments, which was adapted from a model presented by Shamsabadi *et al.* (2007).

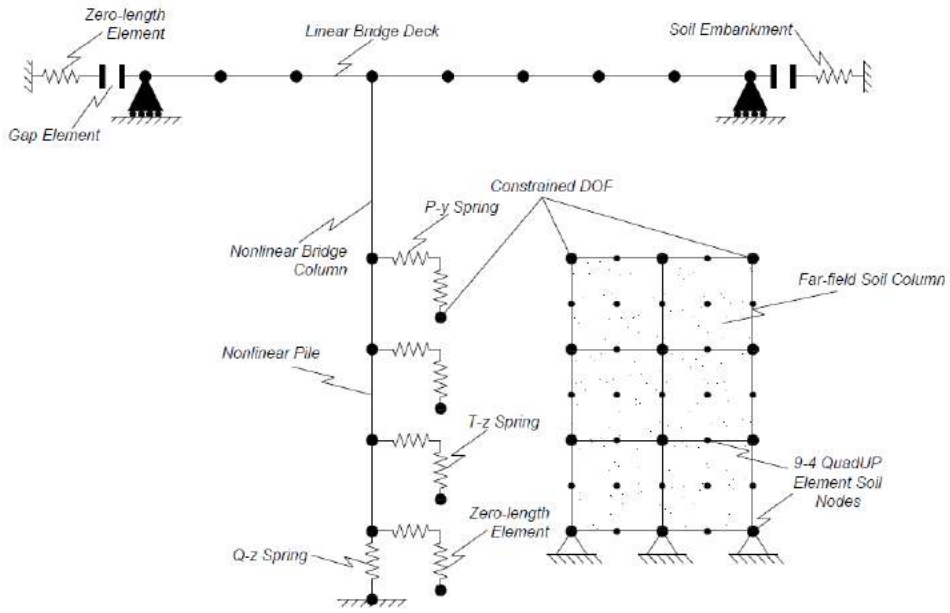

Figure 2.5. Two-dimensional longitudinal soil-bridge model presented by Barbosa *et al.* (2014).

The soil-bridge modeling effort herein closely follows the assumptions, and methodologies developed by Barbosa *et al.* (2014). A comprehensive description of the soil-bridge model by Barbosa *et al.* (2014) with minor alterations is forthcoming in 0.

Chapter 3 Soil-Bridge Modeling Methodology

3.1 Introduction

The primary focus of this chapter is to introduce and present the methodology used to model a typical Pacific Northwest (PNW) coastal bridge. Soil-structure-interaction (SSI) was considered by including the underlying bridge foundation and soil continuum elements. The two-dimensional soil-bridge models presented herein were developed in the OpenSees finite element framework.

To quantify the seismic response of the soil-bridge system, both the longitudinal and transverse components of the bridge were examined. As shown in Figure 3.1, the longitudinal component of the soil-bridge system is parallel to the bridge deck, whereas the transverse component is orthogonal to the bridge deck.

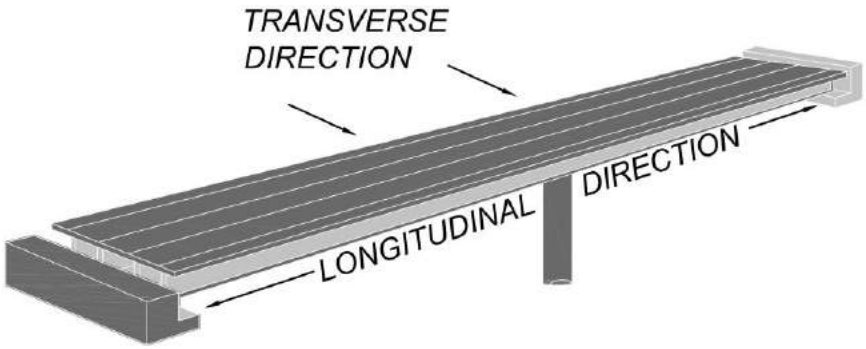

Figure 3.1. Conceptual bridge deck drawing showing longitudinal & transverse direction. (after Shamsabadi *et al.* 2007)

The longitudinal and transverse directional components are represented by two different finite element models. The bridge deck cross section in the longitudinal direction is modeled with single line elements that are supported by end abutments and monolithically connected to a center column. For the transverse direction, the bridge deck cross section is explicitly modeled with line elements supported by a center column. The in-plane views of the longitudinal and

transverse models are conceptualized in Figure 3.2. The center column for the longitudinal and transverse directions is attached to a pile foundation, which extends 20 m to the underlying bedrock. The pile foundation transmits vertical and horizontal loads by means of one-dimensional soil interface springs.

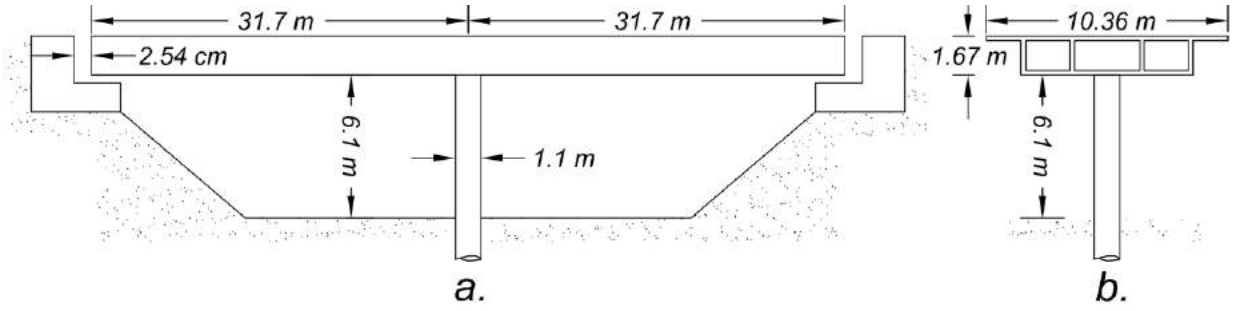

Figure 3.2. Directional components of the soil-bridge system (a) in-plane view of the longitudinal model (b) in-plane view of the transverse model (pile foundation and soil mesh not shown for clarity).

The soil interface springs are attached to a far-field soil column, which is representative of a soil continuum. To represent potential site-soil conditions that can reasonably expected along the Oregon coast, a liquefiable and non-liquefiable soil profile was considered for the soil-bridge system. The column/pile design, soil properties, strength parameters, and geometry are identical for the two different models.

3.2 Earthquake Motion Selection

The Pacific Northwest is susceptible to both shallow crustal and subduction zone earthquakes. Compared to shallow crustal earthquake motions, subduction zone earthquake motions tend to have longer durations, lower frequency contents, and release more energy. To understand the unique demands from shallow crustal and subduction zone earthquake motions, suites of both types of earthquake motions were considered. Before selecting suites of shallow

crustal or subduction zone earthquakes, a target design spectrum was generated. The target design spectrum was used to design the soil-bridge model for seismically induced lateral forces. Furthermore, the shallow crustal and subduction zone suite of earthquake motions were linearly scaled to match the target design spectrum. The site chosen to create the design spectrum is located on the Oregon coast in Lincoln City (44.96745 N, 124.01646 W). The design spectrum was produced using the 2009 AASHTO guidelines for site soil class B. Site soil class B is defined as rock with a shear wave velocity of ($762 < V_s$ (m/s) < 1524). Site soil class B was selected because earthquake motions are inputted at the soil-bedrock interface for the soil-bridge model. In Figure 3.3 the linear, 5 percent damped, pseudo-spectral acceleration design response spectrum is plotted.

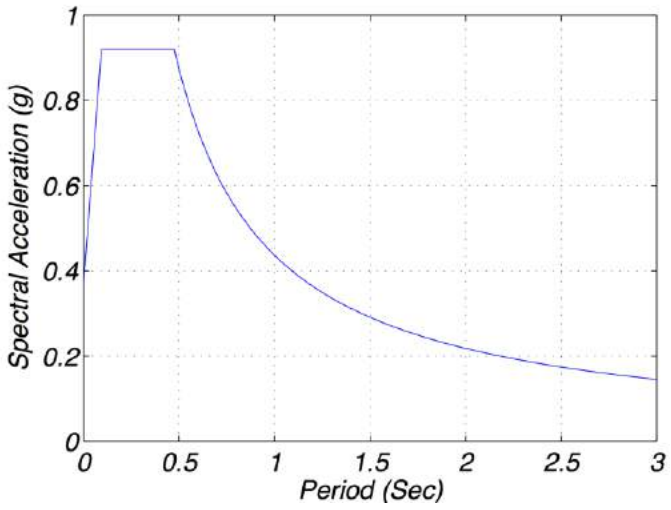

Figure 3.3. Target design response spectrum for Lincoln City, Oregon. Based on 2009 AASHTO guidelines for soil type B, rock ($762 < V_s$ (m/s) < 1524)

The complete suite of subduction zone earthquake motions were obtained from the March 11, 2011 Great East Japan earthquake, a 9.0 moment magnitude event, which was 300 s in duration at the selected recording sites. Earthquake motion records were obtained from both Kik-

net and K-NET recording stations. The earthquake motions selected for the subduction zone earthquake motion suite came from the Sendai and Sanriku regions located on the Northeast coast of Japan. A total of 46 earthquake records were selected, which were all recorded on bedrock to match the rock site-soil condition (i.e., site class B) selected for the target design spectrum. The selected earthquake motions were unfiltered, and thus, required filtering before use (Boore and Bommer 2005). Each selected earthquake motion was filtered with a fourth-order Butterworth filter with earthquake motion specific corner frequencies. Signal processing was performed using MATLAB. Arias intensity (I_a), significant duration (D_{5-95}), peak ground acceleration (*PGA*), peak ground velocity (*PGV*), and modified cumulative absolute velocity (CAV_5) were determined for each filtered earthquake motion. In Appendix A the locations, station names, Butterworth corner frequencies and intensity parameters for each of the subduction zone earthquake motions are reported.

The suite of shallow crustal earthquake motions were provided by Baker *et al.* (2011) as part of a Pacific Earthquake Engineering Research Center (PEER) report. Baker *et al.* (2011) provides multiple suites of shallow crustal earthquake motions for the analysis of various structural and geotechnical systems. The suite of shallow crustal earthquake motions were selected from the Baker *et al.* (2011) set #2. Set #2 consists of earthquake motions recorded by 40 different stations founded on bedrock. Three components of the earthquake motions are recorded by each station (i.e., fault parallel, fault normal, and vertical). The earthquake motions in set #2 were selected to have magnitudes near 7.0 and source-to-site distances near 10 km. Of the 40 stations in set #2, 24 stations were selected to develop the suite of shallow crustal earthquake motions. For each of the 24 selected stations the fault parallel and fault normal components were considered for a total of 48 shallow crustal earthquake motions. Notably, 48

shallow crustal earthquake motions were selected to roughly equal the same number of subduction zone earthquake motions. Appendix B contains the locations, stations names, and intensity parameters for each of the 48 shallow crustal earthquake motions.

The automated process implemented in MATLAB to linearly scale the shallow crustal and subduction zone earthquake motions in the time-domain is similar to the procedure presented in Barbosa *et al.* (2014) which is similar to the procedure developed by Kottke and Rathje (2008). Each earthquake motion was scaled by a linear scaling factor (*SF*), and then, the root-mean-square-error (*RMSE*) was calculated between the target spectrum and scaled earthquake motion spectrum. The *RMSE* error proposed by Barbosa *et al.* (2014) is as follows,

$$RMSE = \sqrt{\sum_{i=1}^{n}\left[\ln\left(S_{a,\text{target}(T_i)}\right) - \ln\left(SF \cdot S_{a,\text{eqke}(T_i)}\right)\right]^2} \quad , \tag{3.1}$$

where $S_{a,target(Ti)}$ is the response spectral accelerations for the target spectrum, and $S_{a,eqke(Ti)}$ is the response spectral acceleration for the considered unscaled earthquake motion and T_i (i = 1...n) is the number of periods in which the response spectrum is specified.

Barbosa *et al.* (2014) used a specific period range (i.e., near the fundamental period of the structure-of-interect) to fit earthquake motions using Eq. 3.1; however, a specific period range was not considered herein, because of the considerable difference between the fundamental periods of the longitudinal and transverse directions of the soil-bridge system. Although a specific period range was not considered, a unique method was used to scale the shallow crustal and subduction zone earthquake motions. The subduction zone earthquake motions were first scaled to the target design spectrum using the procedure proposed in Barbosa *et al.* (2014). Then, the median response spectrum from all 46 scaled subduction zone earthquake motions was calculated. The shallow crustal earthquake motion suite was then scaled to the median response

spectrum of the subduction zone earthquake motion suite, rather than the target design spectrum. Scaling the shallow crustal earthquake motions to the median subduction zone spectral response is preferred, because it ensures that the shallow crustal and subduction zone earthquake motions have roughly equivalent amplitudes and frequency content intensity measures.

Figure 3.4 shows the calculated subduction zone median response spectrum plotted against the AASHTO target design spectrum. Figure 3.5 shows the shallow crustal median response spectrum and the subduction zone median response spectrum, which was used as the $S_{a,target}$. The relative difference between the subduction zone and shallow crustal median response spectrum is presented in Figure 3.6. Good agreement is shown in Figure 3.6 for the period range of 0.125 to 1.375 s, with the relative difference between median responses averaging to roughly 5 percent. Greater discrepancy is observed for periods greater than 1.375 s, with the relative difference between median responses averaging to roughly 35 percent. An increased error at longer periods is caused by the fundamental difference of the shallow crustal and subduction zone earthquake motions; i.e., subduction zone earthquake motions tend to have lower frequency contents.

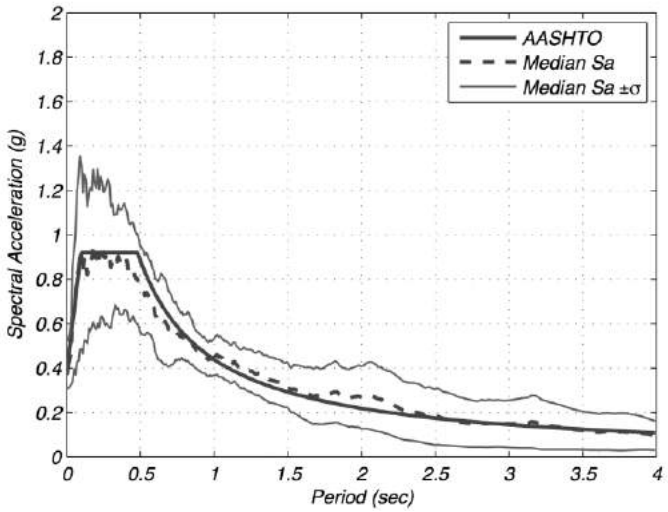

Figure 3.4. Response spectrum for 46 Great East Japan Earthquake subduction zone earthquake motions plotted against AASHTO 2009 design response spectrum for Lincoln City, Oregon for soil type B.

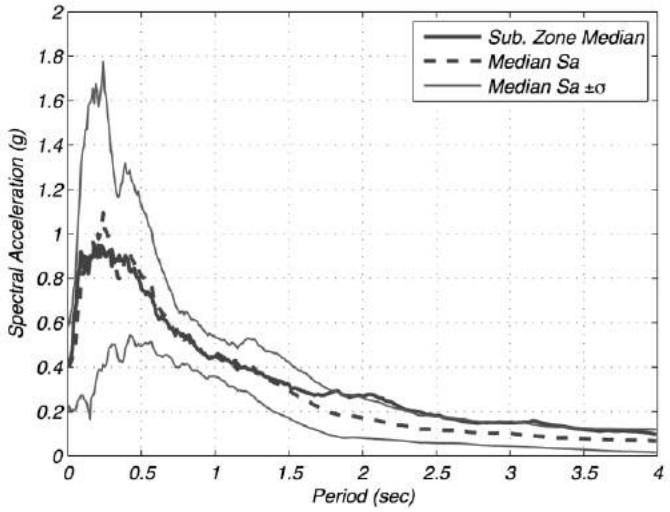

Figure 3.5. Response spectrum for 48 shallow crustal earthquake motions plotted against the previously determined subduction zone median response spectrum, which was used at the target to scale the shallow crustal earthquake motions.

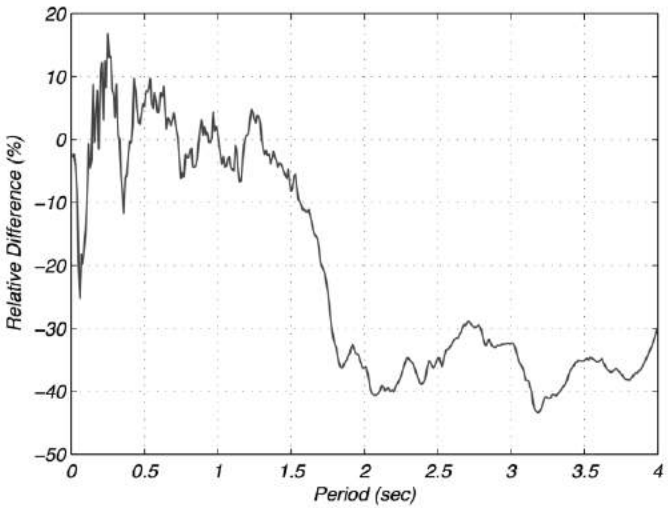

Figure 3.6. The relative difference between the median response of the shallow crustal and subduction zone spectra.

3.3 Soil Sites

For both the longitudinal and transverse soil-bridge models, the soil continuum is represented by a 20 m tall by 1 m wide, two-dimensional plane-strain uniform mesh, far-field soil column atop a dense bedrock layer representing the model boundary. The geometry of the entire soil column and the individual elements of the soil mesh do not change with differing site-soil conditions. However, the biaxial material model, which governs element and soil column response, does change with soil-site conditions.

For both the longitudinal and transverse soil-bridge models, the soil continuum is represented by a 20 m tall by 1 m wide, two-dimensional, plane-strain, uniform mesh, far-field soil column atop a dense bedrock layer representing the model boundary. The geometry of the entire soil column and the individual elements of the soil mesh do not change with differing site-soil conditions. However, the biaxial material model, which governs element and soil column response, does change with soil-site conditions.

Suggested input parameters for the PDMY constitutive model have been proposed by Yang *et al.* (2003). The constitutive modeling parameters are provided for the dense (D_R = 90 percent) and loose (D_R = 35 percent) sands in Table 3.1. The non-liquefiable site-soil condition was modeled homogeneously with the PDMY dense (D_R = 90 percent) sand, which was adapted from a similar site-soil presented in Barbosa *et al.* (2014). The liquefiable soil-site, which is illustrated in Figure 3.7, incorporates a 4 m loose (D_R = 35 percent) sand liquefiable layer, which is overlain and underlain by a non-liquefiable dense (D_R = 90 percent) sand with 3 m and 13 m heights, respectively.

The 1 m by 1 m "9 u-p" quadrilateral soil mesh elements are illustrated in Figure 3.8. The "9 u-p" denotes nine nodes, where degrees of freedom define the soil-skeleton displacement (u) and pore water pressure (p) coupling. The 9-node elements use four Gaussian integration points. The pore water pressure is calculated at each of the four corner nodes for the quadrilateral element, and the horizontal and vertical soil-skeleton displacement is determined at every node.

Each element has an associated out-of-plane thickness. The out-of-plane thickness is required to assign body masses. The depth of the elements differs for the longitudinal and transverse models and was assigned as roughly ten times the breadth of the structural model. The structural breadths of the longitudinal and transverse models are 10.36 m and 31.7 m, respectively. The respective quadrilateral thicknesses were determined to be 100 m for the longitudinal model and 300 m for the transverse model. Slight response differences occur when assigning multiplication factors other than 10 for the structural breadth. These differences can be attributed to the dashpot couple, whose description is forthcoming in Section 3.6.

Table 3.1. Soil pressure dependent multi-yield (PDMY) parameters for fully saturated dense (D_R = 90 percent) and loose (D_R = 35 percent) sands (Yang *et al.* 2003).

PDMY Parameters	Dense Sand	Loose Sand
Material Type	PDMY	PDMY
Pressure Dependent Coeff., d	0.5	0.5
Relative Density, D_R	90%	35%
Friction Angle, ϕ' (deg)	40	29
Soil Mass Density ρ_s (Mg/m3)	2.1	1.7
Phase Transformation Ang., φPT (deg)	27	27
Fluid Mass Density, ρ_w (Mg/m^3)	1.0	1.0
Contraction Coeff., C	0.03	0.21
Shear Modulus, G (kPa)	1.3×10^5	5.5×10^4
Dilation Coeff., d_1	0.8	0
Dilation Coeff., d_2	5	0
Shear Wave Velocity, Vs (m/s)	250	220
Soil Bulk Modulus, B (kPa)	3.9×10^5	5.5×10^5
Horizontal Permeability, K_h (m/s)	5×10^{-5}	5×10^{-5}
Vertical Permeability, K_v (m/s)	5×10^{-5}	5×10^{-5}
Liquefaction Coeff., L_1 (kPa)	0	10
Liquefaction Coeff., L_2	0	0.02
Liquefaction Coeff., L_3	0	1
Peak Shear Strain, γ_p	0.1	0.1
Void Ratio, e	0.45	0.85
Reference Pressure, P'_r (kPa)	80	80
Number of Yield Loci	20	20

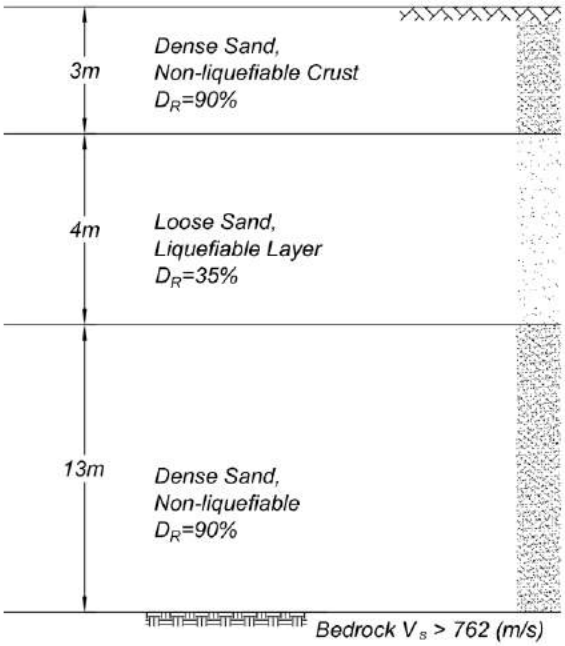

Figure 3.7. Liquefiable soil profile.

The height, *h*, of the individual elements (i.e., 1 m x 1 m) within the soil column was determined with the relationship proposed by Seed (1987),

$$h = \frac{V_s}{8 f_{\max}} \ , \tag{3.2}$$

where V_s is the shear wave velocity in m/s of the weakest layer, and f_{max} is largest expected frequency in Hertz. The lowest expected shear wave velocity provided in Table 3.1 is 220 m/s, and the highest expected frequency, which is typically bounded by earthquake motion filtering, is 25 Hz. Using Equation 3.2, the element height was calculated to be 1.1 m. A 1 m height was selected rather than the calculated value of 1.1 m to ensure the 9 node quadrilateral elements are uniformly sized.

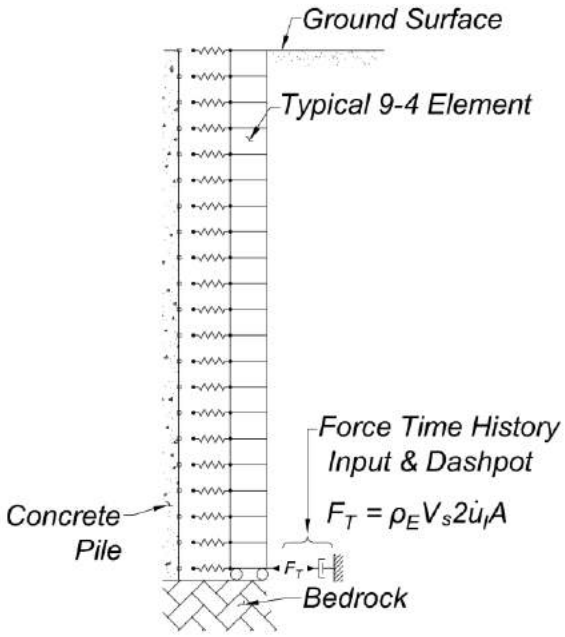

Figure 3.8. Generalized view of the far-field soil column modeled using 9-4 quadrilateral elements. Shown with lateral p-y soil interface springs. Not shown, vertical t-z, and end bearing q-z springs.

A shear beam assumption is commonly used to model soil columns subjected to dynamic excitation. The shear beam assumption requires that soil at equivalent depths below the ground surface have equal lateral and vertical displacements. Accordingly, the left and right sides of the soil column cannot displace laterally or vertically in opposite directions. Implementing the shear beam assumption in OpenSees is achieved by using the multi-point constraint command, *equalDOF*. Using the *equalDOF* command, nodes at equivalent depths are constrained to have identical lateral and vertical displacements as the master node.

A sensitivity analysis was performed on the soil column to determine how the number of 1 m by 1 m quadrilateral elements influences numerical results. To test mesh sensitivity, the soil-bridge system response for a 20 m by 20 m soil column with 400 quadrilateral elements was compared to the 20 m by 1 m soil column with 20 quadrilateral elements presented herein. The mesh comparison was performed using the same shallow crustal earthquake motion and the non-

liquefiable site-soil conditions. Figure 3.9 shows the recorded deck displacement time series for the two soil column sizes (i.e., 20 m by 20 m and 20 m by 1 m). The total mass of the 20 m by 20 m and 20 m by 1 m soil columns is the same for both analyses. The mass for the larger 20 m by 20 m soil column is distributed over a much larger area (400 m^2), compared to that of the 20 m by 1 m soil column (20 m^2). Although the displacement responses of the 20 m by 20 m and 20 m by 1 m soil columns are not identical, agreement between results is evident. The peak displacements for both models occurs at roughly the same time (17.2 s), and the absolute difference between peaks is 8 percent. The differences in displacement response for the 20 m by 20 m and 20 m by 1m soil columns shown in Figure 3.9 is attributed to the mass density of the soil. Both soil columns considered have identical masses, but the 20 m by 20 m soil column distributes the mass over a much larger number of elements. Without the large soil-mesh area, mass is then concentrated near the pile foundation with the 20 m by 1 m soil column. Although the use of the smaller soil column may be perceived as a modeling kludge, it has significantly lower computational cost compared to the 20 m by 20 m soil column. The 400 element soil column with 20 times greater the number of elements as the 20 element column required 6 times the computational time. In summary, although high performance computing can minimize computational time, the differential cost between soil columns does not justify the use of the 20 m by 20 m soil column.

3.4 Soil-Pile Interface

The soil-structure interface springs transmit vertical gravity (t-z and q-z) and seismically induced lateral loads (p-y) from the structural elements to the soil. The three types of nonlinear one-dimensional springs used to model the soil-pile interface are lateral resisting (p-y), skin

friction (t-z), and end bearing (q-z) springs. The soil spring coefficients are functions of the ultimate capacity of the soil, displacement at which of 50 percent of the ultimate strength is mobilized (y_{50}), and drag resistance with a fully mobilized gap (c_d). In OpenSees, the one-dimensional springs are defined by *PySimple1*, *TzSimple1*, and *QzSimple1*. The same one-dimensional springs were used for both the liquefiable and non-liquefiable site-soil profile, but different methodologies were used to calculate the required input parameters.

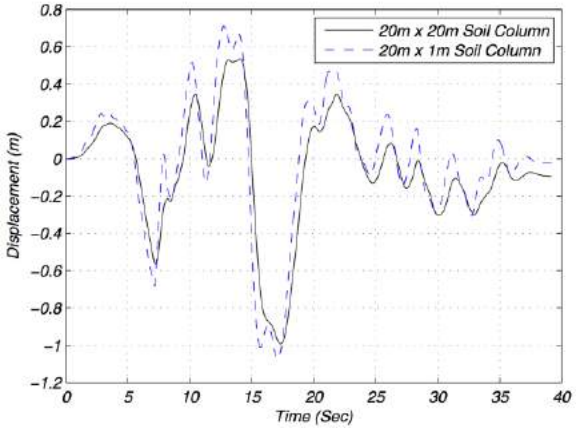

Figure 3.9. Deck displacement time series comparison for 20 m by 20 m and 20 m by 1 m mesh for the same shallow crustal earthquake motion (Irpinia, Italy-01).

A comprehensive discussion of p-y spring formulation is provided Reese *et al.* (1974) and Mosher (1984) for t-z springs. The values for the springs coefficients were determined with the friction angle (ϕ') and relative density (D_R) of the material. The t-z springs were developed from recommendations by Mosher (1984). The inputs for the p-y interface spring type was developed from recommendations presented by the American Petroleum Institute (API 1993) for clean, cohesionless sands. Additional modifications to the p-y spring coefficients were implemented in accordance with Boulanger *et al.* (1999). The Boulanger *et al.* (1999) modification increases the calculated sub-grade soil modulus at larger overburden effective stresses by a multiplier factor of,

$$K_{MOD} = \sqrt{\frac{50\ \text{kPa}}{\sigma'_v}}\ , \tag{3.3}$$

where σ'_v is the effective overburden stress at the point of interest in kPa. The soil-interface springs for the non-liquefiable soil-site were developed following the model presented in by Barbosa *et al.* (2014). Table 3.2 and Table 3.3 summarizes the calculated parameters for the p-y and t-z springs.

Table 3.2. Summary of one-dimensional lateral p-y soil-interface spring values for the non-liquefiable site-soil conditions

Depth (m)	L_t (m)	σ'_v (kPa)	$\bar{A}$	c_σ	$P_{u,1}$ (kN)	$P_{u,2}$ (kN)	P_{ult} (kN)	y_{50} (mm)
0.5	0.5	5.4	2.52	3.04	99	1584	49	0.34
1	1	10.8	2.13	2.15	223	2674	223	1.1
2	1	21.6	1.53	1.52	481	3844	481	1.6
3	1	32.4	1.15	1.24	725	4340	725	2
4	1	43.2	0.95	1.08	1000	4786	1000	2.4
5	1	54	0.88	0.96	1394	5558	1394	3
6	1	64.7	0.88	0.88	1944	6639	1944	3.8
7	1	75.5	0.88	0.81	2592	7745	2592	4.7
8	1	86.3	0.88	0.76	3334	8851	3334	5.7
9	1	97.1	0.88	0.72	4167	9958	4167	6.7
10	1	107.9	0.88	0.68	5094	11064	5094	7.8
11	1	118.7	0.88	0.65	6114	12171	6114	8.9
12	1	129.5	0.88	0.62	7226	13277	7226	10.1
13	1	140.3	0.88	0.6	8431	14384	8431	11.3
14	1	151.1	0.88	0.58	9728	15490	9728	12.5
15	1	161.9	0.88	0.56	11119	16597	11119	13.8
16	1	172.7	0.88	0.54	12602	17703	12602	15.2
17	1	183.4	0.88	0.52	14178	18809	14178	16.6
18	1	194.2	0.88	0.51	15846	19916	15846	18
19	1	205	0.88	0.49	17607	21022	17607	19.5
20	0.5	215.8	0.88	0.48	19461	22129	9731	10.5

L_t -tributary length for each spring; σ'_v -vertical effective stress
$\bar{A}$ -empirical adjustment factor; c_σ - empirical adjustment factor
$p_{u,1,2}$ -ult. strength accounting for depth effects; y_{50} -horiz. disp. at which 50% of ult. strength is mobilized

Table 3.3. Summary of one-dimensional vertical t-z soil-interface spring values for the non-liquefiable site-soil conditions

Depth (m)	L_t (m)	σ'_v (kPa)	T_{ult} (kN)	Z_{50} (mm)
0.5	0.5	5.4	2.3	0.7
1	1	10.8	9	0.7
2	1	21.6	18	0.7
3	1	32.4	27	0.7
4	1	43.2	36	0.7
5	1	54	45	0.7
6	1	64.7	54	0.7
7	1	75.5	63	0.7
8	1	86.3	72	0.7
9	1	97.1	81	0.7
10	1	107.9	90	0.7
11	1	118.7	99	0.7
12	1	129.5	108	0.7
13	1	140.3	117	0.7
14	1	151.1	126	0.7
15	1	161.9	135	0.7
16	1	172.7	144	0.7
17	1	183.4	153	0.7
18	1	194.2	162	0.7
19	1	205	171	0.7
20	0.5	215.8	90	0.7

L_t - tributary length for each spring
σ'_v - vertical effective stress
T_{ult} - ultimate vertical strength
Z_{50} - Vert. Disp. at 50% mobilized strength

Soil strength is significantly reduced in the presence of and immediately adjacent to a liquefiable layer. Loss of strength in these layers is implemented in OpenSees by reducing the ultimate strength (p_{ult}) of the nonlinear p-y springs with a procedure outlined by McGann *et al.* (2011). Rather than deriving novel p-y springs for coarse-grained soils, McGann *et al.* (2011)

suggests dimensionless parameters that reduce the strength and stiffness of established p-y springs for homogeneous soil profiles to account for a liquefiable soil layer. The strength and stiffness reduction parameters are different for both the soil atop and underlying the liquefiable layer. As the distance increases from the liquefiable layer, the dimensionless strength and stiffness reduction parameters proposed by McGann *et al.* (2011) approach one, and thus, do not reduce p-y spring resistance. For the calculation of the unreduced p-y springs, McGann *et al.* (2011) suggests the non-liquefiable soil layers (i.e., atop and beneath the liquefiable layer) be used. The p-y spring resistance for the non-liquefiable soil layer were originally calculated for the non-liquefiable site-soil conditions with the homogeneous dense sand (D_R = 90 percent). The unreduced and reduced strength and stiffness of the p-y springs for the liquefiable soil-site profile are given in Table 3.4. Figure 3.10 shows the p-y spring resistance as a function of depth for the liquefiable and non-liquefiable site-soil conditions. It is important to note the p-y springs in the liquefiable layer still provide a minimal lateral resistance. The minimal resistance is required to avoid numerical instability, which would result if the ultimate strength of the nonlinear p-y springs was set to zero.

3.5 Concrete Pile and Column

The pile foundation and bridge column are a 1.1 m diameter reinforced concrete, continuous shaft. The bridge column is 6.1 m in length extending from the ground surface to the support the bridge deck. The pile foundation is 20 m in length and extends from the ground surface to the underlying bedrock. Pile-foundations founded on bedrock are typically socketed into the competent layer. Socketing provides greater end bearing resistance, minimizes settlement, and forces pile failure into the structural elements. Socketing was not considered for

the soil-bridge system due to the complex boundary condition required to correctly model the pile-socket interface.

Table 3.4: Unreduced and reduced strength and stiffness parameters for p-y springs in accordance with McGann *et al.* (2011).The liquefiable layer is highlighted.

Depth (m)	$P_{u,(unreduced)}$ (kN)	$K_{T,(unreduced)}$ (kN)	P_u Reduction Factor	P_T Reduction Factor	$P_{u,(reduced)}$ (kN)	$K_{T,(reduced)}$ (kN)
0.5	49	64041	1	1	49	64041
1	223	90568	1	1	223	90568
2	481	128083	0.99	1	475	127892
3	725	156869	0.54	0.7	392	109765
4	**1000**	**181136**	**0.01**	**0.1**	**10**	**18114**
5	**1394**	**202517**	**0.01**	**0.1**	**14**	**20252**
6	**1944**	**221846**	**0.01**	**0.1**	**19**	**22185**
7	**2592**	**239621**	**0.01**	**0.1**	**26**	**23962**
8	3334	256166	0.92	1	3054	256156
9	4167	271705	0.96	1	4009	271705
10	5094	286402	0.98	1	5006	286402
11	6114	300381	0.99	1	6066	300381
12	7226	313737	1	1	7200	313737
13	8431	326548	1	1	8417	326548
14	9728	338875	1	1	9721	338875
15	11119	350769	1	1	11115	350769
16	12602	362273	1	1	12600	362273
17	14178	373422	1	1	14177	373422
18	15846	384248	1	1	15846	384248
19	17607	394778	1	1	17607	394778
20	9731	405033	1	1	9731	405033

$P_{(unreduced,reduced)}$ -ult. strength of p-y spring
$K_{(unreduced,reduced)}$ -stiffness of p-y spring

Both the pile and column are modeled with nonlinear stiffness-based elements, which were implemented in OpenSees with the *dispBeamColumn* element. The pile is discretized into 20, 1 m length elements to match the vertical dimension of the nine node quadrilateral soil elements. The one-dimensional soil-interface springs attach the quadrilateral soil elements to end nodes of the pile elements. The 6.1 m column is divided into 6 equal (1.02 m) length elements. It

was determined that six elements satisfied h-refinement requirements for stiffness-based elements.

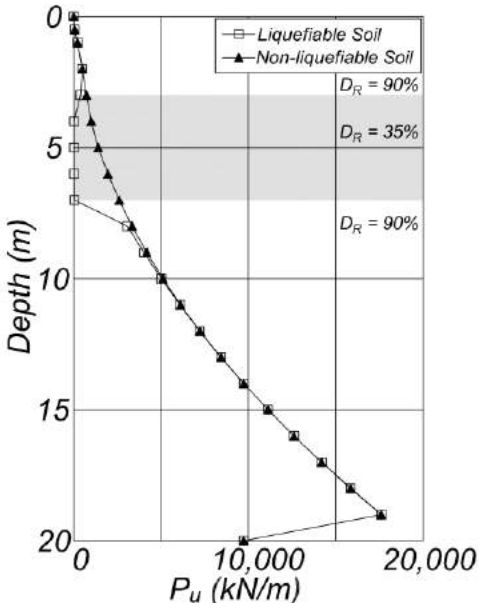

Figure 3.10: Comparison of the p-y springs resistance as a function of depth for the non-liquefiable and liquefiable soil profiles

Figure 3.11 shows the cross section for the continuous concrete shaft used for the column and pile foundation. The modeled shaft corresponds to a Caltrans Type I drilled shaft. The design concrete strength is 28 MPa, and 18 equally spaced #10 ASTM A706 Grade 60 (420 MPa) longitudinal bars are circularly arranged in (Figure 3.11), which gives a reinforcement ratio is 1.5 percent. The longitudinal bars have a Young's modulus of 200 GPa and a strain hardening ratio of 3 percent. The circular concrete shaft section was designed to support an axial gravity load of 3483 kN which is 7.5 percent of $f'_c A_g$. Transverse spiral reinforcement was added to resist seismic forces and satisfy seismic design requirements.

The longitudinal bars, coupled with the transverse spiral reinforcement illustrated in Figure 3.11, provide confinement for the concrete core, which tends to have significant increases in strength and ductility compared with unconfined concrete (Mander *et al.* 1988). Typically, the

strength increase of the confined concrete core is expressed as the confined strength ratio (*K*) between the unconfined and confined concrete. For the modeled column, *K* is 1.38 (Barbosa *et al.* 2014). The remaining confined concrete parameters (i.e., peak strain, failure strain, failure stress) were determined with relationships proposed by Karthik and Mander (2010) and were consistent with Barbosa *et al.* (2014).

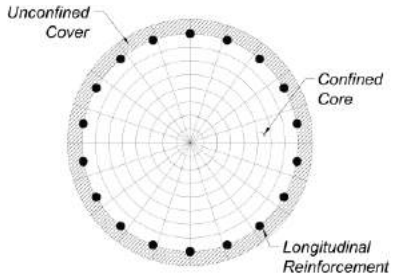

Figure 3.11: Reinforced concrete column and pile cross section

The steel reinforcement constitutive model is defined by the Menegotto and Pinto (1973) constitutive model with modifications by Filippou *et al.* (1983). In OpenSees, the modified Menegotto-Pinto material model is designated by *Steel02*. The concrete constitutive model was proposed by Yassin (1994) and combines Kent and Park (1971) stress-strain envelopes with Karsan and Jirga (1969) unloading and with added linear tension softening. In OpenSees, the concrete material is modeled as *Concrete02*. The concrete constitutive model was defined separately for the unconfined concrete cover and confined concrete core, both of which are illustrated in Figure 3.11.

3.6 Boundary conditions

When seismic waves contact a boundary such as dense/soft material, or large geologic features, portions of the wave energy are absorbed, reflected, and refracted. Reflection and

refraction of seismic energy is routinely modeled numerically, but absorption of energy is not. Additional appropriate damping is required to dissipate (i.e., absorb) energy from the numeric domain. Typically, in computational soil dynamics, an absorbing boundary layer is added to represent the dissipation of seismic wave energy to underlying layers.

Figure 3.8 shows the absorbing boundary conditions for the soil bridge model is illustrated. At the soil-bedrock interface, the earthquake motion is applied as an equivalent force-time history coupled with a viscous dashpot (Zhang *et al.* 2003; Chiaramonte *et al.* 2013). The dashpot at the soil-bedrock interface absorbs wave energy that would typically be dissipated by the elastic half-space. The viscous dashpot coefficient, *c*, can be determined by the relationship,

$$c = \rho_E \upsilon_s A \ , \tag{3.4}$$

where ρ_E is the mass density of the underlying bedrock, υ_s is the shear wave velocity of the bedrock, and *A* is the out-of-plane thickness of the quadrilateral element located at the bedrock layer. The equivalent force-time history, F_{EQU}, is determined by,

$$F_{EQU} = 2\rho_E \upsilon_s \dot{u}_I A \ , \tag{3.5}$$

where $\dot{u}_I$ is the velocity-time series of the respective earthquake motion. The lateral constraint at the soil-bedrock interface is released to allow for the application of the equivalent force time history. An unconstrained lateral degree-of-freedom was accomplished by modeling the soil column at bedrock interface with rollers (see Figure 3.8).

3.7 Bridge Deck and Abutments

The addition of a deck superstructure is the first notable difference between the longitudinal and transverse models. The bridge deck for both the longitudinal and transverse

models was developed from a bridge presented by Shamsabadi *et al.* (2007). The prestressed-post tensioned concrete bridge deck is 10.36 m wide, 1.67 m tall, and consists of two 31.7 m spans. Figure 3.12 shows the bridge deck-cross section proposed by Shamsabadi *et al.* (2007), which is implemented in the soil-bridge model. It is assumed the bridge deck responds linear-elastically to loading due to the high axial stiffness in the deck. Hence, elastic beam-column elements, denoted as *elasticBeamColumn* in OpenSees, are used to model both the longitudinal and transverse bridge deck.

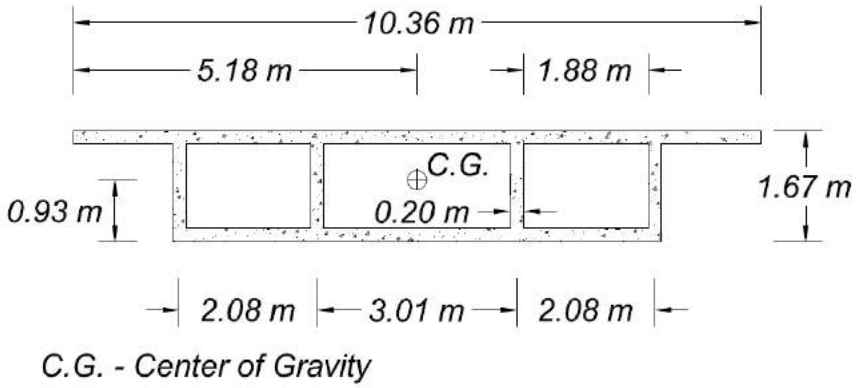

Figure 3.12. Cross section of the bridge deck used for the soil-bridge model (Barbosa *et al.* 2014).

The transverse deck is modeled similar to the section shown in Figure 3.12. Modeling the deck cross section was achieved by defining nodes at each corner, then using a script to discretize elements between defined nodes. The tributary deck mass and vertical gravity loads supported by the center column are assigned to the bridge deck cross section. The mass is uniformly distributed throughout the section in its entirety and vertical gravity loads are applied as distributed loads across the 10.36 m wearing surface.

The longitudinal deck is modeled with 20 (3.17 m) beam-column elements with mass lumped at element end nodes. Gravity loads are applied uniformly along the entire length of the 63.4 m deck. The bridge deck beam-column elements for the longitudinal model are vertically

located at the centroidal height of the cross section shown in Figure 3.12, which is 0.93 m above the top of the column. The connection of the bridge deck to the column was modeled with a very stiff, rigid, linear elastic element. Rigidity was achieved by increasing the stiffness (*EI*) of the bridge deck by a factor of 1000. The purpose of the rigid element is to transmit forces and rotational moments from the deck to the column.

The longitudinal model has abutments at both end of the bridge deck to support vertical gravity loads. At the two abutments, expansion joints are provided between the bridge deck and the abutment back wall to absorb thermal deformations, vibrations, and contraction/shrinkage of construction materials. When the longitudinal displacement at the abutment joints is less than the initial design gap, the abutment behaves as a roller support (i.e., unconstrained lateral degree of freedom). When the longitudinal displacement of the bridge deck exceeds the initial design gap, the gap is closed and "pounding" occurs on the back face of the abutment. The force-displacement behavior of the gap element is illustrated in Figure 3.13. The forces and displacements that the rear abutment backwall can withstand depends on the shear resistance of the back wall and passive strength of the backfilled earth. The soil selected for backfill response is a silty sand, which was presented by Shamsabadi *et al.* (2007). The element shown in Figure 3.13 is modeled in OpenSees using the *ElasticPPGap* uniaxial material, which is used to create a uniaxial spring between the bridge deck and the abutment back wall.

For the bridge system presented in Shamsabadi *et al.* (2007), the material parameters that define the *ElasticPPGap* force-displacement material are: initial gap = 2.54 cm; tangential stiffness (K) = 307 kN/cm/m; and yield force (F_y) = 1397 kN

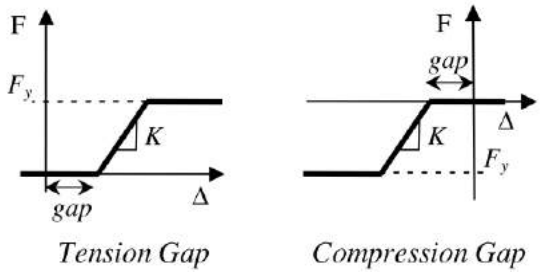

Figure 3.13. Elastic perfectly plastic gap material force displacement response (Barbosa and Silva 2007).

3.8 Fundamental periods and damping

An eigenvalue analysis was required to determine the fundamental periods of the longitudinal and transverse soil-bridge models. The fundamental period of vibration of the longitudinal model and the transverse model are 0.89 s and 1.71 s, respectively. The fundamental periods were required to assign Rayleigh damping, which is characterized by mass and stiffness components (Hall 2006; Charney 2008). The investigated soil-bridge systems are relatively stiff systems (i.e., dense soil and concrete structural elements); therefore, a damping ratio of 2 percent was selected for both the mass and stiffness proportional components of Rayleigh damping. The range of natural frequencies selected for Rayleigh damping were 1.12 Hz to 125 Hz and 0.58 Hz to 125 Hz for the longitudinal and transverse models, respectively. The lower respective frequencies of 1.12 Hz and 0.58 Hz corresponds to the fundamental periods of the longitudinal and transverse models, and the 125 Hz upper bound is the third mode of vibration for the two soil-bridge systems.

3.9 Analysis Framework

The analysis of the nonlinear, finite element longitudinal and transverse soil-bridge models is performed in six stages. In addition to serving as modeling logic, the stages simulate pre-construction and post-construction soil conditions and incorporate staged construction

principles of analysis. The stages presented are identical for both the longitudinal and transverse models until the bridge deck is created.

- Stage 1: In this stage, the global geometry of the soil-bridge system is established. This includes defining the nodes, the PDMY plane-strain material, and the "9-4" u-p quadrilateral elements. Single and multiple point constraints are established during this stage, which includes the roller boundary condition and the *EqualDOF* constraint condition required for the shear beam assumption. Additionally, the one-dimenstional p-y, t-z, and q-z soil-interface springs are defined, but are not attached to the far-field soil column during this stage.
- Stage 2: At beginning of this stage, mass is lumped at the pile, column and bridge deck (longitudinal model only) nodes. The mass is lumped for both the vertical and horizontal degrees-of-freedom. Nodal inertia from rotation is neglected. The pile/column fiber cross section is defined by incorporating the longitudinal reinforcing steel, the confined concrete, and the unconfined concrete with their respective constitutive models. The stiffness-based elements of the pile and the column are defined with the fiber section. The deck line elements of the longitudinal model are created and they are attached to the abutments and atop the reinforced concrete column.
- Stage 3 (transverse model only): During this stage, the deck cross section is defined for the transverse model. This is completed by defining nodes at the corners of the bridge deck cross section and discretizing rigid elements between the user-defined nodes. Similar to the mass assignment in Stage 2, the mass is lumped at the discretized and user defined nodes. The mass at each node contains the tributary mass of the deck.

- Stage 4: During this stage, element and node recorders are defined. The recorded outputs include: displacements, deformations, dynamic and static forces and stress-strain response.
- Stage 5: Initially, this stage begins with application of soil gravity loads to simulate pre-construction soil conditions. Gravity loads are applied to the soil elements as a linear ramp function with a critically damped transient analysis. Critically damping the soil-bridge system simulates a static condition. At the completion of the gravity load analysis the one-dimensional interface springs (i.e., p-y, t-z, and q-z) are attached to the soil column and pile foundation. Once the interface springs have been attached, the deck gravity loads are applied. For the transverse model the deck loads are distributed across the 10.67 m surface. For the longitudinal model, the deck loads are distributed along the 63.4 m deck length. The deck loads are incrementally applied with a linear ramp function, and the peak of the ramp function represents full deck loading. Similar to the soil gravity loads, the analysis is performed with a critically damped system. Critical damping is provided by artificially imposing damping by increasing the Newmark (1959) time integration parameters to 1.5 and 1.0 for β and γ.
- Stage 6: At the beginning of this stage, the dashpot is created. This includes the viscous dashpot material and the redundant nodes that attached the dashpot to the soil column. Finally, the nonlinear dynamic time-history analysis is performed using Newmark constant average integrator ($\beta = 0.25$ and $\gamma = 0.5$). The equilibrium of a nonlinear system cannot be solved for directly; therefore, a solution algorithm is required to approximate equilibrium with an iterative approach. The Krylov-Newton algorithm was selected for the soil-bridge models (Scott and Fenves 2010).

Chapter 4 Results

The focus of this chapter is to use the soil-bridge system presented in 0 to evaluate bridge response to shallow crustal and subduction zone earthquakes. The earthquake motion intensity parameters (i.e., *PGA*, *PGV*, I_a, $D_{5\text{-}95}$, $S_a(T_1,\beta)$, CAV_5) for the 48 shallow crustal and 46 subduction zone earthquake motions were compared to duration-dependent seismic response damage assessments. The effectiveness of each earthquake motion intensity parameter to predict duration-dependent bridge damage was then evaluated.

Peak-drift ratio has been commonly used by researchers and practitioners to describe the peak demand from an earthquake motion on a bridge. For a given bridge, the peak-drift ratio is similar for shallow crustal and subduction zone earthquakes with similar amplitudinal intensity. Accordingly, the duration of an earthquake motion and the number of loading cycles is not fully considered when calculating the peak-drift ratio. To incorporate duration effects, additional demand parameters are established, and the additional demand parameters distinguish the damage from shallow crustal and subduction zone earthquake motions. The first demand parameter, which is a durational demand parameter, counts the number of occurrences when the recorded plastic hinge rotation (θ_{lp}) exceeds the reference yield rotation (θ_Y). The second demand parameter is the area bounded by the reference yield rotation value and recorded plastic hinge rotation.

Plastic hinge rotation, θ_{lp}, is computed by the following expression,

$$\theta_{lp} = \phi \cdot l_p \ , \tag{4.1}$$

where ϕ is the measured curvature and ℓ_p is the effective plastic hinge length. The curvature is recorded during the nonlinear seismic analysis for both the column and pile foundation. Curvature at reference yield is a value that was determined experimentally, and it accounts for

the shaft diameter and yield strength of the longitudinal reinforcing steel. The relationship proposed in Priestly (2003) to calculate the reference yield curvature θ_Y is,

$$\theta_Y = \frac{2.25\grave{o}_y l_p}{D} \ , \tag{4.2}$$

where D is the reinforced concrete shaft diameter, and ε_y is the expected yield strain of the longitudinal reinforcing steel. The plastic hinge length, ℓ_p, suggested by Priestly *et al.* (2007) is equal to $0.08\ell + 0.15 d_b f_y$, where ℓ is the length of the column in meters, d_b is the nominal bar diameter (m), and f_y is the yield strength (MPa) of the longitudinal reinforcing steel. Note that the last term of the plastic hinge length equation accounts for strain penetration effects.

Figure 4.1 and Figure 4.2 show a visual representation of the inelastic excursions for a 30 s shallow crustal earthquake motion (motion 14, Appendix B), and a 300 s subduction zone earthquake motion (motion 28, Appendix A). Figure 4.1 and Figure 4.2 were developed using the longitudinal model with the non-liquefiable site-soil profile. The earthquake motions were selected for their similar amplitudinal intensity parameters (i.e., *PGA*, *PGV*) to illustrate the effect of earthquake motion duration on number of inelastic excursions. The cumulative plastic rotations described below are also shown in Figure 4.1 and Figure 4.2 for reference.

Cumulative plastic rotation (*CPR*) for the bridge model is defined as the area under the plastic rotation time series (θ_{lp}-t) and above the reference plastic hinge rotation time series (θ_Y-t). The expression used to evaluate plastic rotation is,

$$CPR = \int_0^{t_{max}} \langle \chi \rangle \left| \theta_{lp} \right| \mathrm{d}t \quad \text{where} \quad \langle \chi \rangle = \begin{cases} 0 & \text{for} \quad \left| \theta_{lp} \right| < \theta_Y \\ 1 & \text{for} \quad \left| \theta_{lp} \right| \geq \theta_Y \end{cases} \ , \tag{4.3}$$

where t_{max} is the time at the end of strong shaking.

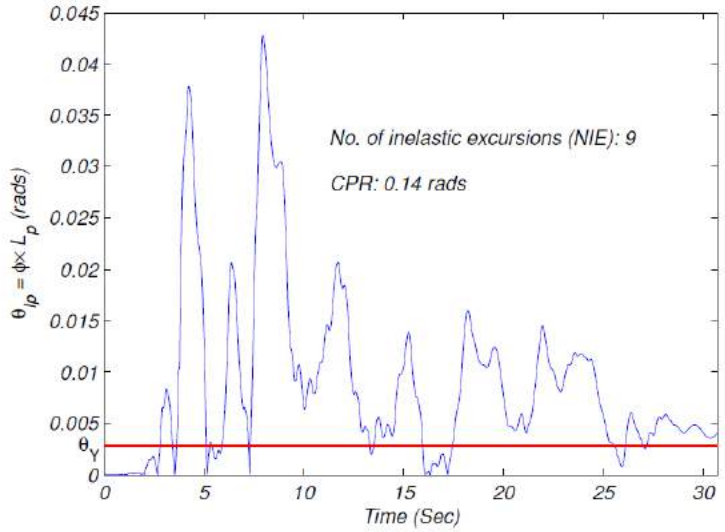

Figure 4.1. Visual illustration of plastic hinge rotation, θ_{lp} for shallow crustal earthquake motion 14, where L_p is the effective plastic hinge, ϕ is the curvature determined at time *t*, and *CPR* is the cumulative plastic rotation.

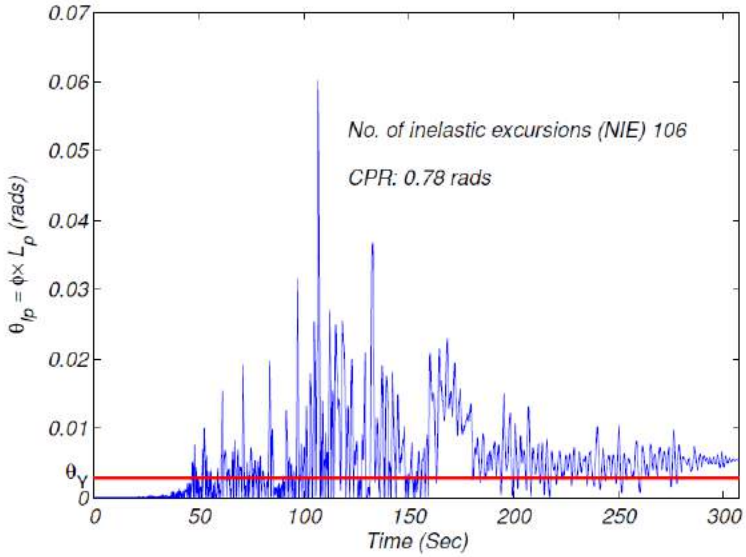

Figure 4.2. Visual illustration of plastic hinge rotation, θ_{lp} for subduction zone earthquake motion 28, where L_p is the effective plastic hinge, ϕ is the curvature determined at time *t*, and *CPR* is the cumulative plastic rotation.

Figure 4.3 through Figure 4.50 show the number of inelastic excursions and cumulative plastic rotation for all earthquake motions plotted against six earthquake motion intensity measures: peak ground acceleration (*PGA*), peak ground velocity (*PGV*), Arias intensity (I_a), significant duration ($D_{5\text{-}95}$), spectral acceleration at the fundamental period [$S_a(T_1,\beta)$], and modified cumulative absolute velocity (CAV_5). Figure 4.3 through Figure 4.50 were generated for each direction (i.e., longitudinal and transverse) and for both site-soil profiles (i.e., liquefiable and non-liquefiable). Additionally, the correlation coefficients for the *NIE*s and *CPR*s for the respective intensity parameters are reported in each figure for the shallow crustal and subduction zone earthquake motions. Table 4.1 through Table 4.4 show correlation coefficients between the earthquake motion intensity parameters and the demand parameters. The correlation coefficients were calculated for each combination of earthquake motion type, model configuration, site-soil condition, and the correlation coefficients were based on the assumption of normally-distributed and lognormally-distributed data. Table 4.5 and Table 4.6 report the number of inelastic excursions and *CPR*s for each earthquake motion considering the different models and site-soil conditions. The means, medians and standard deviations of the *NIE*s and *CPR*s are given in Table 4.7 and Table 4.8.

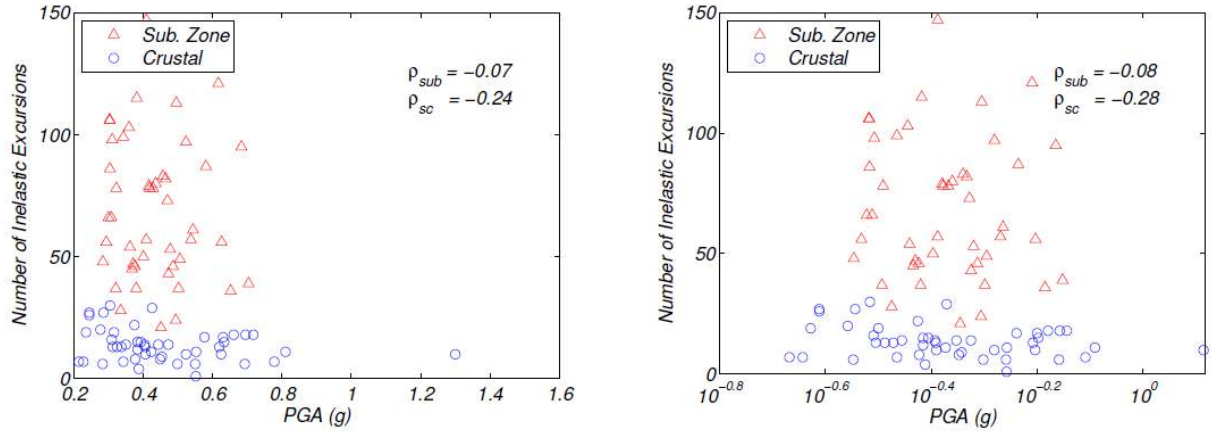

(a) Linear Scale (b) Log Scale

Figure 4.3. Peak ground acceleration of subduction zone and shallow crustal earthquake motions plotted against number of inelastic excursions for the longitudinal model with non-liquefiable site conditions.

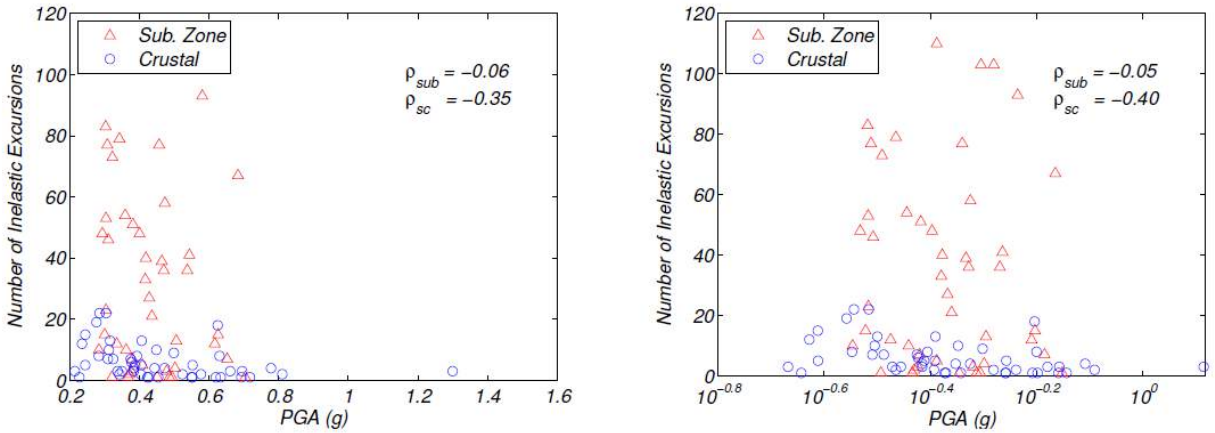

(a) Linear Scale (b) Log Scale

Figure 4.4. Peak ground acceleration of subduction zone and shallow crustal earthquake motions plotted against number of inelastic excursions for the longitudinal model with liquefiable site conditions.

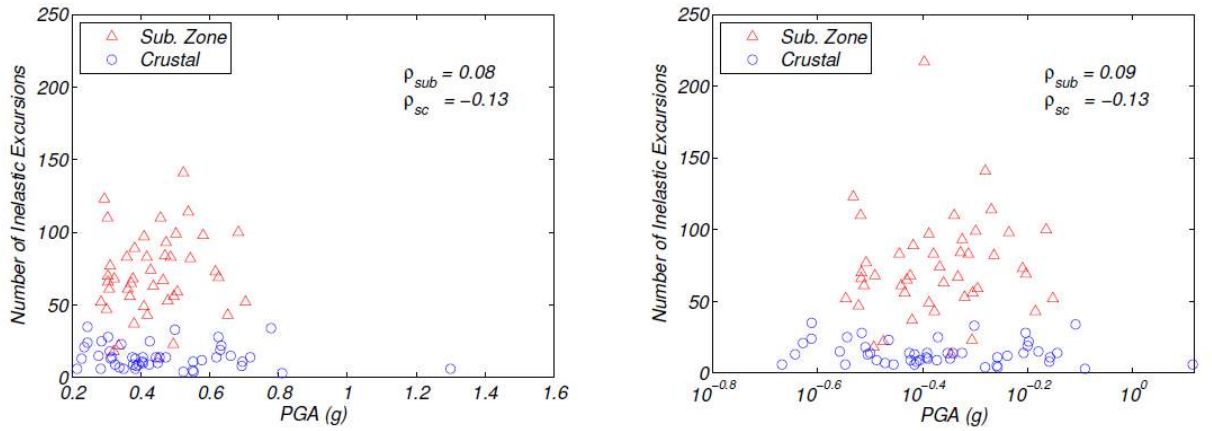

(a) Linear Scale (b) Log Scale

Figure 4.5. Peak ground acceleration of subduction zone and shallow crustal earthquake motions plotted against number of inelastic excursions for the transverse model with non-liquefiable site conditions.

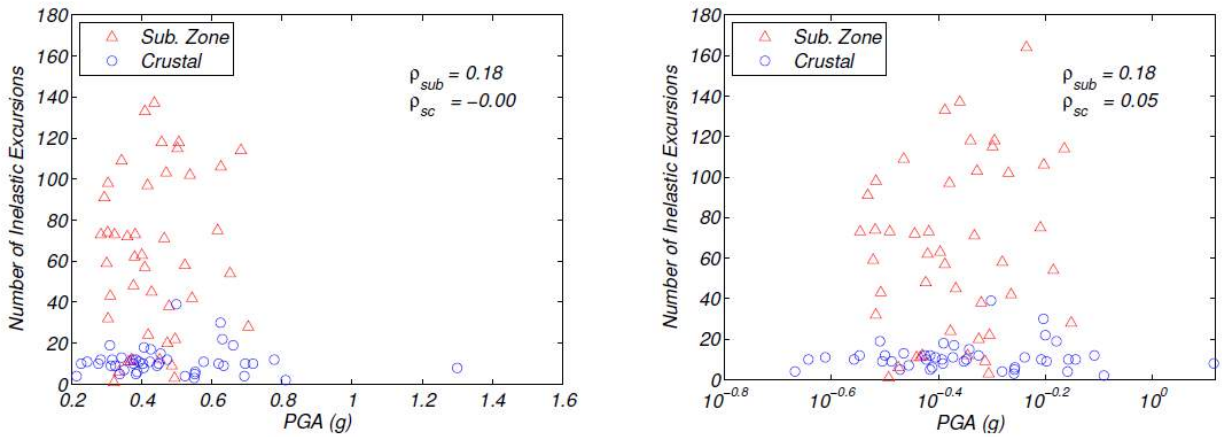

(a) Linear Scale (b) Log Scale

Figure 4.6. Peak ground acceleration of subduction zone and shallow crustal earthquake motions plotted against number of inelastic excursions for the transverse model with liquefiable site conditions.

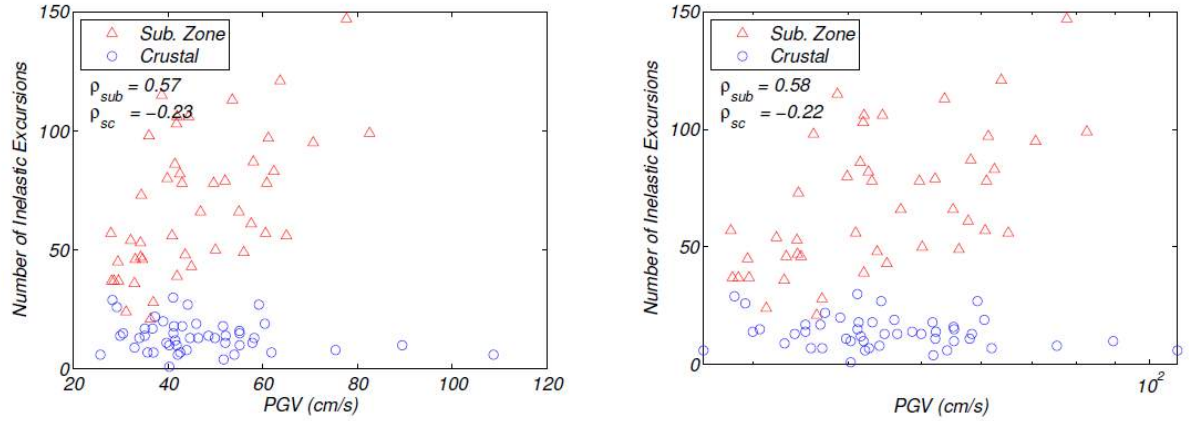

(a) Linear Scale (b) Log Scale

Figure 4.7. Peak ground velocity of subduction zone and shallow crustal earthquake motions plotted against number of inelastic excursions for the longitudinal model with non-liquefiable site conditions.

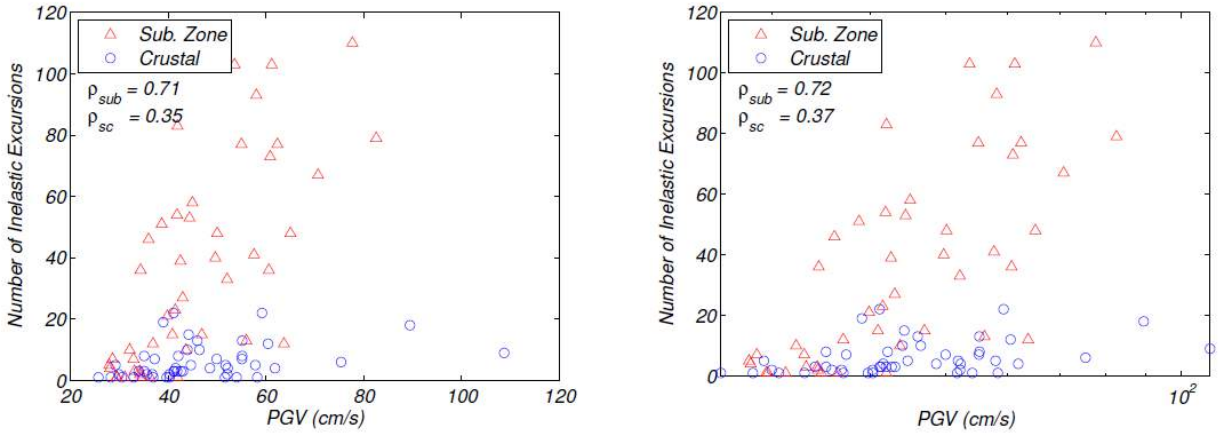

(a) Linear Scale (b) Log Scale

Figure 4.8. Peak ground velocity of subduction zone and shallow crustal earthquake motions plotted against number of inelastic excursions for the longitudinal model with liquefiable site conditions.

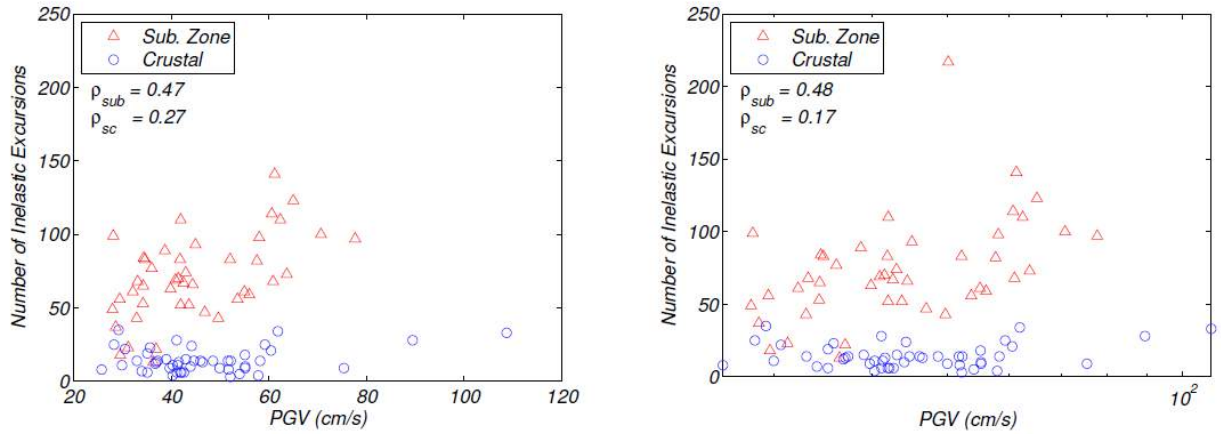

Figure 4.9. Peak ground velocity of subduction zone and shallow crustal earthquake motions plotted against number of inelastic excursions for the transverse model with non-liquefiable site conditions.

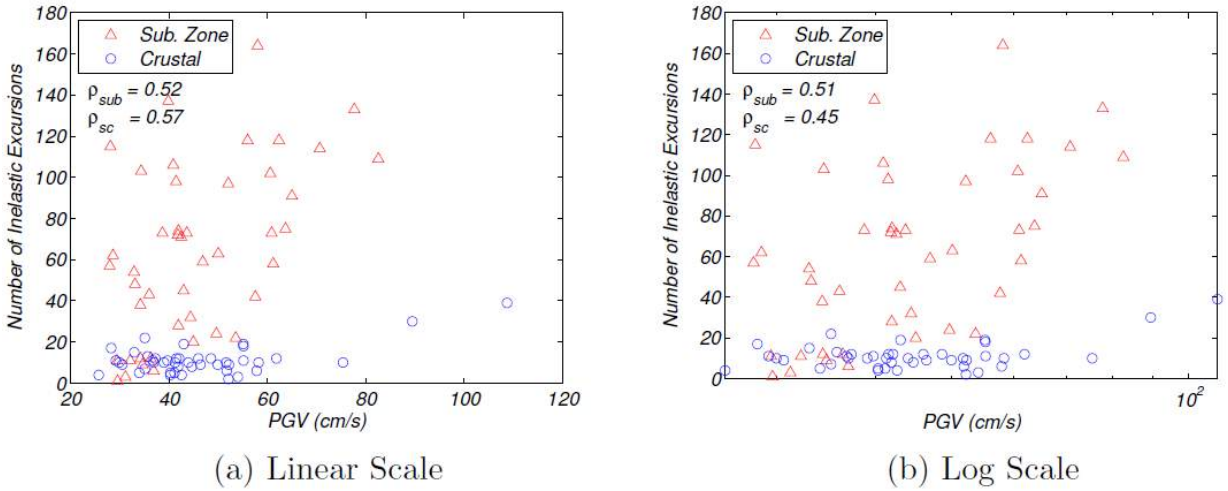

Figure 4.10. Peak ground velocity of subduction zone and shallow crustal earthquake motions plotted against number of inelastic excursions for the transverse model with liquefiable site conditions.

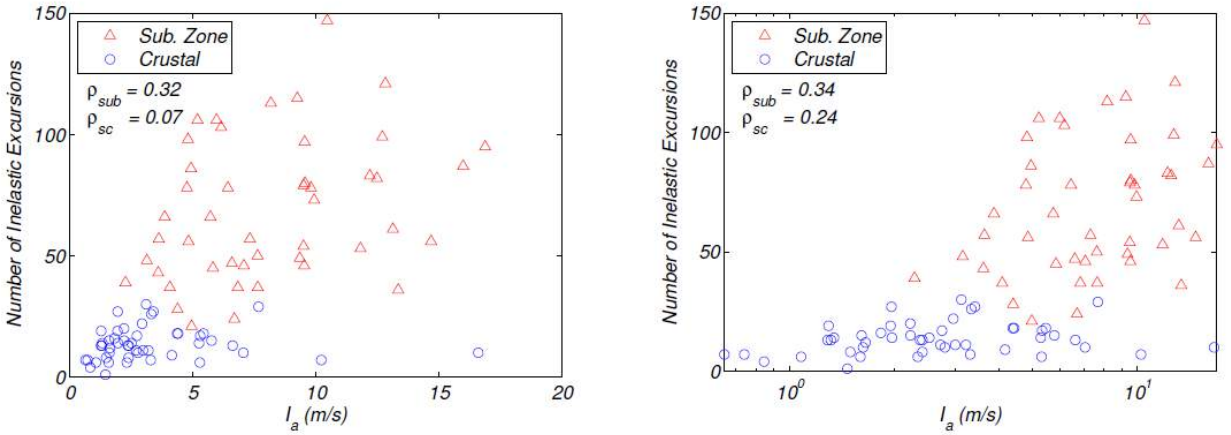

Figure 4.11. Arias intensity of subduction zone and shallow crustal earthquake motions plotted against number of inelastic excursions for the longitudinal model with non-liquefiable site conditions.

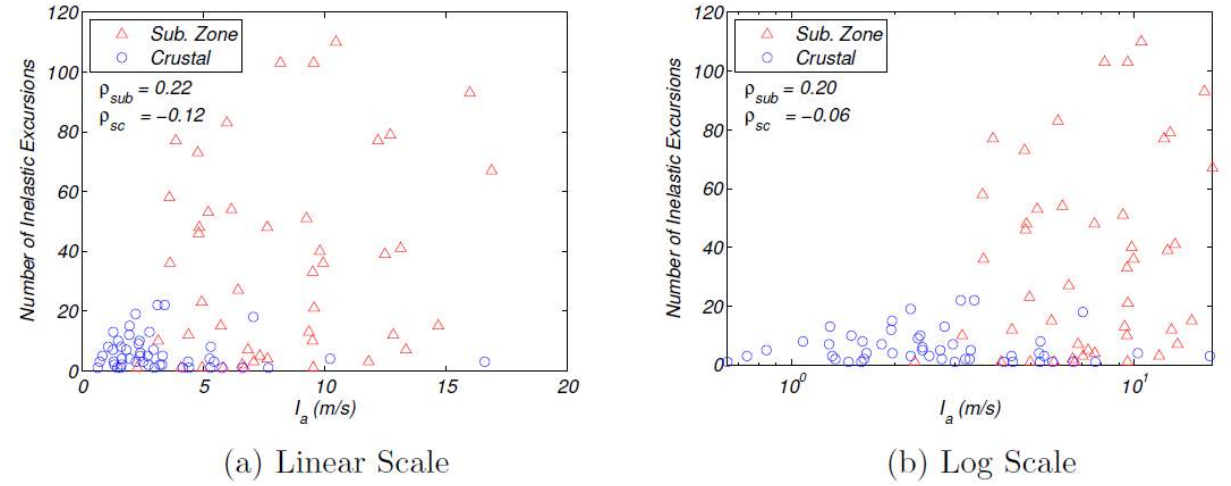

Figure 4.12. Arias intensity of subduction zone and shallow crustal earthquake motions plotted against number of inelastic excursions for the longitudinal model with liquefiable site conditions.

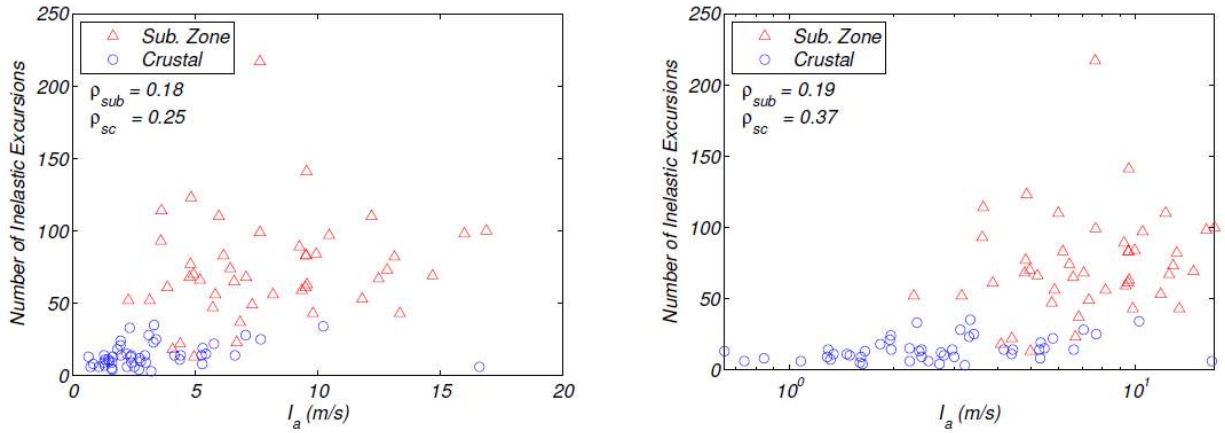

Figure 4.13. Arias intensity of subduction zone and shallow crustal earthquake motions plotted against number of inelastic excursions for the transverse model with non-liquefiable site conditions.

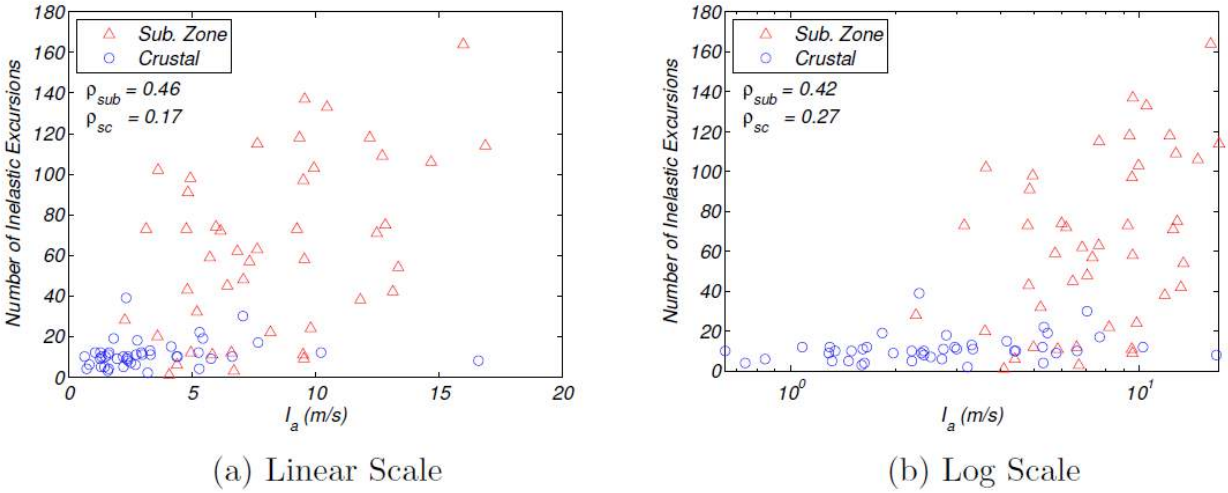

Figure 4.14. Arias intensity of subduction zone and shallow crustal earthquake motions plotted against number of inelastic excursions for the transverse model with liquefiable site conditions.

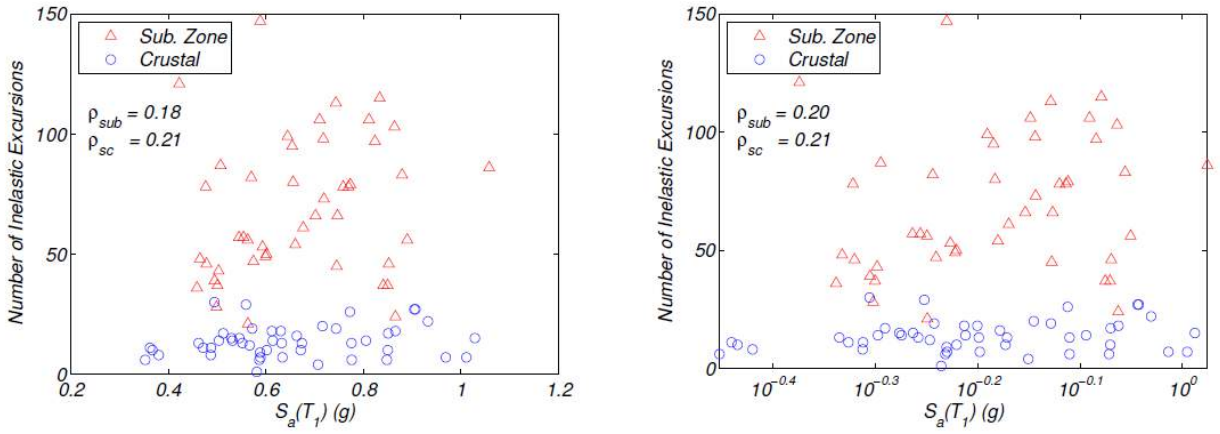

Figure 4.15. Spectral Acceleration at T_1 of subduction zone and shallow crustal earthquake motions plotted against number of inelastic excursions for the longitudinal model with non-liquefiable site conditions.

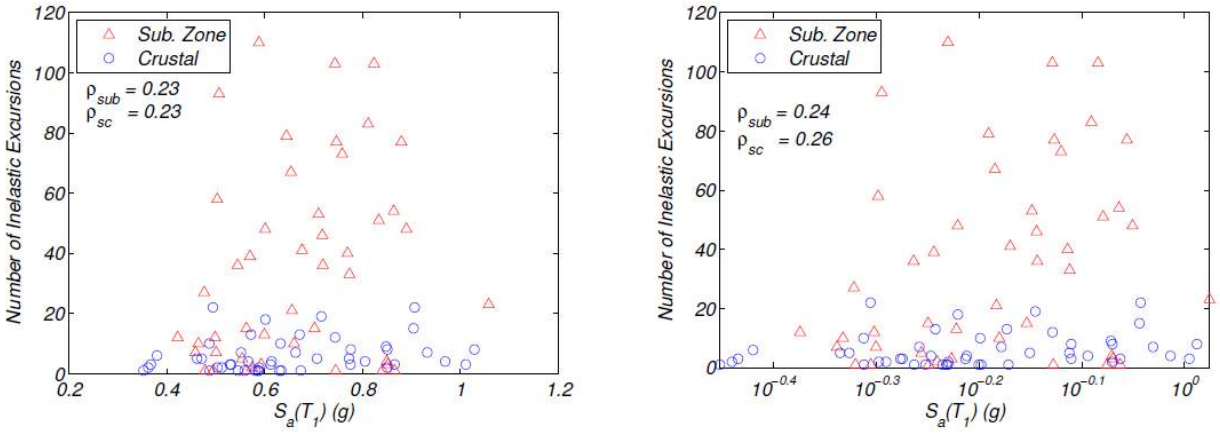

Figure 4.16. Spectral Acceleration at T_1 of subduction zone and shallow crustal earthquake motions plotted against number of inelastic excursions for the longitudinal model with liquefiable site conditions.

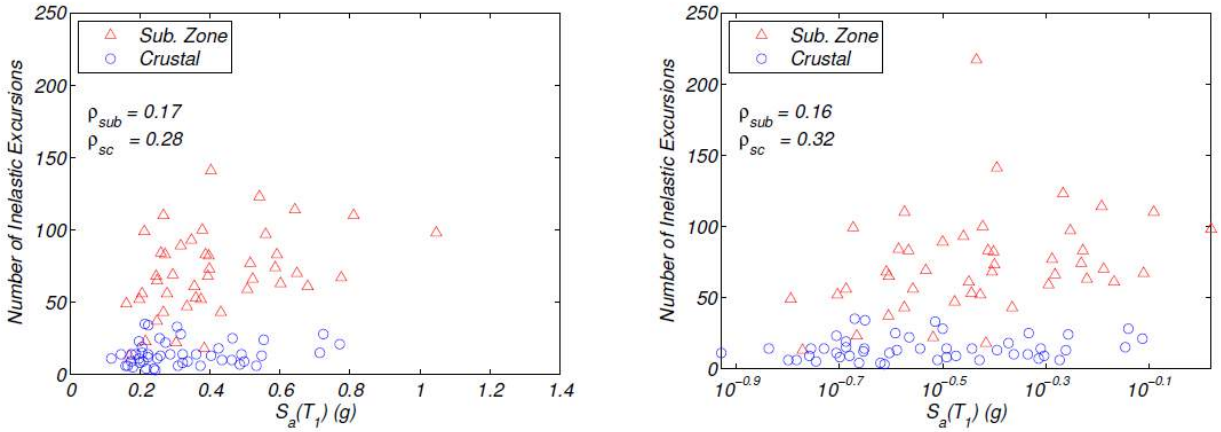

(a) Linear Scale (b) Log Scale

Figure 4.17. Spectral Acceleration at T_1 of subduction zone and shallow crustal earthquake motions plotted against number of inelastic excursions for the transverse model with non-liquefiable site conditions.

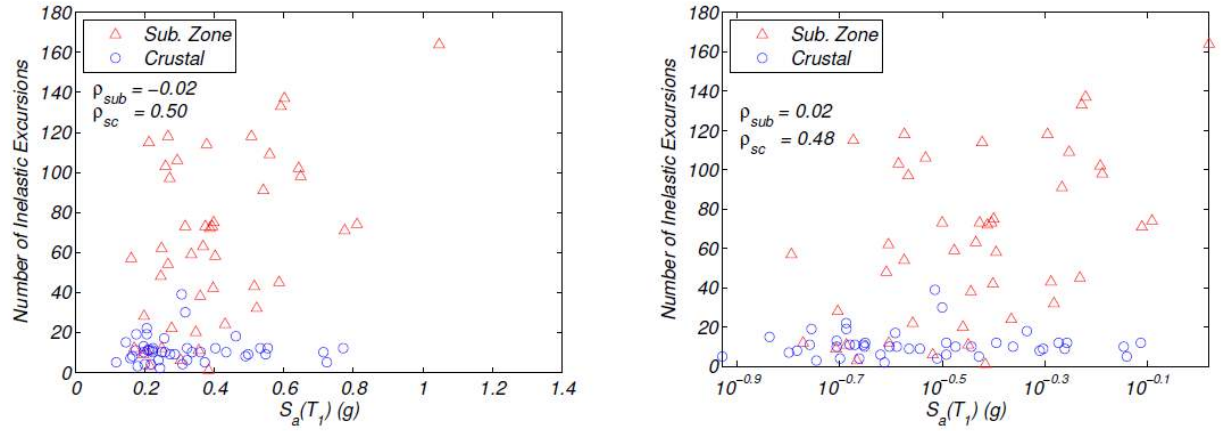

(a) Linear Scale (b) Log Scale

Figure 4.18. Spectral Acceleration at T_1 of subduction zone and shallow crustal earthquake motions plotted against number of inelastic excursions for the transverse model with liquefiable site conditions.

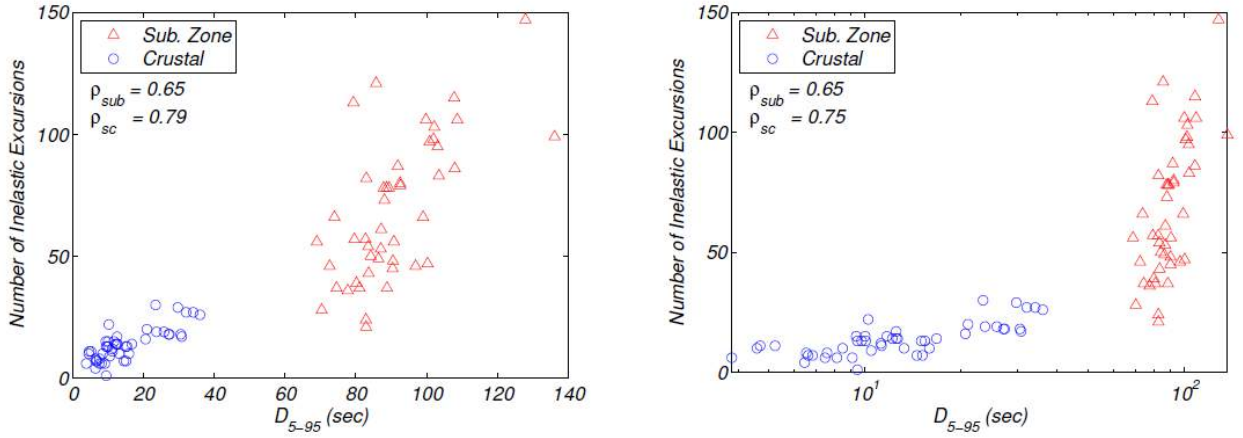

Figure 4.19. Significant duration of subduction zone and shallow crustal earthquake motions plotted against number of inelastic excursions for the longitudinal model with non-liquefiable site conditions.

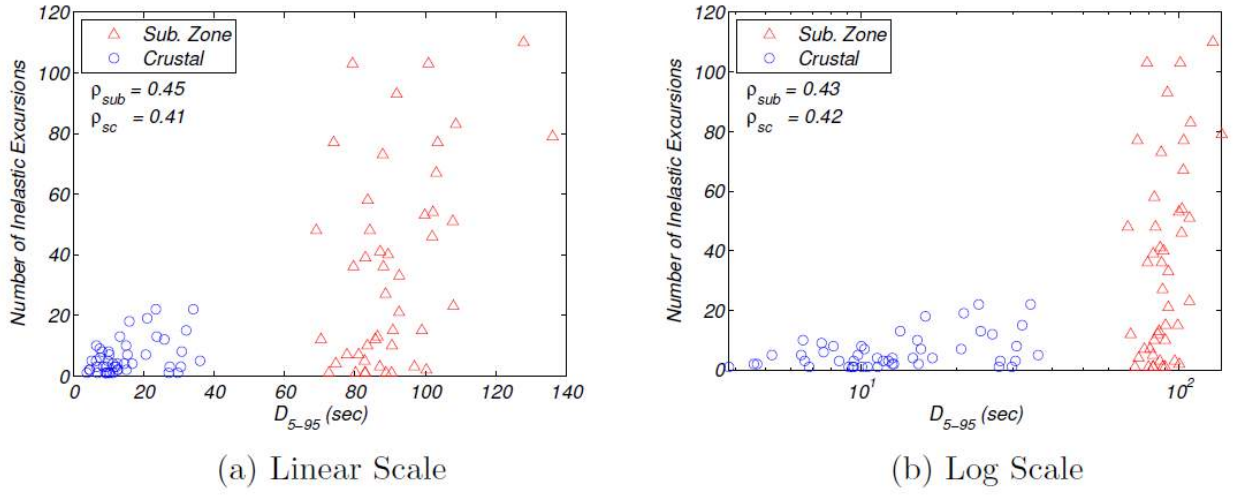

Figure 4.20. Significant duration of subduction zone and shallow crustal earthquake motions plotted against number of inelastic excursions for the longitudinal model with liquefiable site conditions.

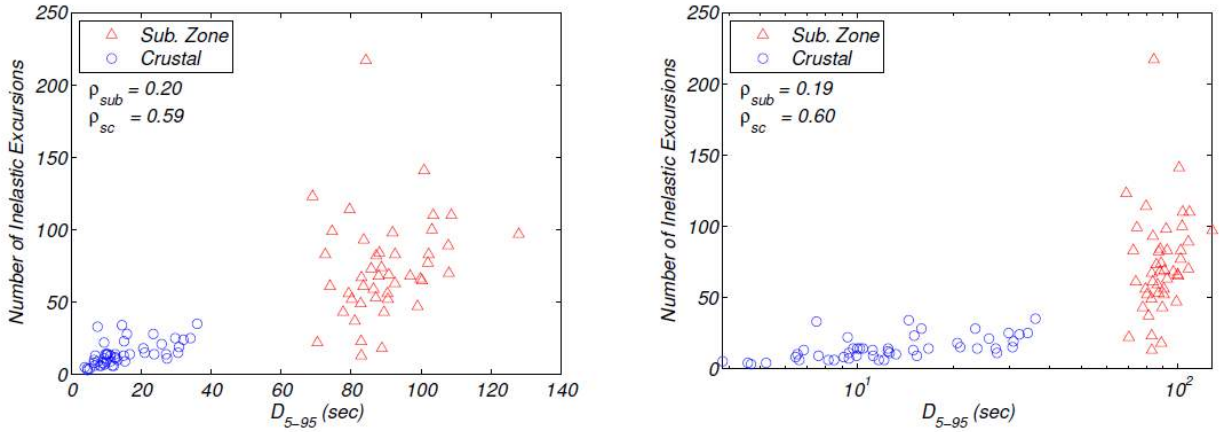

(a) Linear Scale (b) Log Scale

Figure 4.21. Significant duration of subduction zone and shallow crustal earthquake motions plotted against number of inelastic excursions for the transverse model with non-liquefiable site conditions.

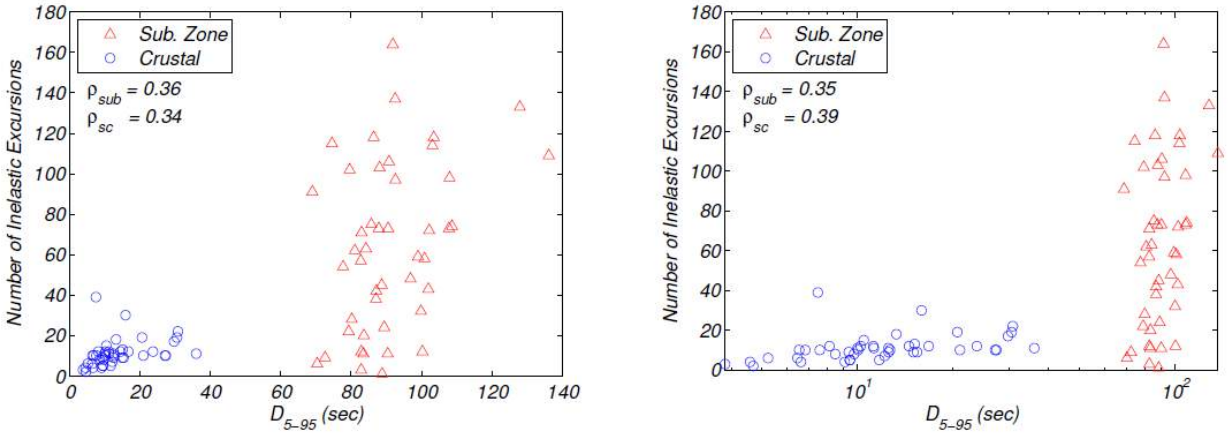

(a) Linear Scale (b) Log Scale

Figure 4.22. Significant duration of subduction zone and shallow crustal earthquake motions plotted against number of inelastic excursions for the transverse model with liquefiable site conditions.

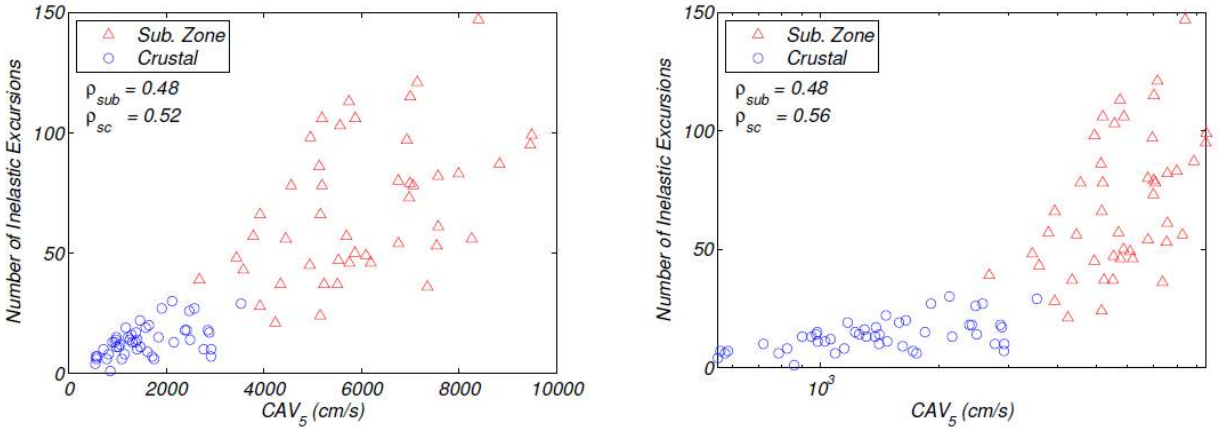

(a) Linear Scale (b) Log Scale

Figure 4.23. Cumulative absolute velocity five of subduction zone and shallow crustal earthquake motions plotted against number of inelastic excursions for the longitudinal model with non-liquefiable site conditions.

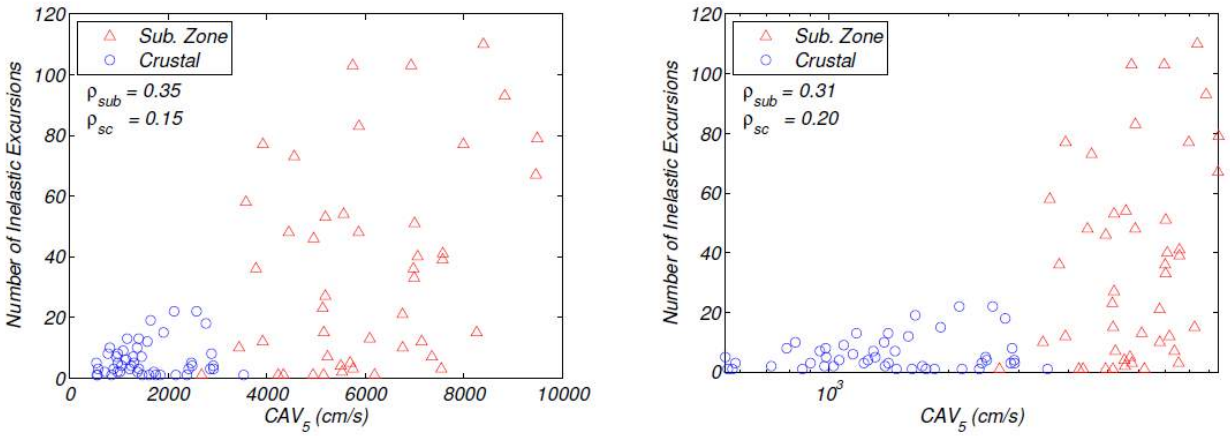

(a) Linear Scale (b) Log Scale

Figure 4.24. Cumulative absolute velocity five of subduction zone and shallow crustal earthquake motions plotted against number of inelastic excursions for the longitudinal model with liquefiable site conditions.

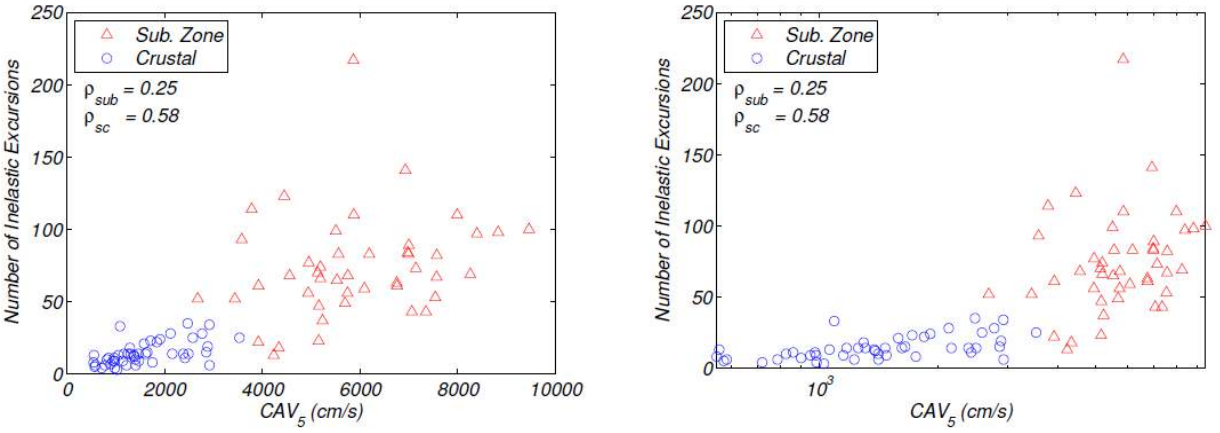

Figure 4.25. Cumulative absolute velocity five of subduction zone and shallow crustal earthquake motions plotted against number of inelastic excursions for the transverse model with non-liquefiable site conditions.

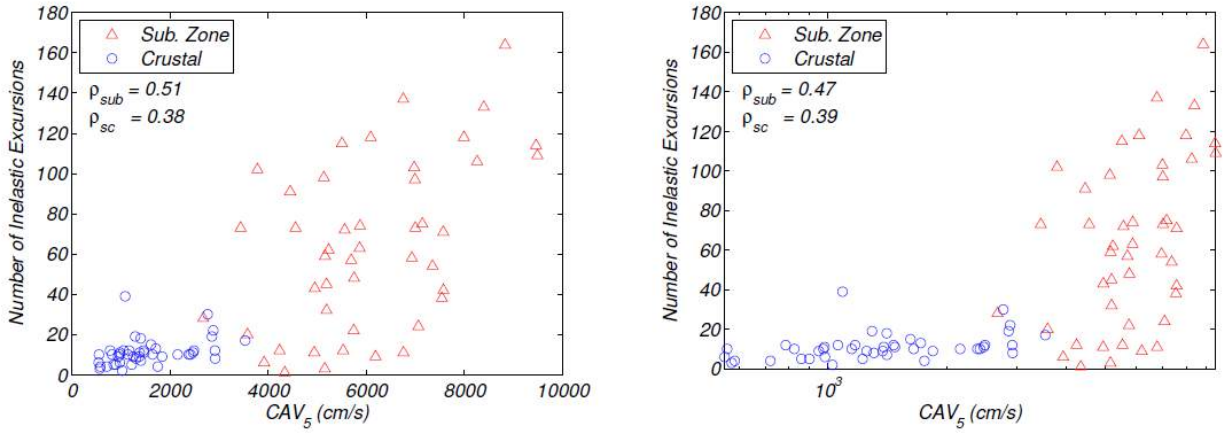

Figure 4.26. Cumulative absolute velocity five of subduction zone and shallow crustal earthquake motions plotted against number of inelastic excursions for the transverse model with liquefiable site conditions.

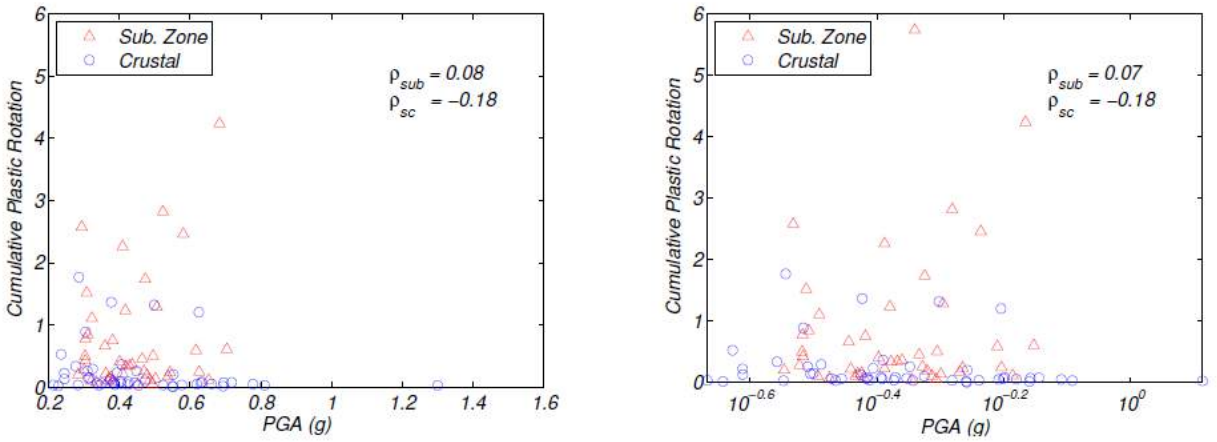

(a) Linear Scale (b) Log Scale

Figure 4.27. Peak ground acceleration of subduction zone and shallow crustal earthquake motions plotted against cumulative plastic rotation for the longitudinal model with non-liquefiable site conditions.

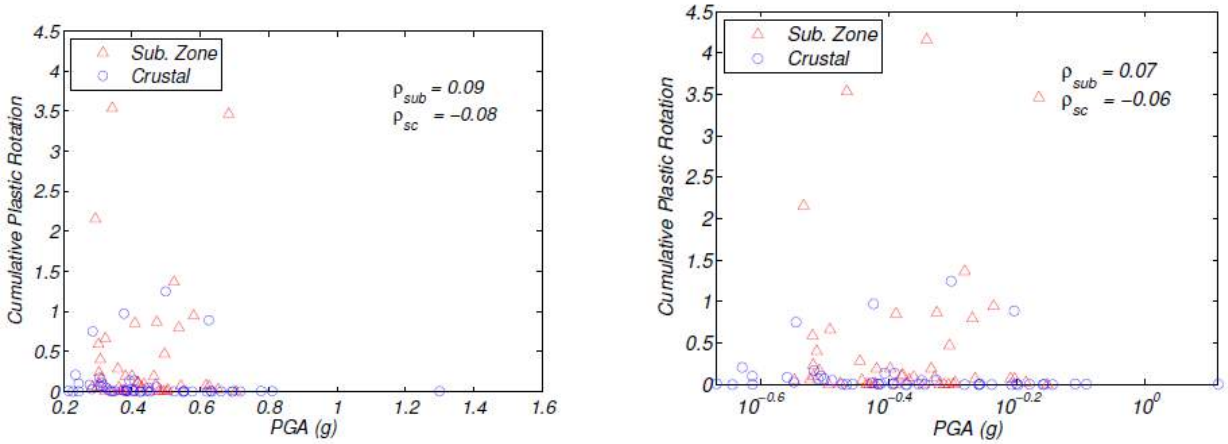

(a) Linear Scale (b) Log Scale

Figure 4.28. Peak ground acceleration of subduction zone and shallow crustal earthquake motions plotted against cumulative plastic rotation for the longitudinal model with liquefiable site conditions.

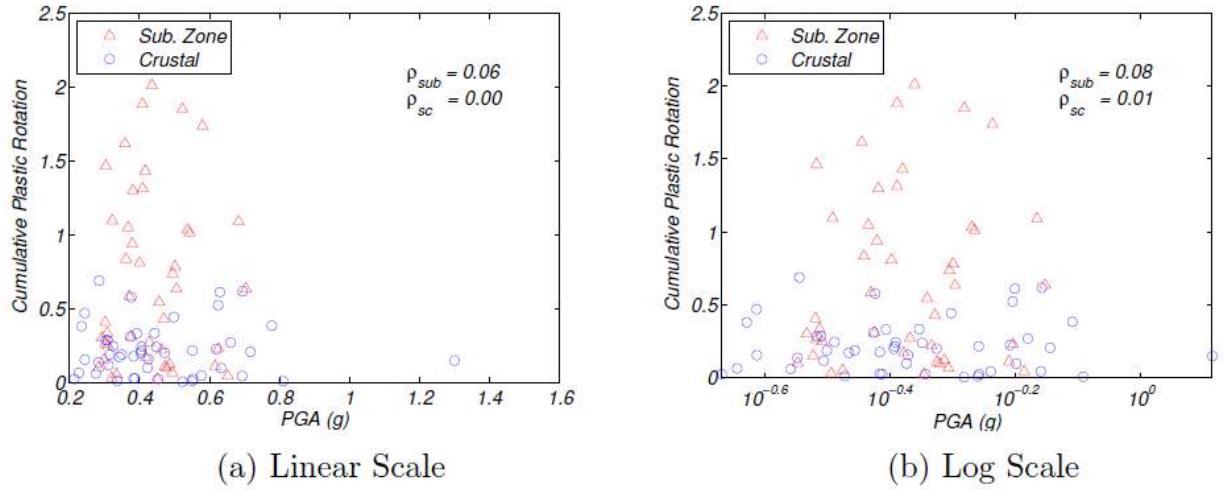

Figure 4.29. Peak ground acceleration of subduction zone and shallow crustal earthquake motions plotted against cumulative plastic rotation for the transverse model with non-liquefiable site conditions.

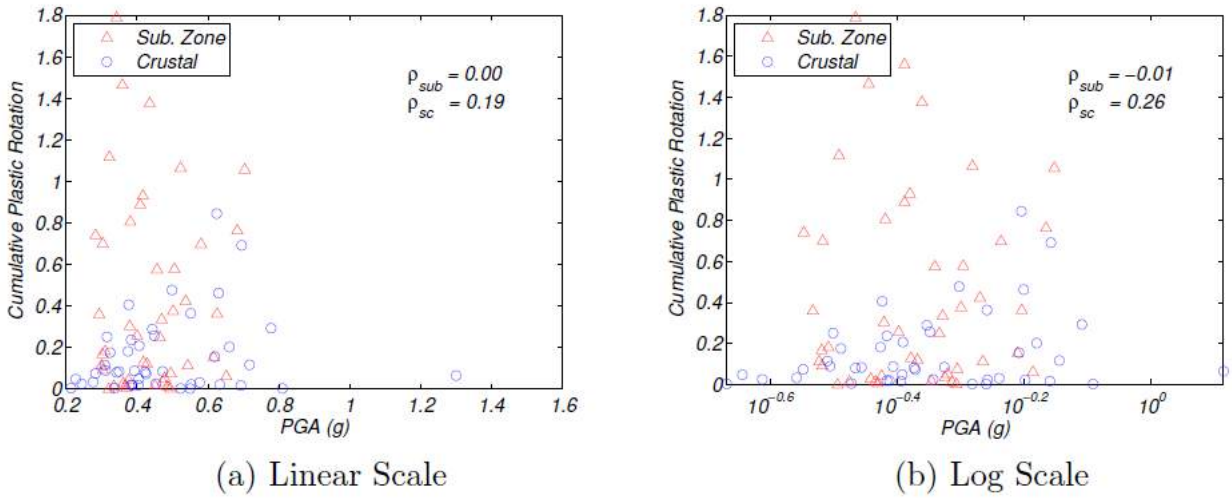

Figure 4.30. Peak ground acceleration of subduction zone and shallow crustal earthquake motions plotted against cumulative plastic rotation for the transverse model with liquefiable site conditions.

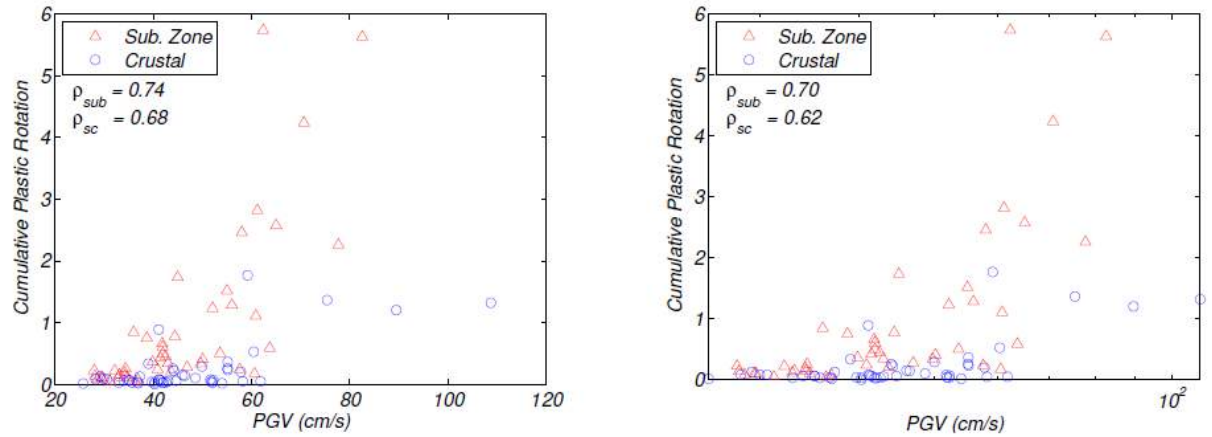

(a) Linear Scale (b) Log Scale

Figure 4.31. Peak ground velocity of subduction zone and shallow crustal earthquake motions plotted against cumulative plastic rotation for the longitudinal model with non-liquefiable site conditions.

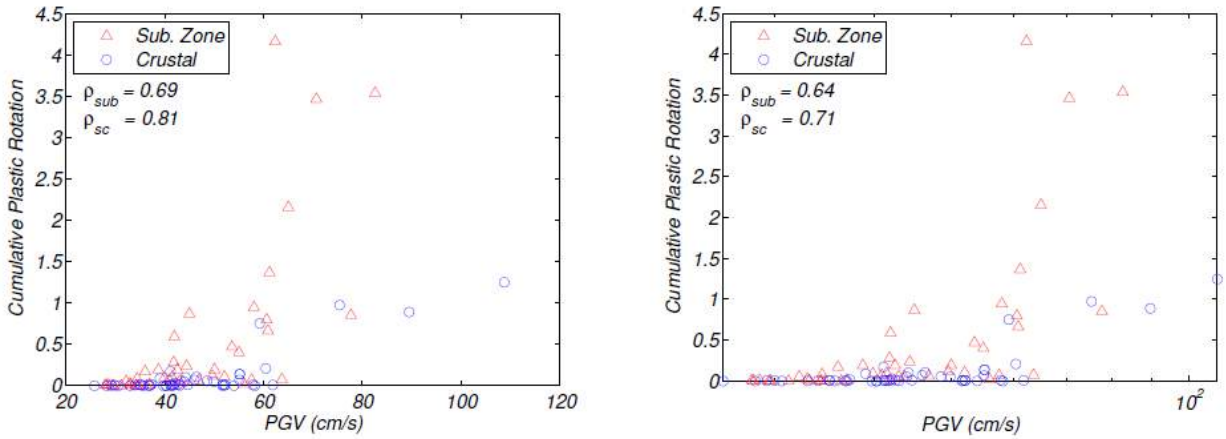

(a) Linear Scale (b) Log Scale

Figure 4.32. Peak ground velocity of subduction zone and shallow crustal earthquake motions plotted against cumulative plastic rotation for the longitudinal model with liquefiable site conditions.

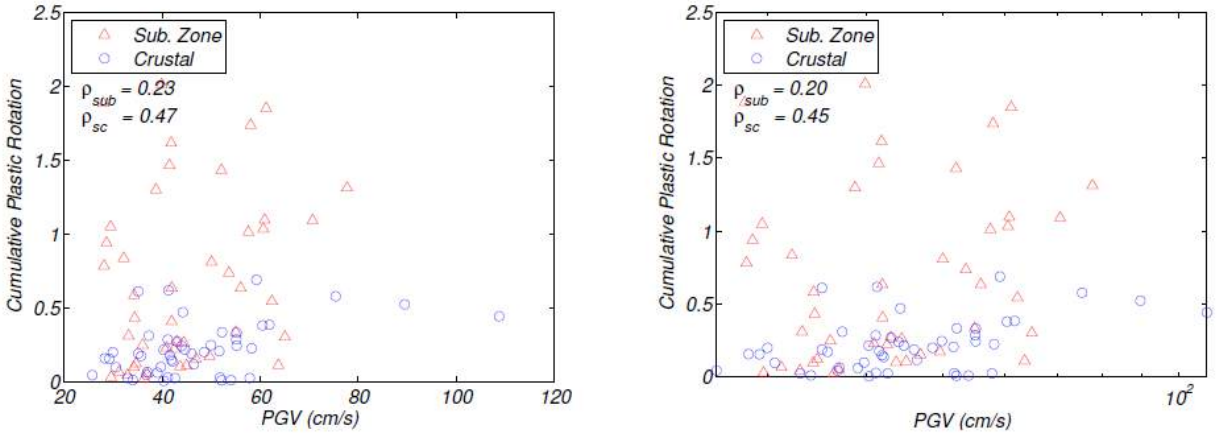

Figure 4.33. Peak ground velocity of subduction zone and shallow crustal earthquake motions plotted against cumulative plastic rotation for the transverse model with non-liquefiable site conditions.

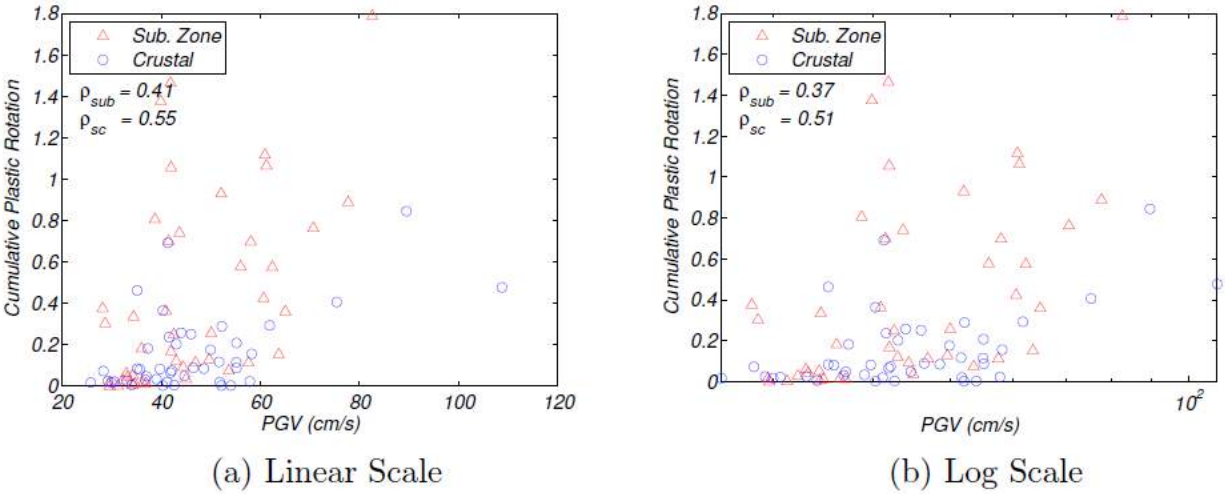

Figure 4.34. Peak ground velocity of subduction zone and shallow crustal earthquake motions plotted against cumulative plastic rotation for the transverse model with liquefiable site conditions.

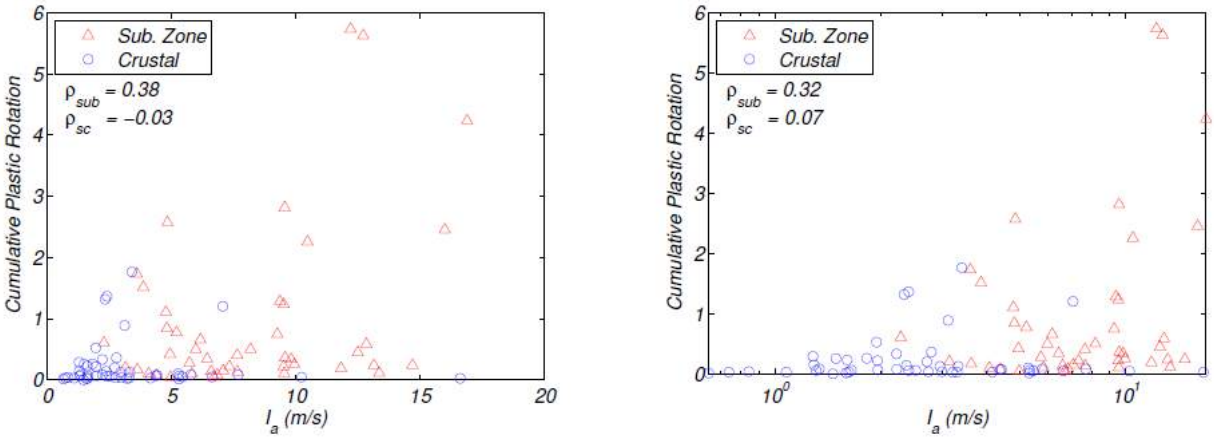

(a) Linear Scale (b) Log Scale

Figure 4.35. Arias intensity of subduction zone and shallow crustal earthquake motions plotted against cumulative plastic rotation for the longitudinal model with non-liquefiable site conditions.

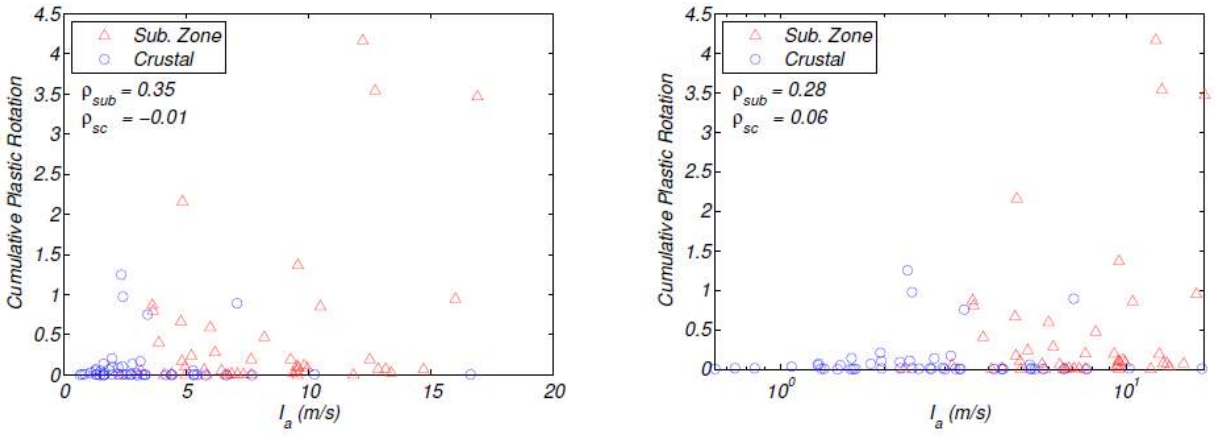

(a) Linear Scale (b) Log Scale

Figure 4.36. Arias intensity of subduction zone and shallow crustal earthquake motions plotted against cumulative plastic rotation for the longitudinal model with liquefiable site conditions.

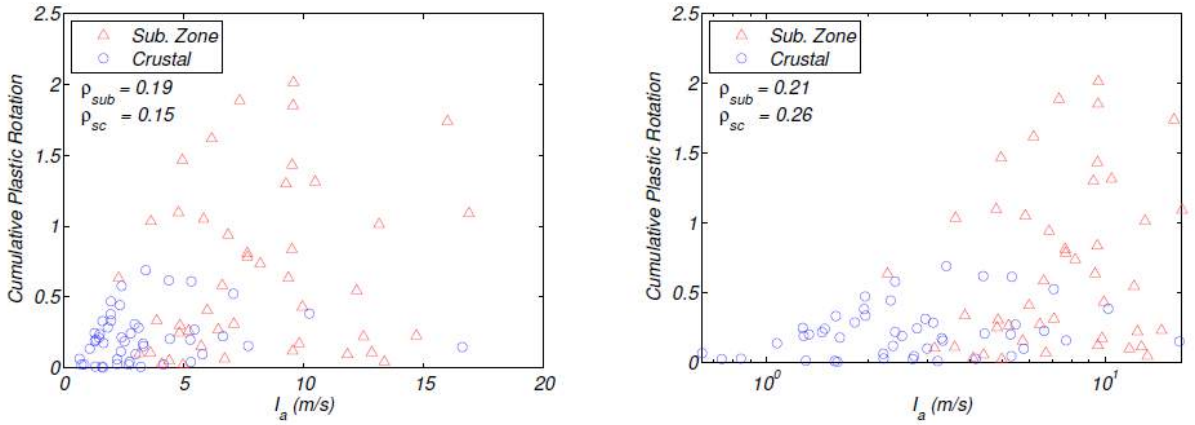

(a) Linear Scale (b) Log Scale

Figure 4.37. Arias intensity of subduction zone and shallow crustal earthquake motions plotted against cumulative plastic rotation for the transverse model with non-liquefiable site conditions.

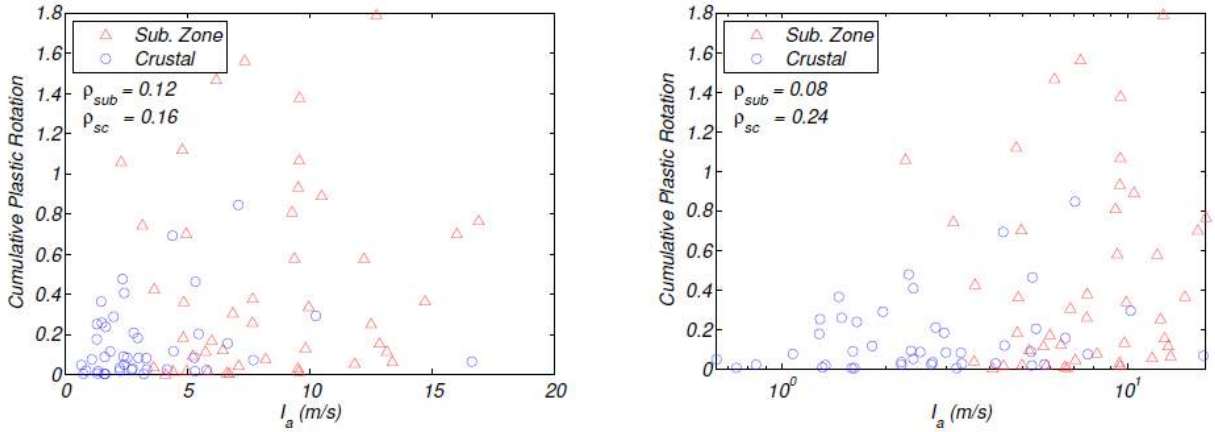

(a) Linear Scale (b) Log Scale

Figure 4.38. Arias intensity of subduction zone and shallow crustal earthquake motions plotted against cumulative plastic rotation for the transverse model with liquefiable site conditions.

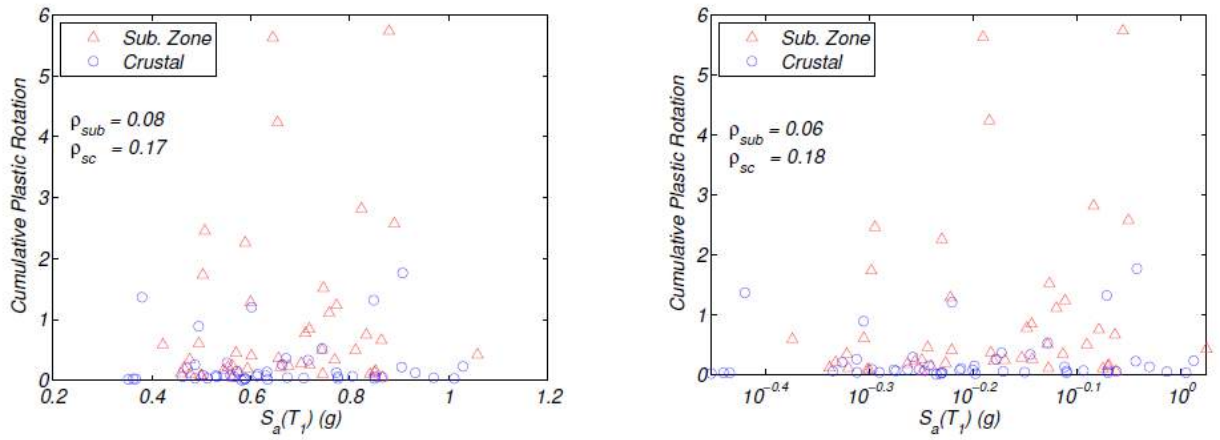

Figure 4.39. Spectral Acceleration at T_1 of subduction zone and shallow crustal earthquake motions plotted against cumulative plastic rotation for the longitudinal model with non-liquefiable site conditions.

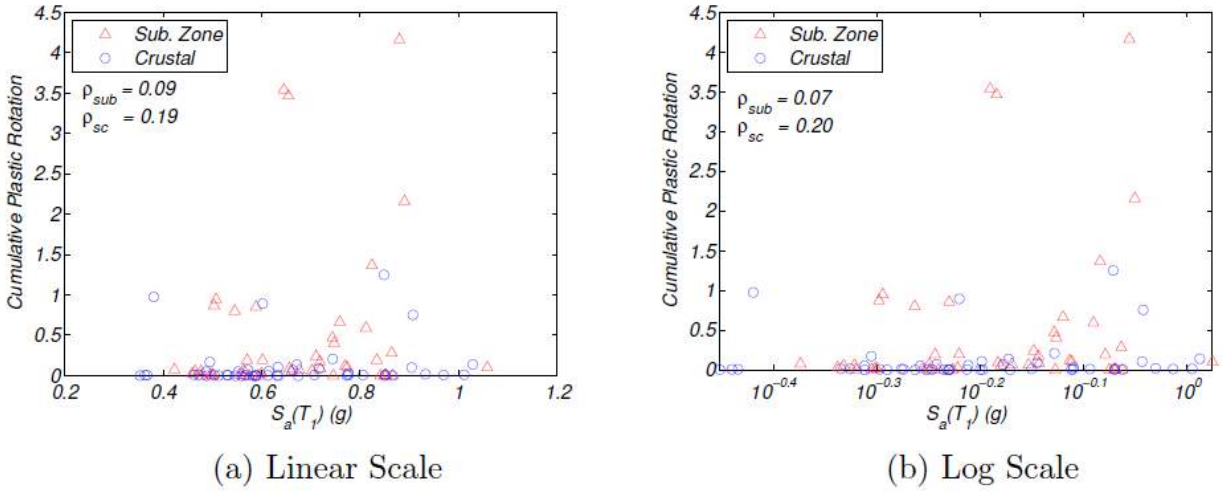

Figure 4.40. Spectral Acceleration at T_1 of subduction zone and shallow crustal earthquake motions plotted against cumulative plastic rotation for the longitudinal model with liquefiable site conditions.

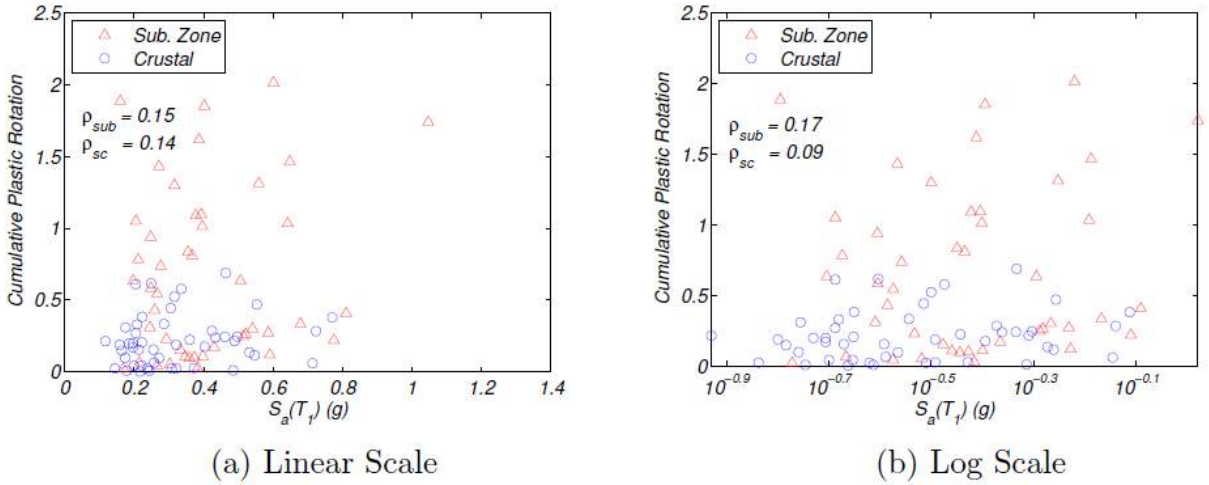

Figure 4.41. Spectral Acceleration at T_1 of subduction zone and shallow crustal earthquake motions plotted against cumulative plastic rotation for the transverse model with non-liquefiable site conditions.

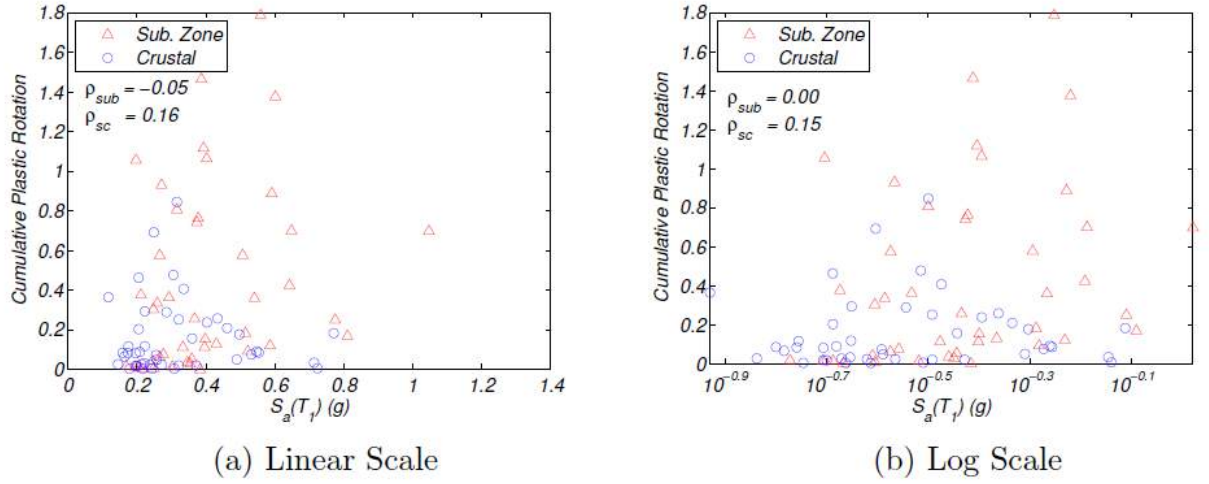

Figure 4.42. Spectral Acceleration at T_1 of subduction zone and shallow crustal earthquake motions plotted against cumulative plastic rotation for the transverse model with liquefiable site conditions.

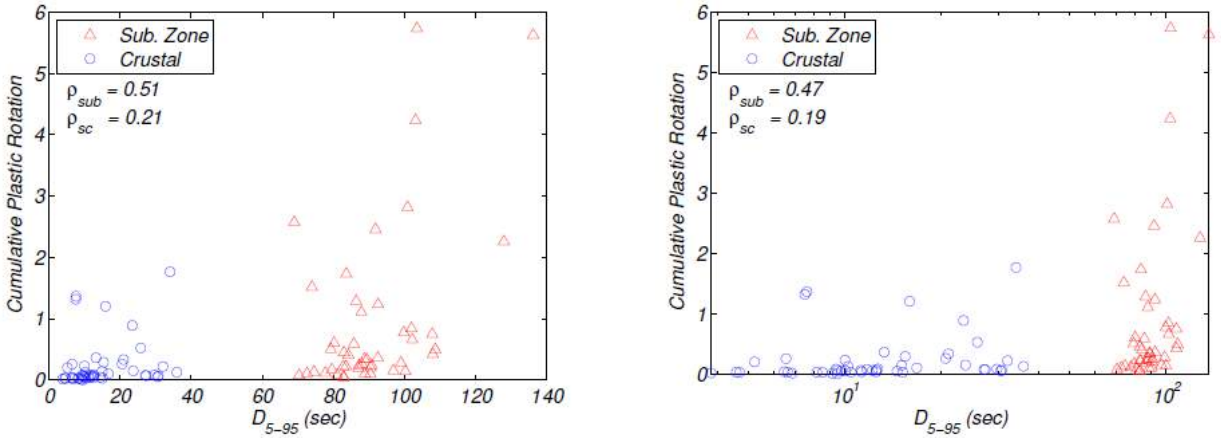

(a) Linear Scale (b) Log Scale

Figure 4.43. Significant duration of subduction zone and shallow crustal earthquake motions plotted against cumulative plastic rotation for the longitudinal model with non-liquefiable site conditions.

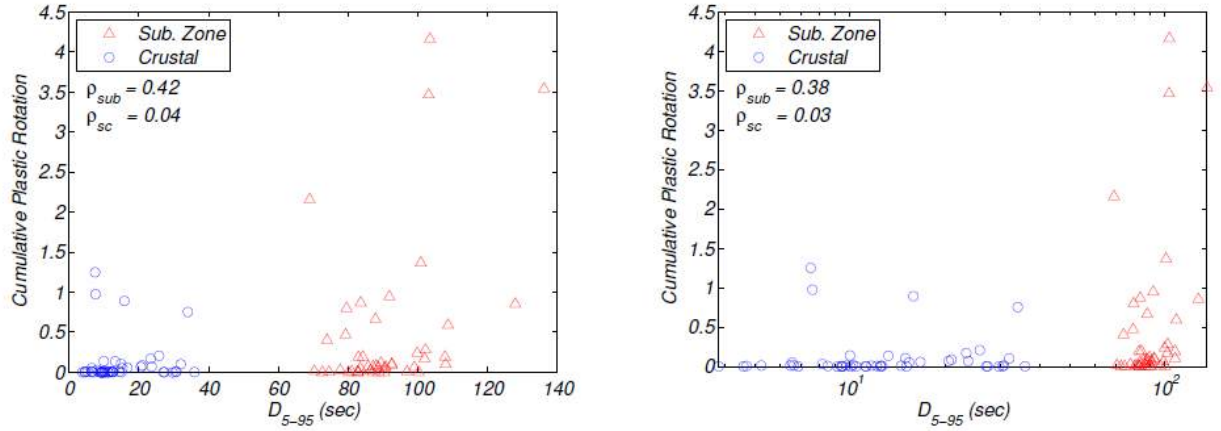

(a) Linear Scale (b) Log Scale

Figure 4.44. Significant duration of subduction zone and shallow crustal earthquake motions plotted against cumulative plastic rotation for the longitudinal model with liquefiable site conditions.

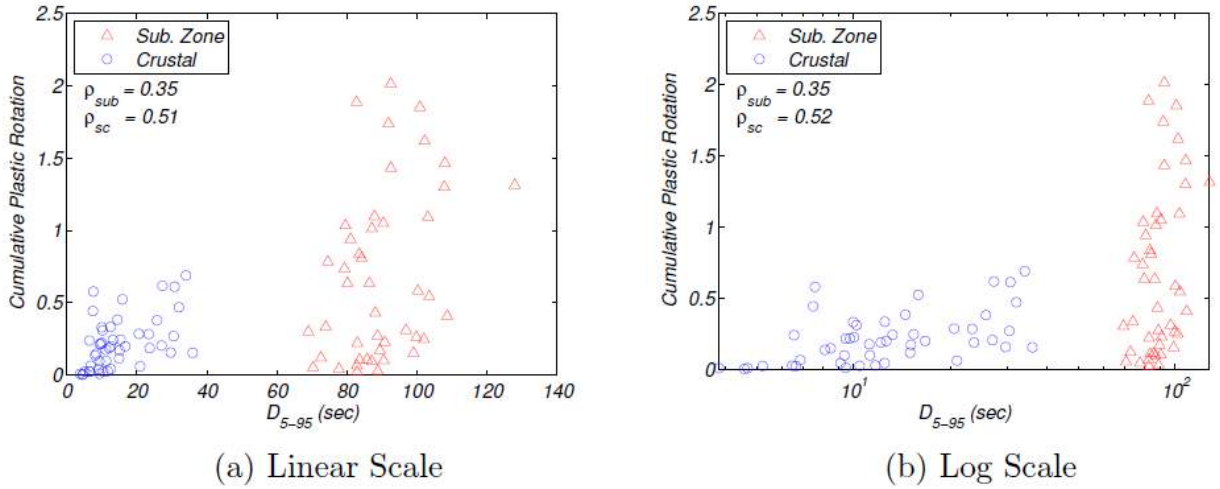

(a) Linear Scale (b) Log Scale

Figure 4.45. Significant duration of subduction zone and shallow crustal earthquake motions plotted against cumulative plastic rotation for the transverse model with non-liquefiable site conditions.

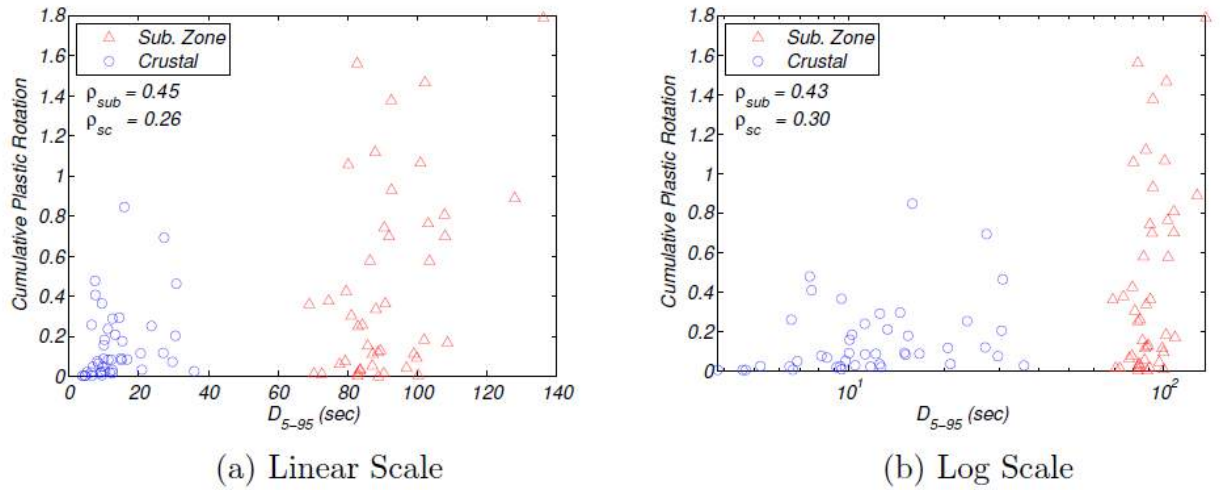

(a) Linear Scale (b) Log Scale

Figure 4.46. Significant duration of subduction zone and shallow crustal earthquake motions plotted against cumulative plastic rotation for the transverse model with liquefiable site conditions.

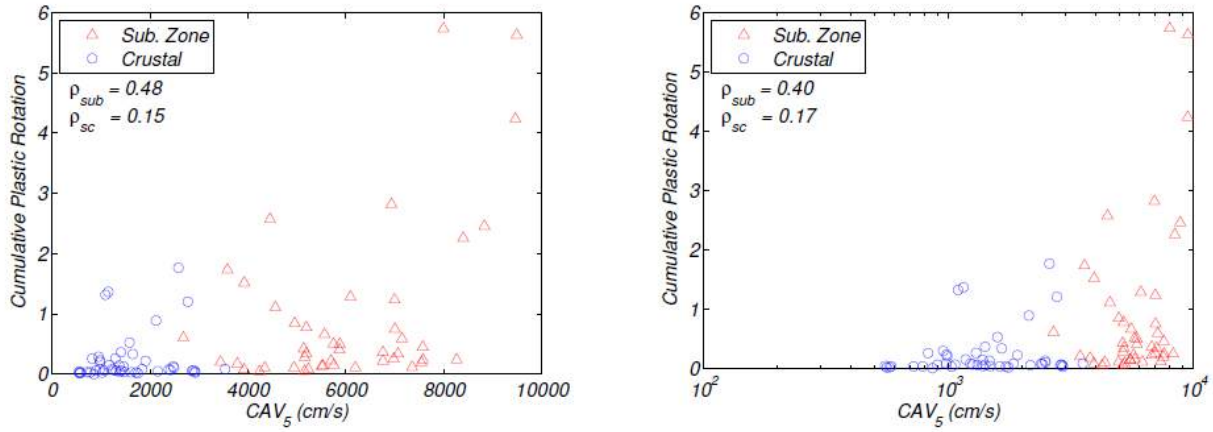

(a) Linear Scale (b) Log Scale

Figure 4.47. Cumulative absolute velocity five of subduction zone and shallow crustal earthquake motions plotted against cumulative plastic rotation for the longitudinal model with non-liquefiable site conditions.

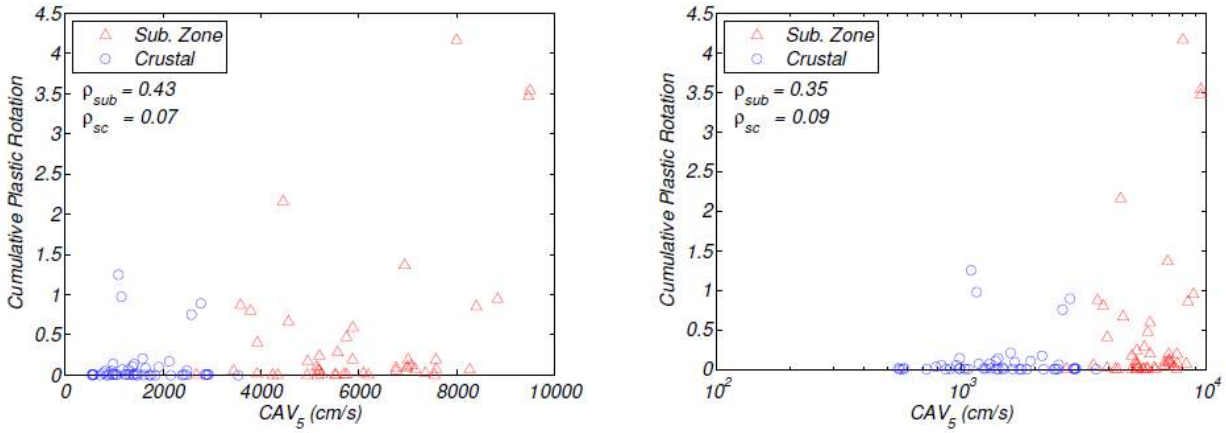

(a) Linear Scale (b) Log Scale

Figure 4.48. Cumulative absolute velocity five of subduction zone and shallow crustal earthquake motions plotted against cumulative plastic rotation for the longitudinal model with liquefiable site conditions.

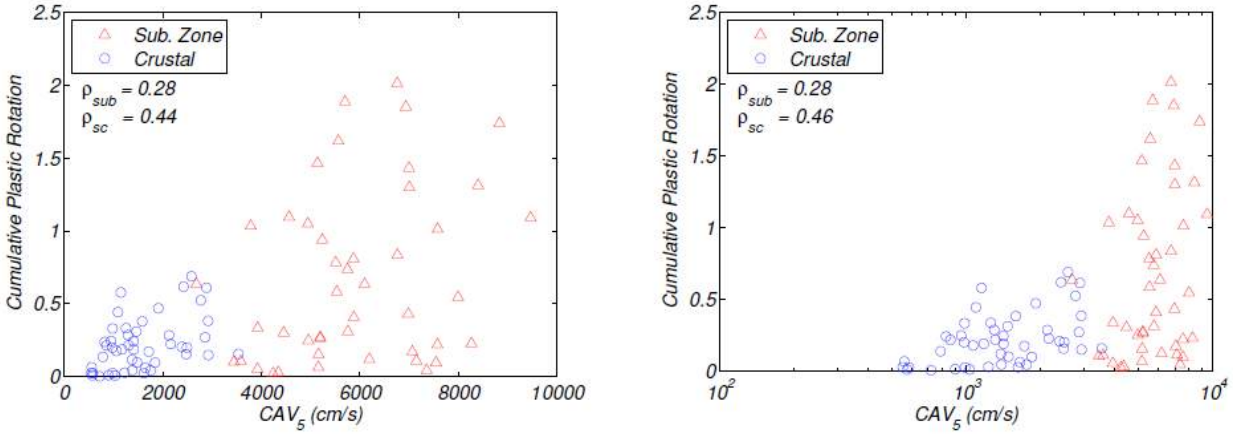

(a) Linear Scale (b) Log Scale

Figure 4.49. Cumulative absolute velocity five of subduction zone and shallow crustal earthquake motions plotted against cumulative plastic rotation for the transverse model with non-liquefiable site conditions.

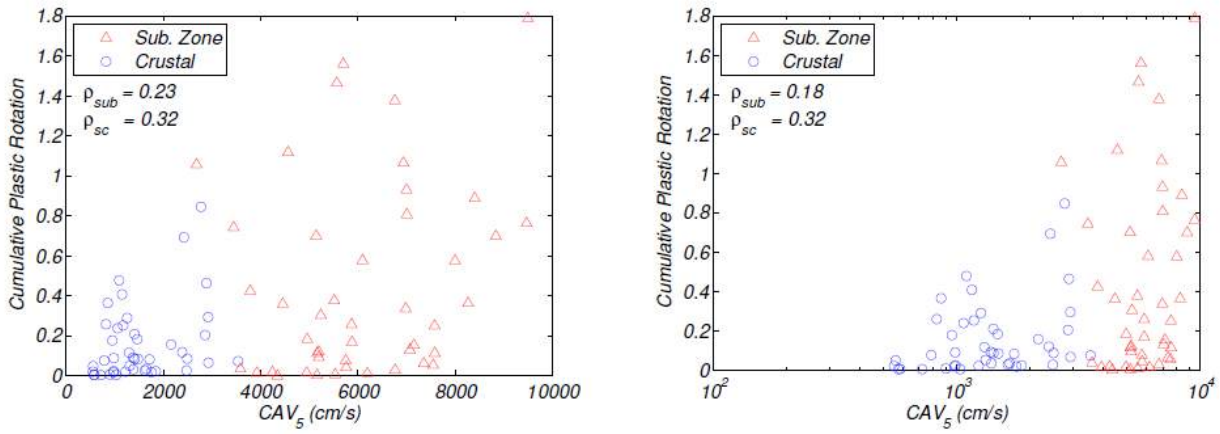

(a) Linear Scale (b) Log Scale

Figure 4.50. Cumulative absolute velocity five of subduction zone and shallow crustal earthquake motions plotted against cumulative plastic rotation for the transverse model with liquefiable site conditions.

Table 4.1. Correlation coefficients for the longitudinal model with subduction zone earthquake motions (θ = relative deck drift; NL = non-liquefiable soil; Liq = liquefiable soil; *NIE* = number of inelastic excursions; *CPR* = cumulative plastic rotation)

	NIE		CPR		Peak θ		ln| Peak θ|		Residual θ	
	NL	Liq	NL	Liq	NL	Liq	NL	Liq	NL	Liq
PGA	-0.07	-0.06	0.08	0.09	-0.05	-0.04	-0.05	-0.04	0.14	0.05
ln| PGA|	-0.08	-0.05	0.07	0.07	-0.06	-0.06	-0.06	-0.06	0.17	0.09
PGV	0.57	0.71	0.74	0.69	0.80	0.82	0.80	0.82	0.08	0.01
ln|PGV|	0.58	0.72	0.70	0.64	0.78	0.80	0.78	0.80	0.11	0.04
I_a	0.32	0.22	0.38	0.35	0.36	0.37	0.36	0.37	0.16	0.08
ln|I_a|	0.34	0.20	0.32	0.28	0.31	0.32	0.31	0.32	0.19	0.15
$S_a(T_1)$	0.18	0.23	0.08	0.09	0.20	0.22	0.19	0.21	0.29	0.20
ln|$S_a(T_1)$|	0.20	0.24	0.06	0.07	0.21	0.22	0.19	0.21	0.26	0.17
$D_{5–95}$	0.65	0.45	0.51	0.42	0.49	0.46	0.49	0.46	-0.11	-0.11
ln| $D_{5–95}$|	0.65	0.43	0.47	0.38	0.45	0.42	0.45	0.42	-0.08	-0.09
CAV_5	0.48	0.35	0.48	0.43	0.47	0.47	0.47	0.47	0.12	0.06
ln|CAV_5|	0.48	0.31	0.40	0.35	0.40	0.41	0.40	0.41	0.16	0.12

Table 4.2. Correlation coefficients for the longitudinal model with shallow crustal earthquake motions (θ = relative deck drift; NL = non-liquefiable soil; Liq = liquefiable soil; *NIE* = number of inelastic excursions; *CPR* = cumulative plastic rotation)

	NIE		CPR		Peak θ		ln| Peak θ|		Residual θ	
	NL	Liq	NL	Liq	NL	Liq	NL	Liq	NL	Liq
PGA	-0.24	-0.35	-0.18	-0.08	-0.12	-0.10	-0.23	-0.17	-0.01	-0.02
ln| PGA|	-0.28	-0.40	-0.18	-0.06	-0.09	-0.08	-0.22	-0.18	-0.03	-0.04
PGV	-0.23	0.35	0.68	0.81	0.84	0.86	0.79	0.81	-0.53	-0.57
ln|PGV|	-0.22	0.37	0.62	0.71	0.75	0.77	0.75	0.79	-0.43	-0.46
I_a	0.07	-0.12	-0.03	-0.01	-0.08	-0.05	-0.14	-0.07	0.04	0.05
ln|I_a|	0.24	-0.06	0.07	0.06	-0.01	0.00	-0.07	-0.04	0.04	0.04
$S_a(T_1)$	0.21	0.23	0.17	0.19	0.05	0.05	0.12	0.10	0.02	-0.03
ln|$S_a(T_1)$|	0.21	0.26	0.18	0.20	0.04	0.04	0.12	0.09	0.06	0.00
$D_{5–95}$	0.79	0.41	0.21	0.04	0.00	-0.01	0.14	0.13	0.27	0.27
ln| $D_{5–95}$|	0.75	0.42	0.19	0.03	0.02	0.01	0.17	0.15	0.29	0.29
CAV_5	0.52	0.15	0.15	0.07	-0.02	-0.01	0.00	0.03	0.17	0.17
ln|CAV_5|	0.56	0.20	0.17	0.09	0.02	0.02	0.05	0.06	0.15	0.15

Table 4.3. Correlation coefficients for the transverse model with subduction zone earthquake motions (θ = relative deck drift; NL = non-liquefiable soil; Liq = liquefiable soil; *NIE* = number of inelastic excursions; *CPR* = cumulative plastic rotation)

	NIE		CPR		Peak θ		ln| Peak θ|		Residual θ	
	NL	Liq	NL	Liq	NL	Liq	NL	Liq	NL	Liq
PGA	0.08	0.19	0.06	0.00	-0.02	-0.06	-0.02	-0.06	0.19	0.20
ln| PGA|	0.09	0.18	0.08	-0.01	-0.04	-0.08	-0.04	-0.08	0.18	0.19
PGV	0.47	0.52	0.23	0.41	0.80	0.84	0.80	0.84	0.16	0.13
ln|PGV|	0.48	0.51	0.20	0.37	0.78	0.80	0.78	0.80	0.18	0.16
Ia	0.18	0.46	0.19	0.12	0.35	0.42	0.35	0.42	0.25	0.25
ln|Ia|	0.19	0.42	0.21	0.08	0.31	0.38	0.31	0.38	0.20	0.21
Sa(T1)	0.17	-0.02	0.15	-0.05	0.38	0.43	0.44	0.51	0.23	0.18
ln|Sa(T1)|	0.16	0.02	0.17	0.00	0.43	0.49	0.50	0.59	0.26	0.20
D5−95	0.20	0.36	0.35	0.45	0.40	0.59	0.40	0.59	-0.13	-0.12
ln| D5−95|	0.19	0.35	0.35	0.43	0.37	0.55	0.37	0.55	-0.12	-0.12
CAV5	0.25	0.51	0.28	0.23	0.44	0.55	0.44	0.55	0.18	0.17
ln|CAV5|	0.25	0.47	0.28	0.18	0.40	0.50	0.40	0.50	0.16	0.16

Table 4.4. Correlation coefficients for the transverse model with shallow crustal earthquake motions (θ = relative deck drift; NL = non-liquefiable soil; Liq = liquefiable soil; *NIE* = number of inelastic excursions; *CPR* = cumulative plastic rotation)

	NIE		CPR		Peak θ		ln| Peak θ|		Residual θ	
	NL	Liq	NL	Liq	NL	Liq	NL	Liq	NL	Liq
PGA	-0.13	0.00	0.00	0.19	0.10	0.12	0.07	0.14	-0.12	-0.06
ln| PGA|	-0.13	0.05	0.01	0.26	0.14	0.17	0.09	0.18	-0.15	-0.10
PGV	0.27	0.57	0.47	0.55	0.76	0.77	0.76	0.76	-0.46	-0.74
ln|PGV|	0.17	0.45	0.45	0.51	0.66	0.66	0.72	0.71	-0.39	-0.59
I_a	0.25	0.17	0.15	0.16	0.16	0.16	0.17	0.19	-0.19	-0.03
ln|I_a|	0.37	0.27	0.26	0.24	0.21	0.21	0.23	0.25	-0.21	-0.07
$S_a(T_1)$	0.28	0.50	0.14	0.16	0.04	-0.02	0.16	-0.01	0.01	0.01
ln|$S_a(T_1)$|	0.32	0.48	0.09	0.15	0.09	0.04	0.19	0.05	-0.02	-0.04
D_{5-95}	0.59	0.34	0.51	0.26	0.05	0.02	0.24	0.16	-0.01	0.06
ln| D_{5-95}|	0.60	0.39	0.52	0.30	0.10	0.07	0.31	0.25	-0.05	0.05
CAV_5	0.58	0.38	0.44	0.32	0.22	0.20	0.29	0.27	-0.22	-0.04
ln|CAV_5|	0.58	0.39	0.46	0.32	0.22	0.20	0.33	0.31	-0.20	-0.04

Table 4.5. Number of inelastic excursions observed for shallow crustal earthquake motions

Motion	L-NL			L-Liq			T -NL			T-Liq		
	NIE	CPR	PθR	NIE	CPR	PθR	NIE	CPR	PθR	NIE	CPR	PθR
1	27	1.77	3.96	22	0.75	3.89	25	0.69	7.31	*	*	*
2	14	0.06	1.51	3	0.01	1.33	6	0.19	1.80	7	0.08	1.76
3	13	0.29	4.25	7	0.05	4.14	9	0.25	2.30	9	0.18	2.27
4	13	0.05	1.66	1	0	1.73	14	0.22	3.71	10	0.16	3.64
5	19	0.15	2.59	13	0.07	2.70	14	0.19	3.85	12	0.25	3.82
6	1	0	1.01	1	0	1.04	11	0.22	4.54	5	0.36	4.50
7	6	1.32	12.96	9	1.25	13.22	33	0.44	19.73	39	0.48	23.30
8	6	0.02	1.12	1	0	1.55	5	0.01	0.97	3	0	0.94
9	15	0.08	1.66	3	0.01	1.84	6	0.03	1.91	5	0.02	1.87
10	18	0.08	1.66	1	0	1.73	14	0.21	3.17	10	0.12	3.13
11	7	0.03	1.69	3	0.01	1.94	6	0.02	1.22	4	0	1.19
12	10	0.03	1.22	3	0.01	1.73	6	0.15	2.45	8	0.07	2.45
13	11	0.2	1.84	5	0.01	1.98	4	0.02	1.73	6	0.02	1.69
14	9	0.14	2.66	10	0.11	2.66	13	0.12	2.70	9	0.09	2.66
15	9	0.03	1.19	1	0	1.19	14	0.02	1.08	15	0.03	1.08
16	6	0.03	1.69	8	0.03	1.76	6	0.14	1.44	12	0.08	1.44
17	20	0.33	3.24	19	0.09	3.53	15	0.06	2.48	10	0.03	2.48
18	4	0.04	2.09	5	0.01	2.12	8	0.03	1.84	6	0.02	1.84
19	15	0.23	2.63	8	0.14	2.56	9	0.33	2.38	11	0.09	2.34
20	18	0.07	1.66	3	0	1.62	11	0.62	4.61	10	0.69	4.61
21	26	0.13	1.48	5	0	1.66	35	0.15	1.58	11	0.03	1.58
22	13	0.06	1.40	5	0.01	1.37	14	0.22	2.27	8	0.05	2.30
23	7	0.05	1.76	4	0.01	2.16	34	0.38	5.55	12	0.29	5.47
24	14	0.1	2.66	4	0.06	3.02	14	0.2	3.06	*	*	*
25	27	0.22	2.92	15	0.1	2.56	24	0.47	3.93	12	0.09	3.06
26	11	0.04	1.15	1	0	1.22	9	0.1	2.38	11	0.08	2.34
27	16	0.26	3.78	7	0.07	3.89	18	0.29	3.20	19	0.12	3.20
28	22	0.13	1.26	7	0.02	1.12	14	0.31	1.48	*	*	*
29	19	0.53	4.03	12	0.21	4.36	21	0.38	5.58	12	0.18	1.44
30	14	0.07	2.45	4	0.01	2.52	14	0.33	7.24	9	0.29	7.20
31	8	1.37	10.23	6	0.97	9.90	9	0.58	9.11	10	0.41	9.18
32	10	0.03	1.19	2	0	1.19	4	0	0.90	4	0	0.83
33	17	0.04	1.37	2	0	1.26	12	0.04	1.08	11	0.03	1.12
34	18	0.05	1.62	3	0	1.69	15	0.27	2.52	19	0.2	2.56
35	7	0.02	1.33	1	0	1.33	13	0.07	1.55	10	0.05	1.55
36	6	0.02	1.19	1	0	1.15	8	0.04	1.51	4	0.02	1.51
37	11	0.03	1.84	2	0.01	1.80	3	0.01	1.37	2	0	1.37
38	10	0.36	4.18	13	0.14	4.32	10	0.24	4.14	18	0.21	4.14
39	15	0.08	1.51	1	0	1.30	22	0.1	1.58	9	0.02	1.55
40	13	0.06	1.62	3	0.01	1.51	7	0.01	1.22	*	*	*
41	30	0.89	3.67	22	0.17	3.42	28	0.28	1.80	5	0.01	1.19
42	8	0.26	3.28	10	0.05	3.24	10	0.24	2.45	10	0.26	2.45
43	14	0.08	1.37	2	0.01	1.62	11	0.2	1.73	10	0.02	1.73
44	17	0.06	2.05	8	0.01	2.12	19	0.61	3.67	22	0.46	3.64
45	29	0.08	1.04	1	0	1.22	25	0.16	1.40	17	0.07	1.37
46	12	0.06	1.33	4	0	1.55	13	0.18	3.64	12	0.24	3.64
47	7	0.03	1.40	2	0	1.15	23	0.17	3.35	13	0.08	3.35
48	10	1.2	8.28	18	0.89	8.21	28	0.52	35.36	30	0.85	37.77

L - longitudinal Model; T - Transverse Model
NL - Non-liquefiable Soil; Liq - Liquefiable Soil
NIE - Number of Inelastic Excursions; CPR - Cumulative Plastic Rotation
* Motion did not converge ; PθR - Peak Deck Drift Ratio

Table 4.6. Number of inelastic excursions observed for subduction zone earthquake motions

Motion #	L-NL			L-Liq			T -NL			T-Liq		
	NIE	CPR	PθR	NIE	CPR	PθR	NIE	CPR	PθR	NIE	CPR	PθR
1	28	0.08	2.23	12	0.02	2.23	22	0.05	1.66	6	0.01	1.66
2	113	0.5	2.88	103	0.47	2.66	56	0.74	2.12	22	0.08	2.05
3	66	1.52	4.25	77	0.4	4.25	61	0.34	3.28	*	*	4.65
4	56	2.58	6.09	48	2.16	6.12	123	0.3	4.57	91	0.36	1.33
5	46	0.15	2.09	3	0.01	2.12	68	0.31	1.33	48	0.04	2.66
6	66	0.28	2.41	15	0.06	2.56	47	0.15	2.70	59	0.11	0.86
7	39	0.61	1.22	1	0	1.12	52	0.64	0.86	28	1.06	0.94
8	24	0.05	1.04	1	0	1.30	23	0.07	0.97	3	0	1.94
9	57	0.17	2.95	36	0.8	2.92	114	1.03	1.91	102	0.42	2.27
10	82	0.45	2.27	39	0.19	2.52	67	0.22	2.30	71	0.25	1.01
11	21	0.05	1.40	1	0	1.22	13	0.02	1.01	12	0.02	1.87
12	121	0.59	2.66	12	0.08	2.88	73	0.11	1.94	75	0.15	2.45
13	103	0.66	3.20	54	0.28	3.46	83	1.62	2.41	72	1.46	1.19
14	37	0.1	1.19	1	0	1.30	18	0.03	1.19	*	*	*
15	79	1.23	3.06	33	0.11	3.20	83	1.43	2.16	97	0.93	2.20
16	78	0.34	2.63	40	0.12	3.13	43	0.17	2.23	24	0.13	2.20
17	78	1.11	2.23	73	0.67	2.56	68	1.1	2.56	73	1.12	2.63
18	54	0.22	2.63	10	0.05	2.74	61	0.84	2.09	11	0.03	2.05
19	50	0.41	2.77	48	0.19	3.35	217	0.81	2.34	63	0.26	2.30
20	53	0.19	1.48	3	0	1.40	53	0.1	1.33	38	0.05	1.37
21	57	0.22	1.91	5	0.01	1.80	49	1.89	2.41	57	1.56	2.41
22	73	0.26	2.23	36	0.08	2.12	84	0.43	1.69	103	0.34	1.66
23	37	0.14	1.62	4	0	1.76	99	0.78	1.30	115	0.38	1.30
24	46	0.11	1.12	1	0	1.33	*	*	*	9	0.01	0.94
25	147	2.26	4.86	110	0.85	4.65	83	0.12	0.97	133	0.89	4.65
26	99	5.63	7.92	79	3.54	7.17	97	1.31	4.54	109	1.79	6.09
27	98	0.84	2.77	46	0.17	2.56	77	0.25	1.91	43	0.18	1.91
28	106	0.78	3.06	53	0.24	3.20	66	0.26	2.41	32	0.09	2.38
29	47	0.14	1.12	2	0	1.15	65	0.58	0.97	12	0.01	0.97
30	56	0.24	2.92	15	0.07	2.74	69	0.23	2.09	106	0.36	2.05
31	80	0.36	2.16	21	0.09	2.34	63	2.01	2.45	137	1.38	2.41
32	87	2.46	4.93	93	0.95	4.39	98	1.74	3.38	164	0.7	3.35
33	37	0.08	1.30	7	0.01	1.40	37	0.94	1.30	62	0.3	1.26
34	36	0.12	1.94	7	0.03	2.23	43	0.04	1.30	54	0.06	1.22
35	45	0.11	1.12	1	0	1.33	56	1.05	1.01	11	0.01	1.01
36	61	0.24	3.10	41	0.07	3.31	82	1.01	3.13	42	0.11	3.10
37	95	4.24	5.11	67	3.46	5.83	100	1.09	5.04	114	0.76	5.01
38	83	5.74	7.63	77	4.16	7.06	110	0.55	4.25	118	0.58	4.29
39	48	0.2	2.59	10	0.05	2.63	52	0.1	2.27	73	0.74	2.20
40	78	0.34	2.81	27	0.06	2.70	74	0.27	2.09	45	0.12	2.05
41	106	0.5	3.06	83	0.59	3.24	110	0.41	2.38	74	0.17	2.38
42	86	0.42	3.02	23	0.1	2.92	70	1.47	2.52	98	0.7	2.45
43	115	0.75	2.88	51	0.19	2.63	89	1.3	2.45	73	0.81	2.41
44	97	2.82	3.78	103	1.37	3.93	141	1.85	3.71	58	1.06	3.78
45	43	1.73	3.10	58	0.87	3.31	93	0.11	1.73	20	0.04	1.84
46	49	1.29	3.02	13	0.02	2.81	59	0.64	2.52	118	0.58	2.45

L - longitudinal Model; T - Transverse Model
NL - Non-liquefiable Soil; Liq - Liquefiable Soil
NIE - Number of Inelastic Excursions; CPR - Cumulative Plastic Rotation
* Motion did not converge ; PθR - Peak Deck Drift Ratio

Table 4.7. Summary table of NIE and CPR for shallow crustal earthquake motions

	L-NL		L-Liq		T-NL		T-Liq	
	NIE	CPR	NIE	CPR	NIE	CPR	NIE	CPR
Mean	14	0.23	6	0.11	14	0.22	11	0.16
Median	13	0.08	4	0.01	13	0.20	10	0.08
Std. Dev.	7	0.39	6	0.27	8	0.18	7	0.19

Table 4.8. Summary table of NIE and CPR for subduction zone earthquake motions

	L-NL		L-Liq		T-NL		T-Liq	
	NIE	CPR	NIE	CPR	NIE	CPR	NIE	CPR
Mean	69	0.94	36	0.49	74	0.68	65	0.46
Median	64	0.39	30	0.09	68	0.55	63	0.28
Std. Dev.	29	1.34	32	0.95	35	0.58	41	0.48

Figure 4.3 through Figure 4.50 show that subduction zone earthquake motions cause significantly greater numbers of inelastic excursions (*NIE*) and cumulative plastic rotations (*CPR*) compared to shallow crustal earthquake motions. The increases in the *NIE* and *CPR* for the subduction zone earthquake motions occurred for both bridge orientations (i.e., longitudinal or transverse) and for both site-soil conditions (i.e., liquefiable or non-liquefiable). The larger *NIE* and *CPR* for the subduction zone earthquake motions suggest that an increase in earthquake motion duration does increase unrecoverable plastic deformations.

The correlation of the *NIE* and *CPR* with increasing earthquake motion intensity is much more robust for intensity measures that consider duration. Accordingly, *PGA*, *PGV*, $S_a(T_1,\beta)$, and I_a do not accurately predict the *NIE* and *CPR*. Figure 4.3 shows that an earthquake motion with a *PGA* of 0.4 g could produce approximately 10 to 100 inelastic excursions. CAV_5, which incorporate earthquake motion duration and amplitudinal intensity, predicts the *NIE* and *CPR* with increasing earthquake motion intensity much more robustly. For instance, a CAV_5 of 5000 cm/s (Figure 4.23) predicts the number of inelastic excursions to be between 25 and 75.

The average number of inelastic excursions for the transverse model is slightly higher than the longitudinal model for identical site-soil conditions. The recorded data for the transverse model also has greater dispersion compared to longitudinal model. These two trends are observed for both liquefiable and non-liquefiable site-soil conditions. The higher damage in the transverse model is possibly caused by the lack of fixity at the bridge deck, which is provided in the longitudinal model by the bridge abutments.

The liquefiable site-soil conditions produced lower *NIE* and *CPR* compared to the non-liquefiable conditions. The lower superstructure demands can be observed for the both transverse and longitudinal models. A potential reason for the lower superstructure demand for bridges atop liquefiable layers is that earthquake motion has been altered. When an earthquake motion propagates through a liquefiable layer, the fundamental properties of the earthquake motion (i.e. frequency content and intensity) are altered (Kramer 1996). For the soil-bridge model and site-soil conditions model herein, the changed earthquake motions decreases superstructure demands. It is important to note that with different models, and soil profiles, the liquefiable layer may increase superstructure demands.

The shallow crustal earthquake motion with the PGA of 1.3 g illustrated in Figure 4.3 through Figure 4.6 is the UC Santa Cruz (UCSC) earthquake motion recording (motion 11 in Appendix B) of the 1989 Loma Prieta earthquake. The scaled PGA of 1.3 g may seem unrealistic, but it illustrates the importance of earthquake motion duration. The UCSC earthquake motion has the highest PGA of the all the earthquake motions considered and typically would not be used for seismic design because of the exceptionally high PGA. Figure 4.3 and Figure 4.27 illustrates that amplitudinal intensity (e.g., *PGA*) of an earthquake motion is not the best indicator of durational damage. A shallow crustal earthquake motion with a *PGA* of

0.3 g in Figure 4.3 and Figure 4.27 has the potential to have twice the *NIE* and *CPR* compared with the UCSC earthquake motion. The lack compatibility between the *NIE* and *CPR* with increasing amplitudinal intensity is demonstrated with the UCSC earthquake motion.

Chapter 5 Conclusions

The primary objective of this research was to evaluate the safety and resilience of a typical Pacific Northwest (PNW) bridge to long duration ground shaking. The motivation for this research stems from the recent Great East Japan Earthquake, where damage to bridge structures was caused by the long-duration, strong ground shaking. To evaluate the seismic bridge system performance, a two-dimensional soil-bridge model was developed in the OpenSees finite element framework.

The soil-bridge model considered both the transverse and longitudinal directions with non-liquefiable and liquefiable site-soil conditions. For each of four soil-bridge model configurations, 46 subduction zone and 48 shallow crustal earthquake motions were analyzed. The earthquake motions were linearly scaled to a target spectrum to isolate earthquake motion duration effects, and to remove amplitudinal differences. Two soil-bridge system damage indicators – number of inelastic excursions (*NIE*) and cumulative plastic rotation (*CPR*) – were used, because typical damage measurements (e.g., peak deck drift ratio) not consider earthquake motion duration.

Subduction zone earthquake motions, which have longer durations compared to shallow crustal earthquake motions had much higher *NIE*s and *CPR*s compared to the shallow crustal earthquake motions. The increase in *NIE* and *CPR* for the subduction zone earthquake motions was apparent for each of the four model configurations considered. Furthermore, the earthquake motion intensity parameters that incorporate duration better predicted the *NIE* and *CPR* compared to the intensity measures that only incorporated amplitudinal intensity. The prediction of the *NIE* and *CPR* for durational dependent earthquake motion intensity parameters was validated with correlation coefficients. The liquefiable site-soil conditions were found to cause a

decrease in the *NIE* and *CPR* compared with the non-liquefiable site-soil conditions. The difference in damage was attributed to the liquefiable site-soil condition fundamentally changing the earthquake motion (i.e., intensity and frequency content) and leading to the lengthening of the fundamental period of the soil-bridge systems.

Many aspects of this work could be explored to garner a further understanding of the similarities and differences of shallow crustal and subduction zone earthquakes and the performance of soil-bridge systems. Potential future research is listed below:

- The development of additional soil-bridge systems to test different bridge types, materials, number of spans, foundation elements, or geometries.
- Perform additional sensitivity analyses to determine how the depth to and the depth of, the liquefiable soil layer influences analytical results.
- Include more earthquake motions for a more robust analysis of earthquake motion durations. Additional subduction zone earthquake motions should be selected or generated from events other than the 2011 Great East Japan earthquake.
- Develop a full three-dimensional nonlinear soil-bridge model for a complete coupling of longitudinal, transverse, and vertical earthquake motion components.

References

1. American Petroleum Institute (API). Recommended Practice for Planning, Designing and Constructing Fixed Offshore Platforms. American Petroleum Institute, Washington, DC, 1993.
2. J. W. Baker, T. Lin, S. K. Shahi, and N. Jayaram. New Ground Motion Selection Procedures and Selected Motions for the PEER Transportation Research Program. Technical Report PEER 2011/03, Pacific Earthquake Engineering Research Center, Berkeley, CA, 2011.
3. A. R. Barbosa and M. A. G. Silva. Bridge abutment interaction under seismic loading. In *2nd International Conference on Structural Condition Assessment, Monitoring and Improvement*, Changsha, China, pages 19–21, 2007.
4. A. R. Barbosa, H. B. Mason, and K. Romney. SSI-bridge: Soil-bridge interaction during long-duration earthquake motions. Technical Report PacTrans Report 2014, USDOT University Transportation Center for Federal Region 10, 2014.
5. D. M. Boore and J. J. Bommer. Processing of strong-motion accelerograms: needs, options and consequences. *Soil Dynamics and Earthquake Engineering*, 25(2):93– 115, 2005.
6. R. W. Boulanger, C. J. Curras, B. L. Kutter, D. W. Wilson, and A. Abghari. Seismic soil-pile-structure interaction experiments and analyses. *Journal of Geotechnical and Geoenvironmental Engineering*, 125(9):750–759, 1999.
7. T. J. Carey. Multi-Hazard Framework and Analysis of Soil-Bridge Systems: Long Duration Earthquake and Tsunami Loading. M.S. thesis, Oregon State University, 2014.
8. T.J. Carey, A.R. Barbosa, H.B. Mason, and M.H. Scott. Modeling framework for soil-bridge system response during sequential earthquake and tsunami loading. In *Tenth U.S. National Conference on Earthquake Engineering*, Anchorage, AK, 2014.
9. F. A. Charney. Unintended consequences of modeling damping in structures. *Journal of Structural Engineering*, 134(4):581–592, 2008.
10. M. M. Chiaramonte, P. Arduino, D. E. Lehman, and C. W. Roeder. Seismic analyses of conventional and improved marginal wharves. *Earthquake Engineering & Structural Dynamics*, 42:1435–1450, 2013.
11. A. Elgamal, Z. Yang, and E. Parra. Computational modeling of cyclic mobility and post-liquefaction site response. *Soil Dynamics and Earthquake Engineering*, 22(4): 259–271, 2002.
12. F. C. Filippou, E. P. Popov, and V. V. Bertero. Effects of bond deterioration on hysteretic behavior of reinforced concrete joints. Technical Report UCB/EERC-83/19, Earthquake Engineering Research Center, 1983.
13. J. F. Hall. Problems encountered from the use (or misuse) of Rayleigh damping. *Earthquake Engineering & Structural Dynamics*, 35(5):525–545, 2006.

14. I. D. Karsan and J. O. Jirsa. Behavior of concrete under compressive loadings. *Journal of the Structural Division*, 95(12):2543–2563, 1969.

15. M. M. Karthik and J. B. Mander. Stress-block parameters for unconfined and confined concrete based on a unified stress-strain model. *Journal of Structural Engineering*, 137(2):270–273, 2010.

16. E. Kausel. Early history of soil–structure interaction. *Soil Dynamics and Earthquake Engineering*, 30(9):822–832, 2010.

17. D. C. Kent and R. Park. Flexural members with confined concrete. *Journal of the Structural Division*, 97(7):1969–1990, 1971.

18. A. Khosravifar. Analysis and design for inelastic structural response of extended pile shaft foundations in laterally spreading ground during earthquakes. PhD thesis, University of California, Davis, 2012.

19. A. Kottke and E. M. Rathje. A semi-automated procedure for selecting and scaling recorded earthquake motions for dynamic analysis. *Earthquake Spectra*, 24(4):911– 932, 2008.

20. S. L. Kramer. *Geotechnical Earthquake Engineering*. Upper Saddle River, 1996.

21. J. B. Mander, M. J. N. Priestley, and R. Park. Theoretical stress-strain model for confined concrete. *Journal of Structural Engineering*, 114(8):1804–1826, August 1988.

22. C.R. McGann, P. Arduino, and P. Mackenzie-Helnwein. Simplified procedure to account for a weaker soil layer in lateral load analysis of single piles. *Journal of Geotechnical and Geoenvironmental Engineering*, 138(9):1129–1137, 2011.

23. F. McKenna, M. H. Scott, and G. L. Fenves. Nonlinear finite-element analysis software architecture using object composition. *Journal of Computing in Civil Engineering*, 24(1):95–107, 2010.

24. M. Menegotto and P. E. Pinto. Method of analysis for cyclically loaded R.C. plane frames including changes in geometry and non-elastic behaviour of elements under combined normal force and bending. In *Symposium on the Resistance and Ultimate Deformability of Structures Acted on by Well-Defined Repeated Loads*, pages 15– 22, Zurich, Switzerland, 1973.

25. R. L. Mosher. Load-transfer criteria for numerical analysis of axially loaded piles in sand. Part 1: Load-transfer criteria. Final Report Army Engineer Waterways Experiment Station, Vicksburg, MS, 1984.

26. G. Mylonakis and G. Gazetas. Seismic soil-structure interaction: Beneficial or detrimental? *Journal of Earthquake Engineering*, 4(3):277-301, 2000.

27. N. M. Newmark. A method of computation for structural dynamics. J*ournal of the Engineering Mechanics Division*, 85:67–94, 1959.

28. NIST. Soil-structure interaction for building structures. Technical Report No. NIST GCR 12-917-21, prepared by the NEHRP Consultants Joint Venture (a partnership of the Applied Technology Council and Consortium of Universities for Research in Earthquake

Engineering) for the National Institute of Standards and Technology, Washington D.C., 2012.

29. M. J. N Priestley. *Myths and Fallacies in Earthquake Engineering, Revisited*. IUSS press, 2003.
30. M. J. N. Priestley, G. M. Calvi, and M. J. Kowalsky. *Displacement Based Seismic Design of Structures*. IUSS Press, 2007.
31. L. C. Reese, W. R. Cox, and F. D. Koop. Analysis of laterally loaded piles in sand. In Fifth Annual Offshore Technology Conference, number OTC 2080, GESA Report No. D-75-9, Houston, TX, 1974.
32. F.L.A. Ribeiro, A.R. Barbosa, and L.C. Neves. Application of reliability-based robustness assessment of steel moment resisting frame structures under post-mainshock cascading events. *Journal of Structural Engineering*, 140, 2014.
33. H Bolton Seed. Design problems in soil liquefaction. *Journal of Geotechnical Engineering*, 113(8):827–845, 1987.
34. A. Shamsabadi, K.M. Rollins, and M. Kapuskar. Nonlinear soil–abutment–bridge structure interaction for seismic performance-based design. *Journal of Geotechnical and Geoenvironmental Engineering*, 133(6):707–720, 2007.
35. Z. Yang, A. Elgamal, and E. Parra. Computational model for cyclic mobility and associated shear deformation. *Journal of Geotechnical and Geoenvironmental Engineering*, 129(12):1119–1127, 2003.
36. M. H. M. Yassin. Nonlinear analysis of prestressed concrete structures under monotonic and cyclic loads. PhD thesis, University of California of Berkeley, 1994.
37. Y. Zhang, Z Yang, J. Bielak, J.P. Conte, and A. Elgamal. Treatment of seismic input and boundary conditions in nonlinear seismic analysis of a bridge ground system. In *16th ASCE Engineering Mechanics Conference*, pages 16–18. University of Washington, Seattle, USA, 2003.
38. Y. Zhang, J. P. Conte, Z. Yang, A. Elgamal, J. Bielak, and G. Acero. Two- dimensional nonlinear earthquake response analysis of a bridge-foundation-ground system. *Earthquake Spectra*, 24(2):343–386, 2008.

Appendix A Subduction Zone Earthquake Motions

Table A.1. Subduction zone earthquake motion state, location, and component (FN = fault normal; FP = fault parallel)

Number	Earthquake	Date	Station	Comp.	Lat.	Long.
1	Tohuku	3/11/2011	FKSH12	FN	37.2169	140.5703
2	Tohuku	3/11/2011	FKSH12	FP	37.2169	140.5703
3	Tohuku	3/11/2011	FKSH14	FN	37.0264	140.9702
4	Tohuku	3/11/2011	FKSH14	FP	37.0264	140.9702
5	Tohuku	3/11/2011	FKSH17	FN	37.6636	140.5974
6	Tohuku	3/11/2011	FKSH17	FP	37.6636	140.5974
7	Tohuku	3/11/2011	FKSH19	FN	37.4703	140.7227
8	Tohuku	3/11/2011	FKSH19	FP	37.4703	140.7227
9	Tohuku	3/11/2011	FKSH20	FN	37.4911	140.9871
10	Tohuku	3/11/2011	FKSH20	FP	37.4911	140.9871
11	Tohuku	3/11/2011	IWTH05	FN	38.8654	141.3512
12	Tohuku	3/11/2011	IWTH05	FP	38.8654	141.3512
13	Tohuku	3/11/2011	IWTH14	FN	39.7435	141.9087
14	Tohuku	3/11/2011	IWTH14	FP	39.7435	141.9087
15	Tohuku	3/11/2011	IWTH17	FN	39.6442	141.5977
16	Tohuku	3/11/2011	IWTH17	FP	39.6442	141.5977
17	Tohuku	3/11/2011	IWTH18	FN	39.463	141.6775
18	Tohuku	3/11/2011	IWTH18	FP	39.463	141.6775
19	Tohuku	3/11/2011	IWTH21	FN	39.4734	141.9336
20	Tohuku	3/11/2011	IWTH21	FP	39.4734	141.9336
21	Tohuku	3/11/2011	IWTH22	FN	39.334	141.3015
22	Tohuku	3/11/2011	IWTH22	FP	39.334	141.3015
23	Tohuku	3/11/2011	IWTH23	FN	39.2741	141.8233
24	Tohuku	3/11/2011	IWTH23	FP	39.2741	141.8233
25	Tohuku	3/11/2011	IWTH24	FN	39.1979	141.0118
26	Tohuku	3/11/2011	IWTH24	FP	39.1979	141.0118
27	Tohuku	3/11/2011	IWTH26	FN	38.969	141.001
28	Tohuku	3/11/2011	IWTH26	FP	38.969	141.001
29	Tohuku	3/11/2011	IWTH27	FN	39.0307	141.532
30	Tohuku	3/11/2011	IWTH27	FP	39.0307	141.532
31	Tohuku	3/11/2011	IWTH28	FN	39.0307	141.532
32	Tohuku	3/11/2011	IWTH28	FP	39.0307	141.532
33	Tohuku	3/11/2011	MYGH03	FN	38.9207	141.637
34	Tohuku	3/11/2011	MYGH03	FP	38.9207	141.637
35	Tohuku	3/11/2011	MYGH04	FN	38.786	141.325
36	Tohuku	3/11/2011	MYGH04	FP	38.786	141.325
37	Tohuku	3/11/2011	MYGH05	FN	38.5793	140.780
38	Tohuku	3/11/2011	MYGH05	FP	38.5793	140.7804
39	Tohuku	3/11/2011	MYGH06	FN	38.5907	141.071
40	Tohuku	3/11/2011	MYGH06	FP	38.5907	141.071
41	Tohuku	3/11/2011	MYGH09	FN	38.0091	140.6027
42	Tohuku	3/11/2011	MYGH09	FP	38.0091	140.6027
43	Tohuku	3/11/2011	MYGH10	FN	37.9411	140.8924
44	Tohuku	3/11/2011	MYGH10	FP	37.9411	140.8924
45	Tohuku	3/11/2011	MYGH12	FN	38.6416	141.4428
46	Tohuku	3/11/2011	MYGH12	FP	38.6416	141.4428

Table A.2. Intensity parameters for baseline corrected and filtered subduction zone earthquake motions before linear scaling (Order = order of Butterworth filter; f_1 = high-pass corner frequency; f_2 = low-pass corner frequency)

Number	PGA (g)	PGV (cm/s)	I_a (m/s)	$D_{5\text{-}95}$ (s)	CAV_5 (cm/s)	Order	f_1 (Hz)	f_2 (Hz)
1	0.10	10.8	0.37	70	968	4	0.16	25
2	0.10	10.3	0.30	79	912	4	0.165	25
3	0.12	21.2	0.57	74	1320	4	0.17	25
4	0.11	24.6	0.69	69	1490	4	0.175	25
5	0.08	7.1	0.32	97	1034	4	0.165	25
6	0.07	11.5	0.34	99	1089	4	0.16	25
7	0.35	20.9	0.57	80	1221	4	0.16	25
8	0.13	8.1	0.46	83	1182	4	0.16	25
9	0.36	41.0	1.66	80	2472	4	0.15	25
10	0.16	14.5	1.45	83	2404	4	0.16	25
11	0.16	12.7	0.60	83	1293	4	0.15	25
12	0.13	13.3	0.56	86	1270	4	0.165	25
13	0.04	4.6	0.07	102	341	4	0.16	25
14	0.05	4.4	0.09	89	394	4	0.18	25
15	0.05	6.8	0.16	93	638	4	0.165	25
16	0.05	6.3	0.16	89	631	4	0.17	25
17	0.07	12.7	0.21	88	711	4	0.16	25
18	0.05	4.8	0.21	83	761	4	0.17	25
19	0.07	9.2	0.26	84	836	4	0.16	25
20	0.07	5.2	0.27	87	892	4	0.17	25
21	0.07	5.1	0.24	83	797	4	0.16	25
22	0.06	4.5	0.17	88	668	4	0.165	25
23	0.14	7.9	0.61	75	1348	4	0.165	25
24	0.12	8.7	0.59	73	1331	4	0.175	25
25	0.11	20.5	0.73	128	1920	4	0.19	25
26	0.08	20.4	0.78	136	2084	4	0.16	25
27	0.11	13.3	0.66	102	1631	4	0.165	25
28	0.10	15.2	0.61	100	1549	4	0.16	25
29	0.10	12.2	0.47	101	1263	4	0.165	25
30	0.11	7.2	0.45	91	1211	4	0.15	25
31	0.07	6.0	0.22	93	768	4	0.16	25
32	0.07	6.7	0.21	92	759	4	0.16	25
33	0.13	9.7	0.78	81	1582	4	0.1625	25
34	0.16	8.2	0.83	78	1630	4	0.16	25
35	0.12	9.8	0.65	90	1471	4	0.1625	25
36	0.11	11.6	0.53	87	1317	4	0.163	25
37	0.18	18.5	1.15	103	2239	4	0.16	25
38	0.14	18.7	1.09	103	2151	4	0.16	25
39	0.17	26.1	1.12	90	1938	4	0.15	25
40	0.16	15.7	0.86	89	1690	4	0.15	25
41	0.12	16.9	0.97	109	2170	4	0.16	25
42	0.13	17.8	0.91	108	2028	4	0.16	25
43	0.15	15.4	1.46	108	2600	4	0.16	25
44	0.22	26.2	1.74	101	2772	4	0.15	25
45	0.24	23.0	0.94	84	1698	4	0.16	25
46	0.15	16.8	0.84	86	1644	4	0.16	25

Table A. 3. Intensity parameters for subduction zone earthquake motions after linear scaling (RMSE = root mean square error)

Number	PGA (g)	PGV (cm/s)	I_a (m/s)	D5-95 (s)	CAV5 (cm/s)	Scaling factor	RMSE
1	0.33	37.0	4.39	70	3924	3.4	1.4
2	0.50	53.6	8.18	79	5745	5.2	1.3
3	0.31	55.0	3.87	74	3926	2.6	2.3
4	0.29	65.1	4.84	69	4454	2.6	3.4
5	0.38	33.1	7.08	97	5754	4.7	1.4
6	0.30	46.9	5.73	99	5163	4.1	1.5
7	0.70	41.9	2.28	80	2682	2.0	1.2
8	0.49	31.2	6.70	83	5156	3.8	1.7
9	0.54	60.6	3.63	80	3785	1.5	2.6
10	0.46	42.6	12.49	83	7571	2.9	1.6
11	0.45	36.3	4.96	83	4237	2.9	1.9
12	0.62	63.7	12.83	86	7147	4.8	1.8
13	0.36	41.9	6.16	102	5563	9.2	1.0
14	0.32	29.6	4.08	89	4342	6.7	1.6
15	0.42	52.1	9.51	93	6993	7.7	1.2
16	0.42	49.7	9.81	89	7062	7.9	1.5
17	0.32	60.9	4.78	88	4563	4.8	1.7
18	0.36	32.2	9.50	83	6758	6.7	1.4
19	0.40	50.1	7.64	84	5868	5.4	0.8
20	0.48	34.2	11.82	87	7541	6.6	1.5
21	0.41	28.0	7.33	83	5695	5.5	1.4
22	0.47	34.4	9.94	88	6977	7.6	1.2
23	0.50	28.2	7.65	75	5510	3.5	1.4
24	0.49	34.7	9.54	73	6191	4.0	1.7
25	0.41	77.7	10.47	128	8398	3.8	2.1
26	0.34	82.6	12.71	136	9488	4.0	1.5
27	0.31	36.0	4.81	102	4954	2.7	2.6
28	0.30	44.4	5.20	100	5192	2.9	3.5
29	0.37	34.3	6.60	100	5531	3.8	1.1
30	0.63	40.9	14.69	91	8260	5.7	1.4
31	0.44	39.9	9.56	93	6754	6.7	1.3
32	0.58	58.1	15.99	92	8830	8.7	2.7
33	0.38	28.7	6.84	81	5234	3.0	2.5
34	0.65	32.9	13.36	78	7353	4.0	3.1
35	0.37	29.5	5.83	90	4944	3.0	0.9
36	0.54	57.6	13.13	87	7573	5.0	0.7
37	0.68	70.7	16.89	103	9461	3.8	1.1
38	0.46	62.4	12.20	103	7991	3.3	1.6
39	0.28	43.7	3.14	90	3444	1.7	3.5
40	0.43	43.0	6.43	89	5195	2.7	2.1
41	0.30	42.0	5.98	109	5875	2.5	2.7
42	0.30	41.5	4.94	108	5139	2.3	2.0
43	0.38	38.7	9.25	108	7000	2.5	0.8
44	0.52	61.2	9.55	101	6932	2.3	1.2
45	0.47	45.0	3.60	84	3585	2.0	1.8
46	0.51	56.0	9.36	86	6094	3.3	1.8

Appendix B Shallow Crustal Earthquake Motions

Table B.1. Shallow crustal earthquake motion station, location, and component

Number	Earthquake	Year	Station	Comp.	Lat.	Long.
1	Chi-Chi, Taiwan	1999	TCU138	FN	23.9223	120.5955
2	Taiwan SMART1(45)	1986	SMART1 E02	FN	24.6296	121.7610
3	Irpinia, Italy-01	1980	Bagnoli Irpinio	FN	40.8210	15.0690
4	Loma Prieta	1989	Santa Teresa Hills	FN	37.21	-121.803
5	Irpinia, Italy-01	1980	Bisaccia	FN	41.0130	15.3750
6	Chi-Chi, Taiwan	1999	TCU045	FN	24.5412	120.9137
7	Kocaeli, Turkey	1999	Gebze	FN	40.82	29.4400
8	Northridge-01	1994	Pacoima Dam	FN	34.334	-118.396
9	Loma Prieta	1989	Gilroy Array #6	FN	37.026	-121.484
10	Chi-Chi, Taiwan	1999	WNT	FN	23.8783	120.6843
11	Loma Prieta	1989	Golden Gate Bridge	FN	37.808	-122.476
12	Loma Prieta	1989	UCSC	FN	37.0010	-122.062
13	Duzce, Turkey	1999	Mudurnu	FN	40.463	31.1820
14	Kocaeli, Turkey	1999	Izmit	FN	40.79	29.9600
15	Northridge-01	1994	Howard Rd.	FN	34.2040	-188.302
16	Chi-Chi, Taiwan-03	1999	TCU138	FN	23.9223	120.5955
17	Chi-Chi, Taiwan-06	1999	TCU138	FN	23.9223	120.5955
18	Northridge-01	1994	LA Dam	FN	34.294	-118.483
19	Loma Prieta	1989	Envirotech	FN	37.512	-122.308
20	Chi-Chi, Taiwan	1999	TCU129	FN	23.8783	120.6843
21	Imperial Valley-06	1979	Cerro Prieto	FN	32.421	-115.301
22	Hector Mine	1999	Hector	FN	34.8294	-116.335
23	Duzce, Turkey	1999	Lamont 531	FN	40.7030	30.8550
24	Hector Mine	1999	Heart Bar State Park	FN	34.1610	-116.799
25	Chi-Chi, Taiwan	1999	TCU138	FN	23.9223	120.5955
26	Taiwan SMART1(45)	1986	SMART1 E02	FP	24.6296	121.7610
27	Irpinia, Italy-01	1980	Bagnoli Irpinio	FP	40.8210	15.0690
28	Loma Prieta	1989	Santa Teresa Hills	FP	37.21	-121.803
29	Irpinia, Italy-01	1980	Bisaccia	FP	41.0130	15.3750
30	Chi-Chi, Taiwan	1999	TCU045	FP	24.5412	120.9137
31	Kocaeli, Turkey	1999	Gebze	FP	40.82	29.4400
32	Northridge-01	1994	Pacoima Dam	FP	34.334	-118.396
33	Loma Prieta	1989	Gilroy Array #6	FP	37.026	-121.484
34	Chi-Chi, Taiwan	1999	WNT	FP	23.8783	120.6843
35	Loma Prieta	1989	Golden Gate Bridge	FP	37.808	-122.476
36	Loma Prieta	1989	UCSC	FP	37.0010	-122.062
37	Duzce, Turkey	1999	Mudurnu	FP	40.463	31.1820
38	Kocaeli, Turkey	1999	Izmit	FP	40.79	29.9600
39	Northridge-01	1994	Howard Rd.	FP	34.2040	-188.302
40	Chi-Chi, Taiwan-03	1999	TCU138	FP	23.9223	120.5955
41	Chi-Chi, Taiwan-06	1999	TCU138	FP	23.9223	120.5955
42	Northridge-01	1994	LA Dam	FP	34.294	-118.483
43	Loma Prieta	1989	Envirotech	FP	37.512	-122.308
44	Chi-Chi, Taiwan	1999	TCU129	FP	23.8783	120.6843
45	Imperial Valley-06	1979	Cerro Prieto	FP	32.421	-115.301
46	Hector Mine	1999	Hector	FP	34.8294	-116.335
47	Duzce, Turkey	1999	Lamont 531	FP	40.7030	30.8550
48	Hector Mine	1999	Heart Bar State Park	FP	34.1610	-116.799

Table B.2. Intensity parameters for shallow crustal motions prior to linear scaling

Number	PGA (g)	PGV (cm/s)	I_a (m/s)	$D_{5–95}$ (s)	CAV_5 (cm/s)
1	0.20	40.7	1.61	34	1724
2	0.12	12.6	0.32	12	482
3	0.19	29.3	0.44	15	543
4	0.27	25.9	1.29	10	920
5	0.12	17.8	0.19	24	433
6	0.60	44.1	1.75	9	949
7	0.24	51.9	0.53	7	501
8	0.50	48.8	1.31	4	519
9	0.16	17.5	0.40	12	492
10	0.96	69.2	7.90	27	3203
11	0.14	28.6	0.33	7	375
12	0.37	12.1	1.37	9	828
13	0.11	10.2	0.19	16	365
14	0.15	22.6	0.56	15	660
15	0.11	8.1	0.25	10	375
16	0.13	19.7	0.24	8	349
17	0.06	9.0	0.12	21	320
18	0.58	77.1	1.87	6	837
19	0.14	20.0	0.21	10	318
20	1.01	60.2	9.29	27	3554
21	0.15	18.3	1.31	36	1539
22	0.34	37.1	1.65	10	1076
23	0.16	12.6	0.43	15	580
24	0.07	7.2	0.11	17	302
25	0.23	40.8	1.67	32	1751
26	0.15	14.2	0.38	11	504
27	0.13	23.4	0.33	21	529
28	0.22	22.1	1.02	10	839
29	0.06	15.8	0.13	26	387
30	0.29	33.7	0.82	13	782
31	0.14	28.2	0.34	8	409
32	0.25	18.7	0.36	5	324
33	0.18	11.5	0.27	13	395
34	0.63	41.2	4.98	31	2733
35	0.18	29.9	0.42	7	444
36	0.31	11.6	1.07	9	779
37	0.07	15.8	0.10	16	270
38	0.22	29.8	0.81	13	752
39	0.14	6.8	0.29	9	390
40	0.13	12.9	0.19	9	317
41	0.05	7.4	0.10	23	317
42	0.42	40.8	1.28	7	762
43	0.10	7.6	0.09	13	209
44	0.64	35.8	5.51	31	2939
45	0.17	11.5	1.25	30	1399
46	0.31	33.0	1.04	11	832
47	0.12	13.0	0.43	15	608
48	0.09	13.5	0.16	16	356

Table B.3. Intensity parameters for shallow crustal earthquake motions after linear scaling

Number	PGA (g)	PGV (cm/s)	I_a (m/s)	$D_{5–95}$ (s)	CAV_5 (cm/s)	Scaling Factor	RMSE
1	0.29	59.2	3.41	34	2581	1.5	1.7
2	0.35	35.1	2.52	12	1413	2.8	1
3	0.32	50	1.28	15	952	1.7	3.2
4	0.62	58.3	6.63	10	2159	2.3	2
5	0.32	46	1.29	24	1174	2.6	1.6
6	0.55	40.3	1.46	10	860	0.9	3.3
7	0.5	108.7	2.33	8	1093	2.1	2.1
8	0.55	54	1.6	4	575	1.1	3.6
9	0.38	41.2	2.22	12	1228	2.4	1.1
10	0.72	51.7	4.41	27	2386	0.7	1.4
11	0.21	42.6	0.74	7	585	1.5	4.7
12	1.3	41.9	16.61	9	2926	3.5	3.2
13	0.55	57.9	2.71	5	986	1.9	3.4
14	0.31	46.4	2.37	15	1378	2.1	1.7
15	0.45	33	4.16	11	1619	4.1	3.1
16	0.28	42.1	1.08	8	786	2.1	2
17	0.28	39	2.22	21	1649	4.3	1.5
18	0.39	51.8	0.84	7	551	0.7	2.6
19	0.39	55.2	1.61	10	984	2.8	1.9
20	0.7	41.3	4.38	27	2422	0.7	1.3
21	0.24	29.3	3.33	36	2476	1.6	2.1
22	0.41	44.7	2.41	10	1310	1.2	2.7
23	0.78	61.9	10.23	15	2922	4.9	4.5
24	0.47	48.6	5.27	17	2493	6.8	2.3
25	0.24	44.2	1.96	32	1910	1.1	3.1
26	0.42	39.7	2.99	11	1479	2.8	2.4
27	0.31	55.1	1.83	21	1295	2.4	2.5
28	0.38	37.3	2.95	10	1469	1.7	1.8
29	0.24	60.5	1.95	26	1585	3.8	3
30	0.44	52.2	1.96	13	1256	1.5	1.9
31	0.38	75.4	2.41	8	1152	2.7	1.8
32	0.52	40.3	1.62	5	719	2.1	1.4
33	0.58	36.8	2.74	13	1386	3.2	1.6
34	0.66	43.1	5.45	31	2858	1	2.6
35	0.23	37	0.65	7	560	1.2	1.9
36	0.69	25.8	5.29	9	1756	2.2	1.4
37	0.81	52.1	3.21	5	1029	2	3.5
38	0.41	55.2	2.79	13	1411	1.9	1.7
39	0.63	30.6	5.77	9	1843	4.4	2
40	0.34	34	1.31	10	901	2.6	1.1
41	0.3	41.1	3.11	23	2126	5.6	1.2
42	0.45	44	1.49	7	826	1.1	1.5
43	0.4	30	1.34	13	977	3.9	1.1
44	0.63	35.1	5.31	31	2885	1	2.6
45	0.43	28.3	7.68	30	3536	2.5	2.9
46	0.38	41.6	1.65	11	1063	1.3	2.9
47	0.34	35.7	3.3	15	1718	2.8	2.1
48	0.62	89.5	7.07	16	2771	6.6	1.8